

Design of a High-Speed Crank-Slider Valve for use in
Hydraulic Switch-Mode Systems with Experimental
Validation in a Pressure Boost Converter Circuit

A Thesis
SUBMITTED TO THE FACULTY OF
UNIVERSITY OF MINNESOTA
BY

Shaun E. Koltavy

IN PARTIAL FULFILLMENT OF THE REQUIREMENTS
FOR THE DEGREE OF
Master of Science in Mechanical Engineering

Advisor: James Van de Ven

June 2016

Acknowledgements

I would like to thank the people who made this work and my tremendous educational experience possible. Thank you to my advisor, James Van de Ven for accepting me into his incredible research group and providing an endless amount of knowledge and guidance throughout the entire experience. Regardless the roadblock he was always easily approachable and able to provide guidance in an understandable manner. I would also like to thank my lab colleague Alexander Yudell for allowing me to be a part of his in depth research and working with me to further develop ideas. Finally I would like to thank Steve Weber from Sun Hydraulics who provided invaluable knowledge regarding spool valve design and donated the critical spool and sleeve components which without this work would not have been possible.

Abstract

Fluid power offers the benefits of high power density, high force potential, and high-speed precision control. To achieve variable power demand, systems often implement metering control, which results in heat dissipation and low overall efficiency. Improved efficiency can be obtained with the use of a variable displacement pump, adding cost, complexity, and size compared to a fixed displacement pump. Switch-mode hydraulic circuits, analogous to switch-mode power electronics, provide alternative control topologies that rely on switching between efficient on and off states. A challenge in realizing these circuits is the need for a high-speed valve with a demanding set of requirements. These requirements include fast transition time, high frequency switching, high flow rates, low energy losses, and a variable duty cycle. The work presented includes the design and modeling of valve that meets these requirements, experimental testing of the valve prototype, and experimental demonstration of the prototype in a pressure boost converter. The valve architecture consists of a dual spool design actuated from a common crank-shaft by two 4-bar crank-slider mechanisms. The valve completes two switching cycles per crank-shaft revolution and the variable duty cycle is achieved by phase shifting one crank arm relative to the other. The valve design constraints included a switching frequency up to 120 Hz, a transition ratio of 5% of the cycle period, and a flow rate of 22.8 lpm at a 0.6 MPa pressure drop. The experimental validation of the valve consisted of two quasi-static tests and one transient test. The first test determined the valve effective area as a function of crank-shaft position. The experimental results agreed well with the model resulting in a 3% variation in transition time and a 13.3% variation in valve overlap. The second test measured the valve leakage which matched the model in shape and order of magnitude. The third test measured the input torque. At low speeds, due to binding forces in the revolute joints the model showed poor agreement, however at higher speeds, where inertial forces dominate, agreement improved significantly. The valve prototype was further validated with experimental demonstration in a pressure boost converter. The converter utilized a rigid tube as the inductive element and transient testing was completed at six different duty cycles, ranging from 0.2-0.9. The system demonstrated boost ratio capabilities of 1.08-2.06 with a general trend of higher boost ratios at lower duty cycles. The system efficiencies ranged from 19-62% with decreasing efficiencies at lower duty cycles. Overall, the valve performed well in the system and successfully demonstrated a boost ratio over two. This

high-speed valve enables switch-mode circuit studies that can improve efficiency in future work, allowing switch-mode circuits to be a viable control method for hydraulic systems.

Table of Contents

List of Tables	vi
List of Figures.....	vii
1. Introduction.....	1
1.1. Background	1
1.2. Literature Review	6
1.2.1. High-speed Valves	6
1.2.2. Switch Inertance Hydraulic Systems	12
1.3. Overview.....	14
2. Valve Design & Optimization	15
2.1. Introduction	15
2.2. Methods	15
2.2.1. Design Constraints	15
2.2.2. Architecture Design	16
2.2.3. Valve Model	22
2.2.4. Parameter Study of Design Trade-Offs and Detailed Design.....	28
2.2.5. Drive Mechanism.....	37
2.3. Optimized Valve Results	41
2.4. Conclusion	48
3. Valve Experimental Validation.....	50
3.1. Introduction	50
3.2. Methods	50
3.2.1. Valve Profile Quasi-static Test.....	50
3.2.2. Quasi-static Leakage & Torque Transient Test	58
3.3. Results	61
3.4. Discussion & Conclusion.....	71
4. Boost Circuit Experimental Validation	73

4.1.	Introduction	73
4.2.	Results	86
4.3.	Discussion and Conclusion	96
5.	Conclusion	98
5.1.	Review	98
5.2.	Conclusions	98
5.3.	Recommendations for Future Work	100
6.	References	102
Appendix A.	106
Appendix A.1.	Valve Part Drawings	106
Appendix A.2.	Potential Active Phase Shift Mechanism.....	127
Appendix A.3.	Pressure Sensor Calibrations	128

List of Tables

Table 2.1. Novel valve performance capabilities.....	17
Table 2.2. Flow types of secondary losses	33
Table 2.3. Drive mechanism component materials.....	40
Table 2.4. Valve design optimization results	41
Table 2.5. Drive mechanism component masses	44
Table 3.1. Quasi-static experimental equipment list.....	52
Table 3.2. Quasi-static C_dA Test Operating Points	55
Table 3.3. External pressure losses from experimental setup.....	57
Table 3.4. Leakage test pressure transmitters	59
Table 3.5. Electrical drive motor	61
Table 3.6. Experimental average flow rate and C_dA through fully open flow path A1.....	67
Table 4.1. Boost circuit experimental equipment list.....	76
Table 4.2. Experimental duty set points and resultant switching frequencies	80
Table 4.3. Boost circuit experimental set points.....	81
Table 4.4. Experimental actual duty cycle results	88
Table 4.5. Experimental boost ratio results	91
Table 4.6. Experimental power results.....	94

List of Figures

Figure 1.1. Simplified hydraulic pressure boost converter.....	3
Figure 1.2. Simplified hydraulic pressure buck converter	4
Figure 1.3. Noergaard et al, Electromagnetic coil moving actuator [14]	8
Figure 1.4. Tu H. et al, High-speed rotary valve design [17]	10
Figure 1.5. Pan et al, Pressure buck converter hydraulic system and electrical equivalent [21] ...	13
Figure 2.1. Crank-slider valve base architecture	18
Figure 2.2. Valve depicted at angular displacement of $\pi/2$	19
Figure 2.3. Example of how a phase shift affects duty cycle	20
Figure 2.4. Crank-slider vector loop convention	21
Figure 2.5. Port orifice area during valve transition	24
Figure 2.6. Effective area for a single flow path	25
Figure 2.7. Valve diagram showing major leakage paths	27
Figure 2.8. Relationship between number of ports in a row and the diameter of the ports vs. the required crank length to achieve a 5% transition ratio.....	29
Figure 2.9. The effect of crank length and radial clearance, on energy losses over a cycle.....	30
Figure 2.10. Energy loss over a cycle vs. the crank length and non-dimensionalized spool land length	31
Figure 2.11. Energy loss over a cycle vs. crank link length, with optimized land lengths of two times the crank link length and a radial clearance of 10 μm	32
Figure 2.12. Secondary throttling loss components of a single flow path.....	33
Figure 2.13. Flow path dimensions for secondary throttling loss.....	34
Figure 2.14. Resultant secondary pressure drop while varying circumferential flow gallery depth	36
Figure 2.15. Drive mechanism force balance	38
Figure 2.16. Drive mechanism	40
Figure 2.17. Effective area of the valve vs. crank link angular displacement when $\varphi = \pi/4$	42
Figure 2.18. Power losses as a fraction of flow power at rated pressure and volumetric flow rate.....	43
Figure 2.19. Solid model of spools and valve housing	44
Figure 2.20. Drive mechanism required input torque	45
Figure 2.21. Pin and bearing stresses in revolute joint.....	46

Figure 2.22. Contact stress in wrist pin.....	48
Figure 3.1. Valve validation hydraulic experimental setup.....	51
Figure 3.2. Experimental setup.....	52
Figure 3.3. Quasi-static electrical circuit diagram.....	54
Figure 3.4. Flow path identification for quasi-static experimental test.....	56
Figure 3.5. Experimental external fitting losses.....	57
Figure 3.6. Leakage hydraulic experimental setup.....	59
Figure 3.7. Torque transducer electrical circuit.....	60
Figure 3.8. Run nine C_dA profile.....	62
Figure 3.9. Valve block angular offset.....	63
Figure 3.10. Analytical effective area with a positive shift for spool one and a negative shift of spool two of 0.58 mm.....	64
Figure 3.11. Analytical and experimental transition time comparison.....	65
Figure 3.12. Valve analytical and experimental overlap comparison between flow paths A2 and B3.....	66
Figure 3.13. Experimental C_dA values for nine flow rate trials.....	67
Figure 3.14. Comparison of analytical and experimental C_dA at various flow rates.....	68
Figure 3.15. Experimental and analytical leakage comparison.....	69
Figure 3.16. Analytical and experimental input torque comparison at 30.1 rad/s.....	70
Figure 3.17. Analytical and experimental input torque comparison at 180.6 rad/s.....	70
Figure 4.1. Simplified pressure boost converter.....	73
Figure 4.2. Experimental boost circuit hydraulic schematic.....	75
Figure 4.3. Experimental boost circuit setup (1).....	75
Figure 4.4. Experimental boost circuit setup (2).....	76
Figure 4.5. Boost circuit electrical circuit schematic.....	79
Figure 4.6. Duty cycle adjustment method.....	83
Figure 4.7. Experimental valve profile, $D=0.9$	87
Figure 4.8. Experimental valve profile peak locations, $D=0.9$	88
Figure 4.9. System experimental pressures, $D=0.5$	89
Figure 4.10. Inertance tube experimental pressures, $D=0.5$	90
Figure 4.11. Boost ratio as a function of duty.....	92

Figure 4.12. System power as a function of duty	93
Figure 4.13. System efficiency as a function of duty.....	94
Figure 4.14. Inertance tube pressure transients at $D=0.5$	95
Figure 6.1. Dynamic phase shift concept utilizing differential gear set.....	127
Figure 6.2. Pressure boost converter, source pressure transmitter calibration.....	128
Figure 6.3. Pressure boost converter, mid-tube pressure transducer calibration	129
Figure 6.4. Pressure boost converter, valve entry pressure transducer calibration	129
Figure 6.5. Pressure boost converter, load pressure transmitter calibration	130
Figure 6.6. Pressure boost converter, tank pressure transmitter calibration	130

1. Introduction

This chapter introduces the reader to switch-mode hydraulic circuits and specifically the requirements of a high-speed valve for these circuits. The first section consists of the background, including motivations and contributions. The second section consists of a literature review outlining additional high-speed valve technologies as well as sample switch-mode circuits. The final section provides an overview of the remaining chapters.

1.1. Background

Hydraulics, the transmission of power via a liquid such as oil, provides many benefits. The power density of hydraulics is an order of magnitude greater than electromechanical system [1]. It can provide high force with rapid response time due to the high bulk modulus of the transmitting fluid. A major drawback, however, is the low overall efficiency.

According to an Oak Ridge National Laboratory report, fluid power systems in the US consume between 2.0 and 2.9 Quads of energy annually, with mobile hydraulics consuming of 0.4 to 1.3 Quads and industrial hydraulics consuming of 1.1 Quads. “In terms of efficiency, the study indicates that, across all segments, fluid power system efficiencies range from less than 9% to as high as 60% (depending upon the application), with an average efficiency of 22%” [1]. This provides a massive opportunity for energy savings with even modest efficiency gains.

One example of a low efficiency mobile hydraulic system is an excavator, which can consist of many actuators, from motors to drive the tracks to cylinders that control the bucket and stick, each which have varying independent demands. These actuators are typically driven from a common pump. The supply pressure must accommodate the pressure requirement of the highest demanding actuator, which results in pressure throttling via control valves to the lower pressure actuators. A field of fluid power research that is pursuing a more efficient alternative to metering valve control is switch-mode hydraulics which is a subdivision of digital hydraulics [2].

Switch-mode hydraulics, analogous to DC-DC converters from power electronics, replaces dissipative throttling valve control with efficient on and off states [3]. In electronics, the state of

the circuit is switched with a transistor, while in hydraulics a high-speed on/off valve switches the state. For useful operation, as defined by low flow ripple and fast response, the valve must have a high switching frequency and ideally instantaneous transition from closed to open states. In power electronics, transistors can easily obtain switching frequencies >100 kHz. Achieving high switching frequencies with a hydraulic valve is challenging due to the high kinetic energy requirements of rapidly shifting a valve mass, along with additional requirements discussed later in this section.

Switch-mode hydraulics can be subdivided into switched inertance hydraulic systems (SIHS), and virtual variable displacement pumps. SIHS are capable of operating as hydraulic transformers offering an alternative to typical pump and motor transformer configurations [2]. SIHS topologies include pressure boost converters (step-up) and pressure buck converters (step-down) which are analogous to their power electronics counterparts [3]. Pressure converters switch between fluid acceleration and deceleration states, converting power from the kinetic to pressure domain or vice-versa [4]. Assuming an ideal system, conservation of energy dictates that a higher pressure (boost converter) results in a lower flow rate and a lower pressure (buck converter) results in a higher flow rate. A simplified pressure boost converter is presented in Figure 1.1 [5].

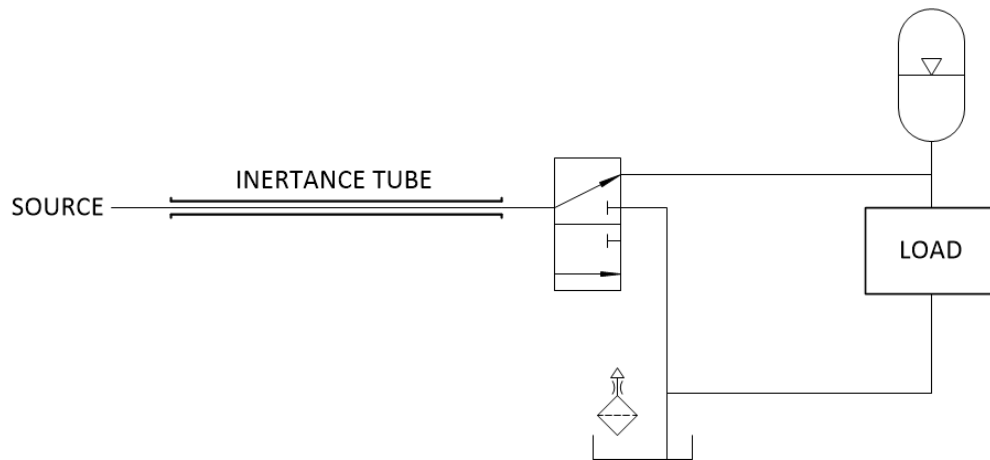


Figure 1.1. Simplified hydraulic pressure boost converter

The boost converter circuit functions as follows. When the valve is open to tank the fluid is accelerated through the tube. The valve rapidly switches to load, at which point the fluid is decelerated. The decrease in momentum results in an elevated load side pressure. Since the load flow is less than the total system flow, the circuit is capable of boosting the load side pressure above the source pressure. A pressure buck converter has the reverse effect as configured in Figure 1.2 [5].

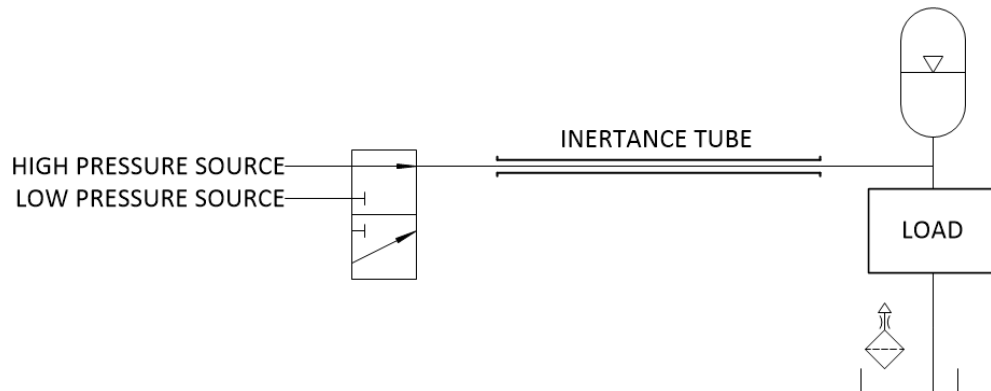


Figure 1.2. Simplified hydraulic pressure buck converter

The buck converter circuit functions as follows. When the valve connects the source to the load, the fluid is accelerated in the inertance tube. When the valve switches to the low pressure source the fluid momentum is directed away from the valve creating a suction effect which drives higher flow rates to load [4]. This topology results in a decreased load pressure and increased load flow rate compared to the high pressure source.

A third switch-mode circuit is a virtual variable displacement pump (VVDP). An axial piston pump provides variable displacement, but suffers from high cost, large size, and complex design relative to its gear pump equivalent [6]. Additionally low relative displacements result in low efficiencies [7]. An alternative to axial piston pumps is the use of a fixed displacement pump and a high-speed valve that efficiently switches between the load and tank providing a pulse width modulated pressure signal to load, typically termed virtual variable displacement pumps (VVDP) [7]. Comparable to a boost converter the pump behaves as the system inertance component in place of an inertance tube. High switching frequency is required to reduce flow ripple. The research presented in this thesis centers around SIHS but there are overlapping themes for VVDP throughout.

Building upon the excavator hydraulic system example provides evidence on how the SIHS may provide efficiency gains in common rail multi-actuator systems. A pressure boost converter

could be implemented at the higher pressure demanding actuators (such as high force cylinders) allowing the overall supply pressure to be lowered which, reduces the pressure throttling required. Furthermore, pressure reduction at point of use could be accomplished via a pressure buck converter.

The most challenging component in realizing the use of these topologies is a valve capable of meeting the demanding operational parameters required for efficient circuit operation. The optimal switching frequencies for these hydraulic inertance topologies is dependent on the inertance tube length L , the Duty D , and the sonic velocity c , described as [8]:

$$f = \frac{Dc}{2L} \quad 0 \leq D \leq 0.5; \quad f = \frac{(1-D)c}{2L} \quad D > 0.5 \quad (1.1)$$

With the use of hydraulic oil and an acceptable inertance tube length for experimental testing (<4 m) the maximum optimum switching frequency resulting from Eq. (1.1), is <120 Hz.

Additionally to prevent throttling losses, the transition time between open states needs to be minimized as well as the throttling losses in the fully open state. As the valve transitions between load and tank, the compressibility losses in the system need to be minimized by a reduction in the volume of fluid seeing changes in pressure, termed the switched volume. Additionally valve leakage and viscous friction need to be minimized. Furthermore, the valve must be capability of adjusting the duty cycle of the valve from 0-1.

There are three main contributions of this thesis work. The first is the modeling and design of a valve capable of meeting the demanding SIHS requirements. The design consists of a dual spool crank-slider valve that is designed for a 120 Hz maximum switching frequency at a fully open rated flow of 22.7 lpm. The fully open throttling loss is designed for <1% of the rated pressure of 34.5 MPa. The transition time is less than 5% (0.42 ms at 120 Hz) of the total cycle and the duty cycle is adjustable from 0-1. Leakage and viscous friction losses in the design result in less than 2% energy loss compared to full rated power. The second contribution is the experimental validation of the designed valve. The third contribution is the use of the high-speed valve prototype in a pressure boost converter. This work was completed in conjunction with PhD

candidate Alexander Yudell. The data acquired in the pressure boost converter will also contribute to the validation of his dynamic model of the switch-mode circuit.

This section provided motivation and a brief overview of the contributions of the thesis work. The subsequent section will provide a review of relevant research in hydraulic high-speed valves and in switch-mode circuits.

1.2. Literature Review

1.2.1. High-speed Valves

As the field of digital hydraulics has gained traction over recent years, much of the contribution has been towards the development of a suitable high-speed valve. The common valve architectures proposed include electromagnetic coil actuated valves, rotary valves, and multistage valves composed of a combination of driving mechanisms.

Solenoid Valves:

Solenoid valves provide the benefits of compactness, reliability, and the potential for high frequency operation. To develop the large actuation forces required for high switching element acceleration, the electromagnetic coils require either high current or a larger number of coil turns [9]. Increasing the number of turns results in an increased charge delay [10]. To decrease the forces necessary, solenoid valves typically design for a low mass switching elements with a short stroke. In addition the high peak currents require methods for heat dissipation [11]. The following is a discussion of example work completed in high-speed solenoid valves for digital hydraulics.

Muto, Yamada, and Suematsu proposed the use of two-way solenoid valves for pulse width modulation control of a hydraulic actuator [12]. The work was not focused on developing a high-speed solenoid valve but in working to model the operation of digital control to provide variable power to an actuator. For this reason a relatively slow spring return solenoid valve was utilized, with a transition time from signal to fully open of 7.4 ms. An important note from this work is that of the 7.4 ms transition time, 4.8 ms was delay from when the signal was generated to when

the switching element began shifting. This demonstrated the need for rapid coil saturation. They additionally noted the significant fluid line dynamics that occur and the challenges in modeling these and recommended reducing these effects. For their system the fluid transients provided undesirable results but this is contrary to switch inertance systems that rely on these transients for successful operation.

Kajima and Kawmura developed a spool driven solenoid valve capable of a 1 ms transition time for diesel engine control [13]. The architecture benefitted by the use of a double solenoid to provide bi-directional actuation. The model demonstrated optimized switching time tradeoffs between solenoid characteristics (plunger materials, sectional area of plunger, magnetic path length, applied voltage, etc.), stroke, and mass of moving parts. To improve on the delay seen in a non-optimized solenoid valve [12], a control was implemented that restricted the maximum current below the coil breakdown value and after transition dropped the current to prevent overheating the coil. Additionally, delay time reduction was proposed through parallel connection of coils. A key note is the significant increase in switching time from operation in air to operation in oil. This is caused not only by the viscous friction but additionally by accelerating the fluid, equivalent to adding mass to the spool. The fast transition time came at the expense high voltage (300 volts), high current (30 A), and small stroke (1 mm). A small stroke spool with clearance seals creates high leakage rates, which were not addressed.

More recently Noergaard, Roemer, Bech, and Andersen presented an alternative architecture that proved to be leakage free up to 40 MPa by replacing a clearance seal with a positive seal [14]. The design consisted of a moving coil and stationary permanent magnets. This design differed from the stationary coil proposed by Kajima and Kawmura [13]. The valve prototype was capable of a switching time of 1.5 ms at a large flow rate of 600 lpm. This flow rate was accomplished with a stroke of 3.5 mm at a pressure drop of <0.05 MPa, demonstrating that short stroke valves are capable of large flow rates. This design allowed the bobbin to free float in the air gap which was of concern since their work showed stress deformation in the bobbin with the potential to cause binding or wear. The results provided a correlation between fluid pressure and transition time, specifically increased pressure resulted in increased transition time, which is

undesirable. Their analytical optimization achieves 1 ms transition time at a high peak input power of 10 kW. The valve prototype design is presented in Figure 1.3.

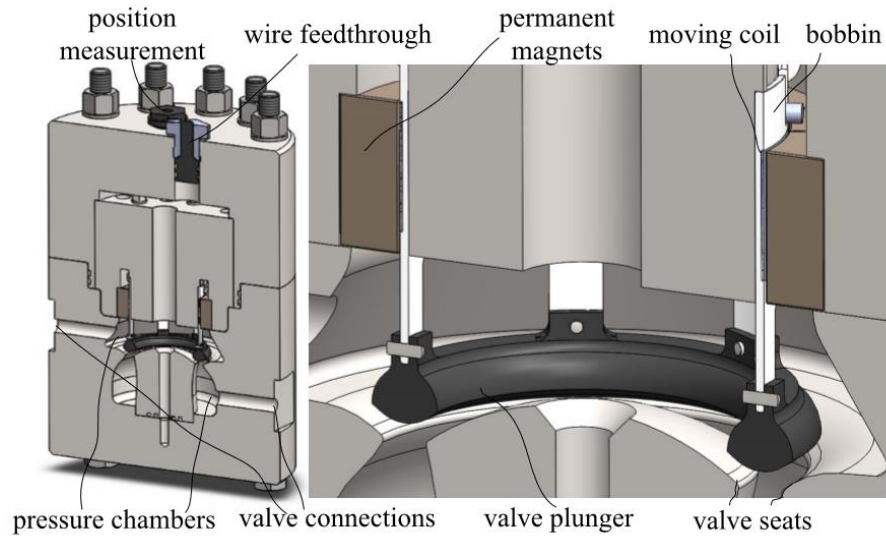


Figure 1.3. Noergaard et al, Electromagnetic coil moving actuator [14]

Overall, electromagnetic valves are capable of high switching frequencies, low transition times, and high flow rates when the valve is properly designed for a small stroke. As demonstrated, inherit operation at high speeds requires undesirable high peak voltages and currents. These large currents require large conductors, capable power supplies, and methods for heat dissipation.

Rotary Valves:

In contrast to linear solenoid valves, rotary valves have been proposed, which offer the benefit of continuous rotation requiring no inertial input force once the rotation element has reached its desired speed. Royston and Singh proposed a pneumatic rotary valve capable of pulse width modulation control of a linear actuator at a switching frequency of 80 Hz [15]. It consisted of a central rotational shaft, phase shifting outer rotor, and a ported fixed stator. As the center shaft continuously rotated, driven by a DC motor, flow paths between the supply-actuator and the return-actuator were open and closed and a secondary servo motor shifted an outer rotor which controlled the duty cycle. Phase shifting a stationary rotor provided significant benefits in control

over dynamic phase shifting. Numerical studies with the model, confirmed the large effect that small changes in valve dimensions have on the predicted results. This indicates the importance of high tolerance components and the challenges in manufacturing these high-speed switching valves. Internal and external leakage effects were noted but were not detailed. This system provided a near linear correlation between the actuator pressure and duty cycle. Further efficiency modeling is required to validate this design.

Van de Ven and Katz proposed an axial flow rotary valve for four quadrant operation of a fixed displacement pump/motor [16]. In this design, a disc rotated between a stator and an outlet plate. Phase shifting the outlet plate relative to the stator resulted in a three way valve that had two switching cycles per revolution similar to Royston and Singh [15]. The valve was rated for a switching frequency of 100 Hz and a flow rate of 10 lpm. This non-optimized design resulted in an efficiency of 73% at a duty ratio of one. Roughly 39% (120.6W) of the energy losses were a result of viscous friction resulting from the continuous high velocity inherent in rotary valves. A proposed solution was completing additional switching cycles per revolution. This would also increase the number of leakage paths. Further optimization may yield improved results, but as proposed, the efficiency is significantly less than the proposed crank-slider valve.

Tu et al. proposed a pulse width modulated rotary valve for use in virtual variable displacement pumps (VVDP) [17]. The valve consisted of a three way rotary spool with a central helical inlet entrance section. The duty cycle of the valve is adjusted by shifting the spool axially. The valve prototype achieved a flow of 40 lpm with a full open pressure drop of 0.62 MPa. At a switching frequency of 100 Hz the transition time was 2.8 ms. Two major benefits were incorporated into the design. One was the ability to achieve multiple switching cycles per revolution based on multiple circumferential sections, also proposed by Van de Ven and Katz [16]. The second was the self-actuating design which used turbine blades on the spool to scavenge energy from the fluid. The design resulted in an impressive 98.5% efficiency at a clearance of 20 μm but this was based on a fully open position, when leakage maximums typically occur during transition. The spool design is shown in Figure 1.4.

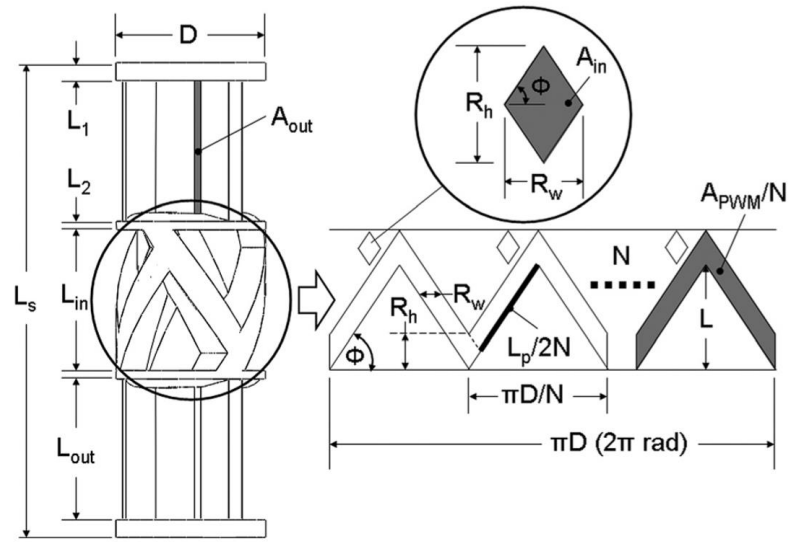


Figure 1.4. Tu H. et al, High-speed rotary valve design [17]

Rotary valves offer the benefit of no inertial acceleration once the switching element has reached operating speed. This comes at a cost of increased viscous friction losses due to the constant high velocity. Multiple switching cycles per revolution can partially mitigate this effect.

Two-Stage Valves:

Another architecture that has been proposed for high-speed valves is a multistage configuration where a high-speed low-flow pilot stage is used to control a high-flow stage. A commercially available example of this architecture is a servo valve. Yokota and Akutu proposed a two stage high-speed digital valve with the first stage consisting of a piezoelectric actuator [18]. The first stage piezoelectric poppet was capable of following a 2 kHz input signal at a displacement of approximately 15 μm . The researchers noted that this displacement is insufficient and needs to be increased. A benefit of a poppet design is the positive sealing, also used by Noergaard, et al [14]. Small switching displacements lead to high leakage if a clearance seal is used. Using the first stage poppet to control fluid actuation of a second stage spool, the design was capable of a full transition time of 2.8 ms with a 1.0 mm spool displacement. Implementation of a feed forward control was required to provide sufficient response and dampening which adds another level of complexity in non-rigid actuation mechanisms. While the first stage of this design achieves very

high speeds, the two stage valve does not meet the desired flow rates and transition time targets of the current work.

Lantela, Kajaste, Kostamo, and Pietola proposed a pilot operated compact valve with fast response and high flow for its size [19]. The valve consisted of a solenoid actuated 3/2 spool valve that was used to control the main valve. The valve was designed for a flow rate of 9 lpm at a pressure drop of 3.5 MPa. A spool type pilot stage utilized clearance seals but also improved leakage by adding a seal seat on one end. This allowed the benefits of large flow at small displacement inherent in spool elements, but also improved upon their poor leakage characteristics. The main stage used a poppet ground from a bearing to seal the main stage. The design achieved a closed state leakage of 0.02 lpm at a supply pressure of 10 MPa. Increases in leakage in the pilot stage were reported when the main stage was open. As demonstrated by other electromagnetic coil work, a large current of 39 A for the 73 turn pilot stage was required. The pilot stage was capable of a response time of 0.4-0.5 ms, which resulted in a main stage 90% open response time of 0.9-1.3 ms. Although the poppet provides improved sealing, it does not provide a linear transition event, as shown by oscillations in their opening transition. This would add a level of complexity if this valve was used in an SIHS because known transition behavior is important in the prediction of inertance tube transients.

Sell, Johnston, Plummer and Kudzma proposed a position controlled multi-stage digital hydraulic valve with design considerations specifically for use in a switched inertance hydraulic system (SIHS) [20]. The valve was a three stage design, using a Moog E050-099 servo valve as the actuation stage. The second stage spool drove a rod which was threaded to and drove the third stage. To take advantage of positive sealing, O-rings were used to prevent external leakage. The main stage consisted of multiple annuluses to allow a large flow area at low spool displacement. The valve achieved a flow rate of approximately 50 lpm at a pressure drop of 1 MPa with transition times near 0.5 ms. This valve was capable of the critical design criteria, but efficiency operation was not a large consideration in the design. Inherently, servo valves have low efficiencies caused by the inherent leakage in the pilot stage and compounding of energy losses in multiple stages. Discussed in the work are the challenges of manufacturing the tight tolerances

required for clearance seals, as discussed in other designs. The manufacturing challenge was compounded by use of multiple grooves with designed zero lap.

Multistage valves are typically expensive, bulky, and complex to manufacture. Their efficiencies are generally low due to loss compounding. They do however, offer many benefits when enabling flow magnification from a high-speed low flow pilot stage to subsequent stages.

This section provided an overview of work in high-speed valves including solenoid valve, rotary valve, and multistage valves. The subsequent section will provide a review of switch-mode circuit studies.

1.2.2. Switch Inertance Hydraulic Systems

Switch inertance hydraulic systems provide the opportunity for improved hydraulic circuit efficiency over throttling valve control. Two common SIHS are the pressure buck converter and the pressure boost converter. A brief review of these two circuits is completed in this section.

Pan, Johnston, Plummer, Kudzma, and Hillis presented an analytical and experimental study of a pressure buck converter, which they referred to as a flow booster [21]. Figure 1.5 presents their hydraulic schematic and equivalent electrical circuit. The system results in a lower load pressure and higher flow rate reaching the load, compared to the supply. Using a frequency domain distributed parameter model, their results at 100 Hz and a duty cycle of 0.9, showed a potential delivery flow rate 6 times that of the supply flow rate. Their experimental results demonstrated agreement at lower switching frequencies, but for repeatable experimentation the experimental test used a Parker DFplus proportional control valve which was not capable of very high frequencies. To accomplish a short switching time, system demands were sized for a valve open area of 20% which occurred at 2 ms. The system accomplished an efficiency of 50-80%, but with higher switching frequencies and shorter inertance tubes, these values have potential for improvement.

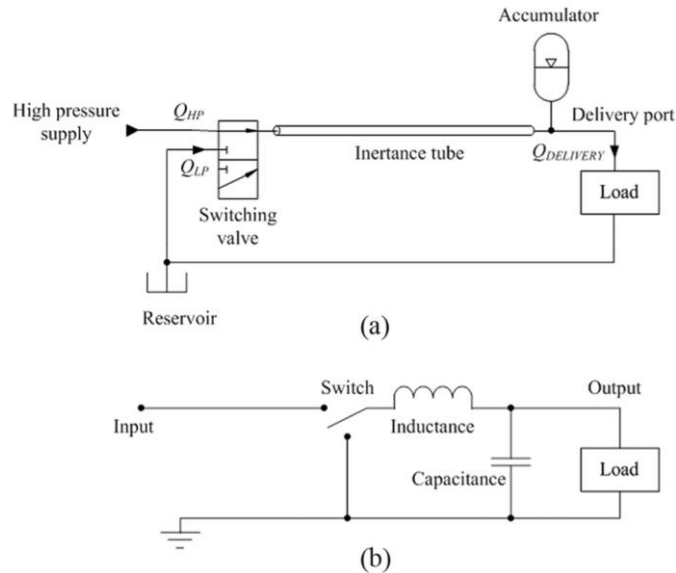


Figure 1.5. Pan et al, Pressure buck converter hydraulic system and electrical analogue [21]

Relocating the inductive component upstream of the switching valve results in another SIHS topology referred to as a pressure boost converter. De Negri, Wang, Plummer, and Johnston proposed a model for predicting behavior in a step-up switching converter [22]. The model showed promising potential with a 75% efficiency at a boost ratio of 2.5. The model further predicted the requirement for a 100 Hz switching valve to reach peak load pressures. An alternative to a long inertance tube inductive element was proposed by Wang, Gu, and Chen [23]. In place of using fluid inertance, a hydraulic motor with a flywheel was placed upstream of the switching valve. The rotational inertia of the flywheel increased when the valve was open to tank, and decreased when the valve switched to load. With a supply pressure of 5 MPa, a flywheel and motor inertia of $0.324 \text{ kg}\cdot\text{m}^2$, and a duty cycle of 0.7, the experimental setup was capable of a load side pressure of 11.6 MPa.

Work has been completed that demonstrates the capabilities of SIHS using high-speed valves. This includes hydraulic transformers consisting of pressure buck converters and pressure boost converters. The contributions of this thesis will further provide an experimental demonstration of a pressure boost converter in chapter 4 with use of a high-speed valve prototype. The subsequent section will provide a brief overview of the contributions that are presented.

1.3. Overview

This chapter presented background information as well as a review of relevant research on high-speed hydraulic valves and switched inertance circuits. The subsequent chapters provide an overview of the contributions of the thesis work. Chapter 2 presents a valve model for designing a dual spool crank-slider valve with desirable characteristics for use in switch-mode circuits. Chapter 3 presents the resulting fabricated valve prototype and provides a brief comparison of the analytical calculations with the experimental results. Chapter 4 demonstrates the use of the high-speed valve prototype in a pressure boost converter and presents the results. Chapter 5 presents an overview of the contributions and suggests future relevant work.

2. Valve Design & Optimization

2.1. Introduction

A key component to switch-mode circuit efficiency is the high-speed valve. A high performance circuit, defined by a fast response time and a low flow ripple, requires a fast valve switching frequency. However, a fast switching frequency creates three main challenges. First, high frequency valves typically use a low mass switching element to minimize the inertial actuation forces. The low mass typically correlates to a small flow area, requiring a balance between fully-open throttling loss and inertial force. Second, each switching event results in throttling across the partially-open transitioning valve. This energy loss can be minimized through soft switching [24, 25] or by reducing the valve transition time, at the expense of increasing the velocity of the switching element. Finally, each switching cycle incurs losses due to compressing and decompressing the fluid in the switched volume. The compressible energy loss can be minimized by reducing the switched volume between the valve and the inductive element.

In this chapter, a novel high-speed valve for switch-mode control is presented. The design and optimization methods are presented in section 2.2 followed by the resulting optimized valve presented in section 2.3. A discussion and conclusion are presented in section 2.4.

2.2. Methods

The design objective is to develop an energy efficient valve that can be used for experimental switch-mode hydraulic circuit studies. The valve must have fast transition times with an adjustable duty cycle and operate at flow rates and pressures suitable for laboratory benchtop testing. An overview of design constraints, architecture design, valve model, design tradeoffs, and drive mechanism are presented in this section.

2.2.1. Design Constraints

A specific set of operational criteria was selected for the valve and these design constraints were fixed throughout the design process. The following constraints were used to drive the valve design and the selection of the valve architecture.

The design flow rate and maximum pressure were selected as 22.8 lpm and 34.5 MPa respectively, based on the capabilities of the available hydraulic power unit (HPU). The target pressure drop through the valve in the on-state, at the rated flow, was 0.345 MPa, which correlates to a 1% loss of the rated source pressure. The target maximum operating frequency of the valve was 120 Hz. This cyclic rate allows operation in the range of switching frequencies above and below the natural frequency of laboratory scale inertance tubes in a switched inertance hydraulic system topology [8].

The valve is determined to be in the 'on' state when the pressure drop across the active flow path is less than 0.345 MPa at rated flow. The transition time is the time required to transition from a blocked state (orifices fully blocked) to the on-state. A transition ratio parameter was defined as the ratio of transition time to switching period. A transition ratio of 5% was selected to diminish transition throttling losses and allow for a duty cycle, as defined as the ratio of port on time to cycle time, greater than 0.9 based on two transition periods per valve switching period.

A method for continuous duty cycle adjustment from 0 to 0.9 with the valve in the non-operational state was required. To prevent cross porting, a valve overlap was required.

Other considerations included that the valve needed to use manufacturing techniques that could be completed in a standard machine shop with readily available materials.

2.2.2. Architecture Design

In this section, the conceptual design of the valve is presented, specifically, the valve operation, switching element selection, and overall valve architecture.

High-speed valve designs reported in the literature include: solenoid valves [10, 12, 13, 14], continuously rotating axial and radial flow valves [15, 16, 17, 26, 27], and multistage valves [18, 19, 20]. The operating parameters of several of these designs is presented in Table 2.1.

Table 2.1. Novel valve performance capabilities

<u>Source</u>	<u>Architecture</u>	<u>Transition Time</u> <u>(ms)</u>	<u>Flow rate (lpm), Pressure</u> <u>Drop (MPa)</u>
Noergaard, et al. [14]	Solenoid	1.5	600, 0.05
Tu, et al. [17]	Rotary	2.8	40, 0.62
Sell, et al. [20]	Multi-Stage	0.5	50, 1

A benefit of a continuously rotating valve element over one that axially translates is a reduction in inertial forces once the valve is accelerated to its operational frequency. However, a translating valve can be designed to maximize the velocity during valve transition, decreasing the average viscous friction losses as well as the transition times compared to a constant angular velocity. Based on these tradeoffs the axially translating element was selected for this valve design.

There are many methods for driving a linear translating element, such as, electromagnetic (solenoid), piezo-electric, and mechanical to name a few. As discussed, there are not currently any readily available commercial valves that meet all of the design requirements. For this reason, a custom mechanical actuation method was selected. This narrowed the selection to a cam driven or crank-slider driven element. Although cams can provide unique velocity profiles that can be beneficial in reducing the transition time, the combination of a requirement for force or form closure and complexity of manufacturing led to the selection of the 4-bar crank-slider drive mechanism.

The next step in the valve architecture layout was the selection of the switching element. Based solely on volumetric efficiency and discrete operation, a positive sealing element such as a plunger, poppet, or ball are good options. With the large number of cycles and the potential for high impact energy, there were concerns that the valve seat would wear rapidly resulting in non-constant transition events. In addition these types of elements can be challenging to pressure balance. Another common switching element used in hydraulic valves is a spool. Spools offer robust and repeatable operation and although clearance seals decrease volumetric efficiency, with

reasonable machining tolerances the leakage can be brought into an acceptable state, as discussed in section 2.2.3. For this reason the more predictable transition behavior of a spool outweighed the benefits of a positive sealing element.

A 3-way spool valve allows flow to be directed between a single inlet (source) and two outlets (A-B). If the spool is moving sinusoidally and the valve transition is located at the center of the spool displacement, the connection time will be equally split between the two ports. If the flow from port A-B is split again between two potential outlets, in this case tank and load, an adjustable duty cycle can be obtained by controlling when the tank to load transition occurs. This is equivalent to a three-position three-way valve supplying a three-position five-way valve. The center position refers to when all ports are closed during transition. This valve architecture along with an equivalent hydraulic symbol are presented in Figure 2.1.

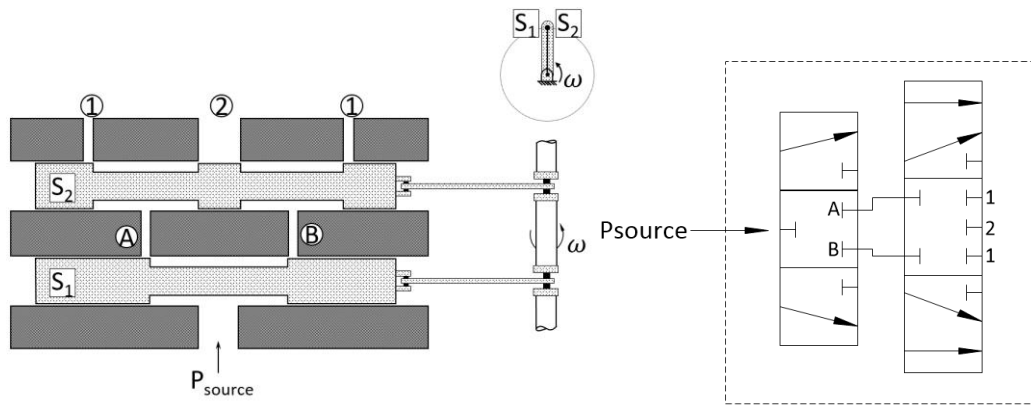


Figure 2.1. Crank-slider valve base architecture

The spools S_1 and S_2 translate axially in the fixed valve housing, allowing connection of alternating ports in the housing. The spools are driven by a common crank-shaft which ensures fixed relative position of the crank arms. Spool S_1 switches the source flow between internal ports A and B, while spool S_2 alternates between connecting A to outlet port 1 and B to outlet 2 and vice versa. Both outlet ports labeled 1 would be connected either internally or externally to the valve, behaving as a single outlet. The axial location of a spool in the blocking position is referred to as the neutral position. Figure 2.1 displays the spools as critically lapped, which

prevents cross porting during transition. It is possible to decrease the spool open length to create an overlapped valve transition.

Valve duty cycles from 0 to 100% can be achieved by adjusting the phase angle between the spools from 0 to π radians. This phase shift modulation approach allows continuous adjustment of duty cycle and results in two switching cycles per revolution of the crank arm. Figure 2.2 demonstrates the flow path through the valve for a crank arm phase shift of ϕ radians, when spool S_1 is displaced by $\theta_1 = \frac{\pi}{2}$ radians. The flow path from the source is through internal port A and then to outlet port 2. At this instance, internal port B is blocked, and as a result there is no flow through either outlet port 1. Figure 2.3 shows the valve displacements and resultant flow paths over a full crank rotation when, spool S_2 leads spool S_1 by the same ϕ radians shown in Figure 2.2. With reference to the ‘Flow path Area’ subplot, the flow is directed to outlet port 2 for a crank angular displacement equal to the ϕ radian phase shift.

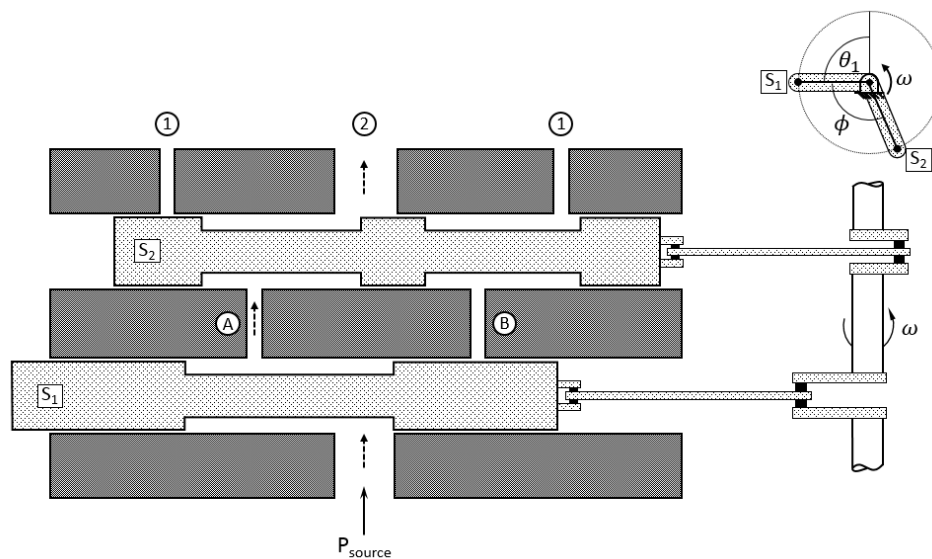


Figure 2.2. Valve depicted at angular displacement of $\pi/2$

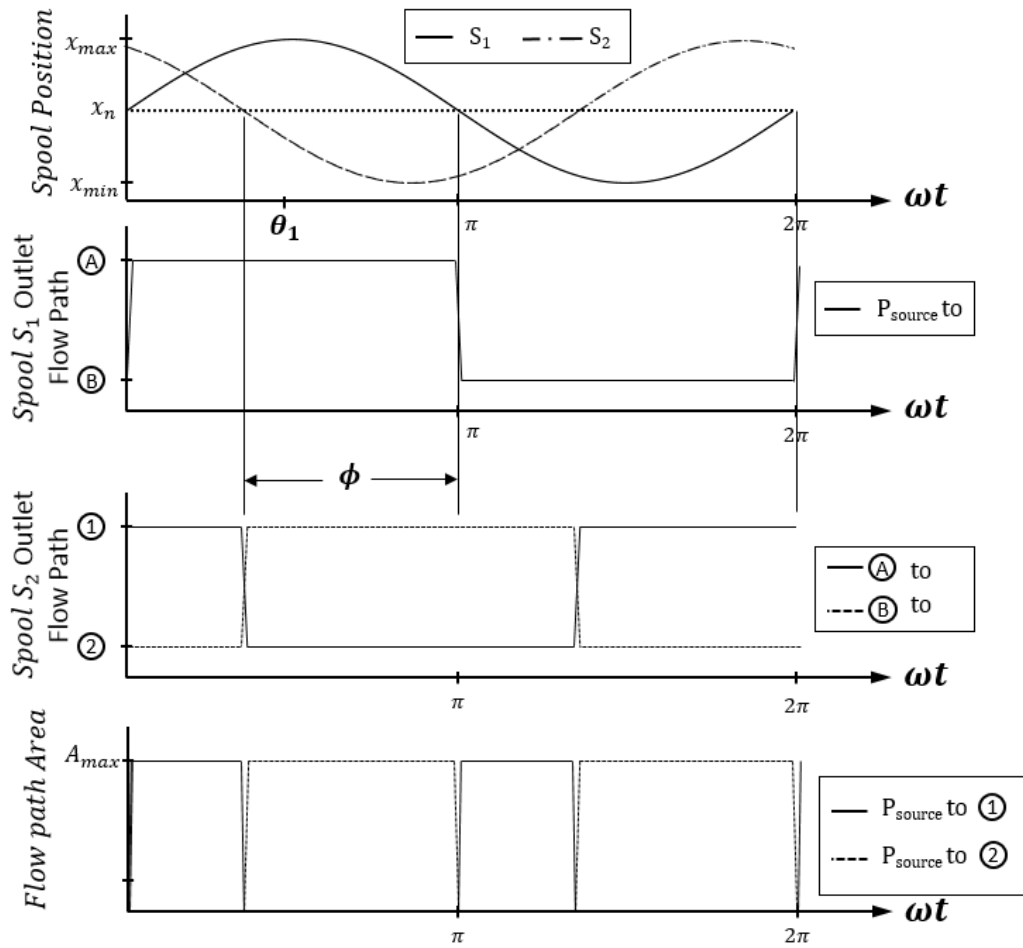


Figure 2.3. Example of how a phase shift affects duty cycle

The phase shift can be varied from 0 to π radians, resulting in outlet port 1 duty cycles described by:

$$D = \frac{\pi - \phi}{\pi} \quad (2.1)$$

where D is the duty cycle of outlet port 1, and ϕ is the phase shift between the two spools. In a critically lapped valve with non-instantaneous transition, a duty cycle of 1 cannot be achieved due

to each spool passing through a blocking state on each switching cycle. In this case, the duty cycle is reduced by the ratio of transition time to valve cycle time.

A four bar crank-slider drive mechanism was selected to actuate the spool element based on its robust high-speed operation. The drive mechanism along with an equivalent kinematic diagram are presented in Figure 2.4.

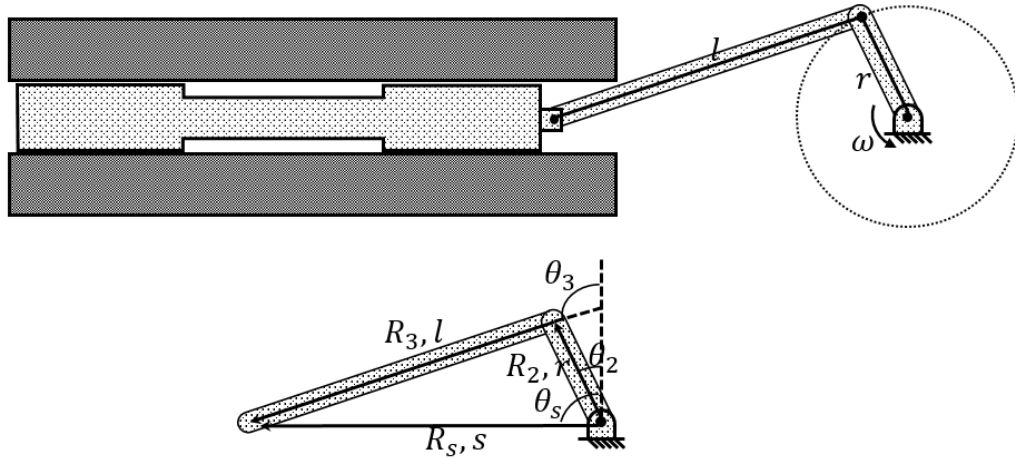


Figure 2.4. Crank-slider vector loop convention

The vector loop for the kinematic diagram can be expressed as:

$$\overline{R_2} + \overline{R_3} - \overline{R_s} = 0 \quad (2.2)$$

where $\overline{R_s}$ represents the vector from the crank pin to the wrist pin. Breaking the vectors into their respective x and y components, and rearranging the loop provides a solution for the two unknowns (s, θ_3):

$$\theta_3 = \text{acos}\left(\frac{-r\cos(\theta_2)}{l}\right) \quad (2.3)$$

$$s = r\sin(\theta_2) + l\sin(\theta_3) \quad (2.4)$$

Taking the derivative of the vector loop equation and separating the result into x and y components, provides solutions for the two velocity unknowns (ω_3 , \dot{s}):

$$\omega_3 = \frac{-r\omega_2\sin(\theta_2)}{l\sin(\theta_3)} \quad (2.5)$$

$$\dot{s} = r\omega_2\cos(\theta_2) + l\omega_3\cos(\theta_3) \quad (2.6)$$

When the length of the coupler link, l , is long relative to the crank link, r , the spool has a near sinusoidal displacement with a maximum absolute spool velocity occurring near the crank arm perpendicular position. As the valve transition time is dependent on the spool velocity during the port switching, the transition time is minimized by having the valve spool transition from one port to the other at the peak spool velocity. After transition, the spools decelerate to zero velocity at the ends of their travel. The nature of the slider link velocity profile accomplishes two design goals: 1) Transition at maximum spool velocity to minimize throttling losses and 2) Reduce velocity outside of transition periods to reduce frictional and viscous losses. A flywheel on the crank-shaft stores kinetic energy when the spool is decelerating and releases the energy during spool acceleration, improving the valve actuation efficiency.

A ported sleeve design was selected, where the valve spool translates within a sleeve placed in the valve block. The sleeve has rows of radially drilled ports, which are covered and uncovered by the lands on the spools. Ports in the valve block distributed circumferentially around the sleeve balance the pressure and flow forces on the spool.

In the next section a valve efficiency model will be discussed and presented.

2.2.3. Valve Model

Post design constraint specification and base valve architecture selection, relationships were created between component dimensions and valve energy losses. Mapping these trade-offs

allowed a selection of dimensions which yields the highest energy efficiency. This section will present the optimization method utilized and the subsequent section will present the tradeoff comparisons.

The throttling energy losses through the valve were divided into primary and secondary losses. The primary losses consisted of the throttling energy dissipation through the sleeve ports, which must be small in diameter for fast valve transition. The secondary losses consisted of the pressure loss at the external valve ports, circumferential flow around the sleeve, and axial flow along the spool within the sleeve. The secondary losses are dependent on the dimensions of the spool and porting within the housing and have an inverse relationship with switched volume. This tradeoff is discussed later in this section.

The pressure drop through each row of ports in the sleeve is described as:

$$\Delta P = \frac{\rho}{2} \left(\frac{Q}{C_d A_o N} \right)^2 \quad (2.7)$$

where N is the total number of radial orifices in a row, ρ is the density of the hydraulic fluid, Q is the volumetric flow rate, C_d is the discharge coefficient and A_o is the open area of a single orifice.

During transition, the spool land covers or uncovers a row of circular ports. The area of the port orifices is a function of the axial spool position, as shown in Figure 2.5.

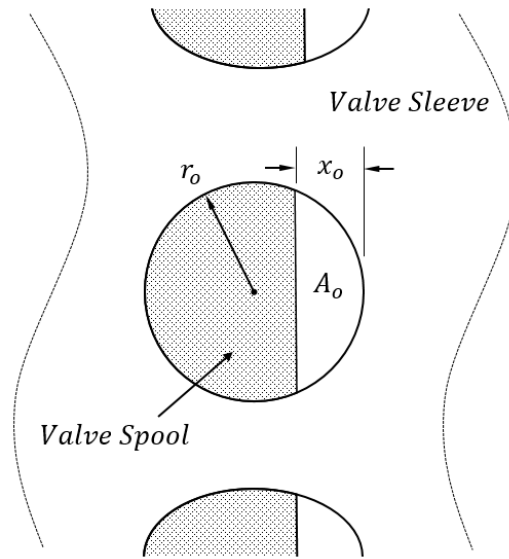


Figure 2.5. Port orifice area during valve transition

The open area of an individual port is:

$$A_o = r_o^2 \cos^{-1} \left(\frac{r_o - x_o}{r_o} \right) - (r_o - x_o) \sqrt{2r_o x_o - x_o^2} \quad (2.8)$$

where r_o is the port radius and x_o is the distance between the spool land (spool neutral position) and the open edge of the orifice.

With reference to Figure 2.6, each flow path passes through four orifice port banks, with the orifice areas designated A_1 closest to the source of flow through A_4 at the outlet. The port banks are in series, thus the pressure drop through these orifices is equal to the sum of the pressure drop through each row of ports as shown in Eqs. (2.9), (2.10), (2.11).

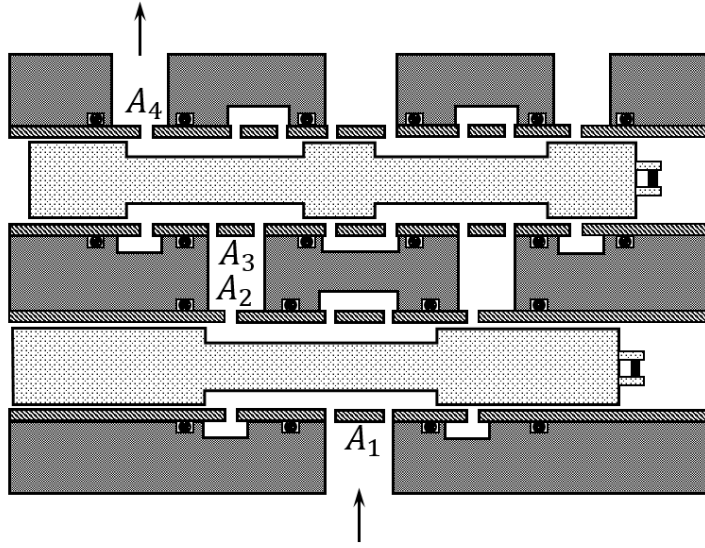


Figure 2.6. Effective area for a single flow path

$$\Delta P = \frac{\rho Q^2}{2C_d^2} \left(\frac{1}{(A_1 N_1)^2} + \frac{1}{(A_2 N_2)^2} + \frac{1}{(A_3 N_3)^2} + \frac{1}{(A_4 N_4)^2} \right) \quad (2.9)$$

$$\Delta P = \frac{\rho Q^2}{2C_d^2 A_{eff}^2} \quad (2.10)$$

$$A_{eff} = \left(\frac{1}{(A_1 N_1)^2} + \frac{1}{(A_2 N_2)^2} + \frac{1}{(A_3 N_3)^2} + \frac{1}{(A_4 N_4)^2} \right)^{-0.5} \quad (2.11)$$

where A_{eff} is the effective area of the four banks in series. Orifice areas A_2 and A_4 are described by Eq. (2.8) during transition, while areas A_1 and A_3 are never blocked by the valve spool, so thus are the area of the circular ports. A_1 and A_3 are composed of two rows of orifices to further reduce the pressure drop within the flow path, simplifying the effective area to:

$$A_{eff} = \left(\frac{2}{\left(\frac{\pi d_o^2}{4} 2N\right)^2} + \frac{1}{(A_2 N)^2} + \frac{1}{(A_4 N)^2} \right)^{-0.5} \quad (2.12)$$

The greatest pressure drop scenario occurs when both spools are in phase and moving through the neutral position. At this time, the port banks designated A_2 and A_4 are partially blocked simultaneously. A similar condition occurs when the spools are π radians out of phase. At other phase shifts, only one bank of ports transitions at a time. The following analysis assumes that the spools are in phase.

For ease of manufacturing, the ports in a row are spaced 30% of their diameter away from each other circumferentially, as seen at the inside wall of the sleeve. In this way, the inside circumference of the sleeve and thus diameter of the spool becomes a function of the number and diameter of ports in a particular row:

$$d_{spool} = \frac{1.3Nd_o}{\pi} \quad (2.13)$$

where d_{spool} is the diameter of the spool. As the number and diameter of sleeve ports increases, the pressure drop across the valve for a given spool position decreases. Increasing N and d_o also increases the required diameter of the spool per Eq. (2.13) which comes at the cost of increased leakage flow through the clearance seal between the sleeve and the spool based on a parallel plate approximation of the annulus:

$$Q_{leak,pp} = \frac{\pi d_{spool} c^3 \Delta P}{12\mu L_{leak}} = \frac{\pi d_{spool} c^3 \Delta P}{12\mu x(\theta)} \quad (2.14)$$

where ΔP is the pressure difference between the pressurized flow and ambient, μ is the dynamic viscosity of the hydraulic fluid, and L_{leak} is the length of the leakage path. In all cases, the leakage flow was evaluated with $\Delta P = 34.5 \text{ MPa}$. The value of c is limited by achievable machining tolerances.

There are four major leakage paths as indicated in Figure 2.7. L represents the leakage path length with the subscripts representing the four leakage paths. *Leak1* is the path from source to the second low pressure outlet port. *Leak2* represents the path from source to external ambient and the length is the full endland length. *Leak3* and *leak4* represent back flow from the pressurized load port to the low pressure outlet ports.

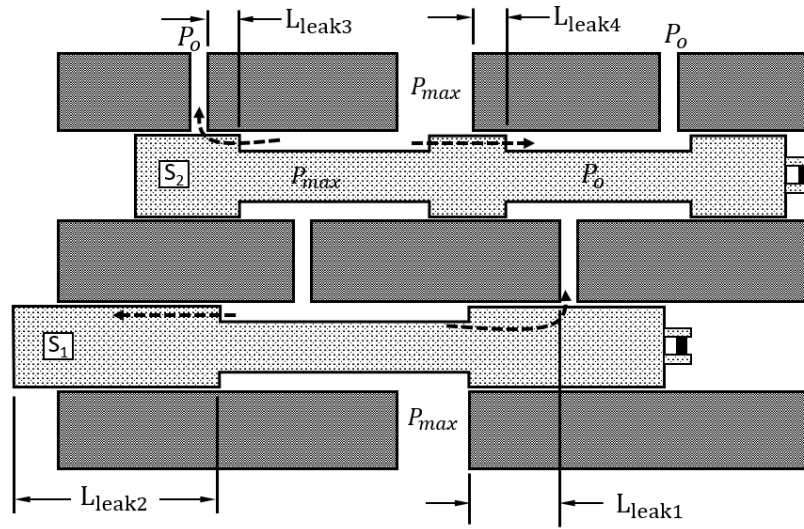


Figure 2.7. Valve diagram showing major leakage paths

When a spool is at zero displacement, the leakage predicted by Eq. (2.14) is infinite. To address this, the leakage flow model is switched to an orifice equation, based on the annular clearance area around the spool, once the flow predicted by the parallel plate leakage exceeds the flow predicted by the orifice model:

$$Q_{leak,o} = C_d A_{annulus} \sqrt{\frac{2\Delta P}{\rho}} = C_d (\pi d_{spool} c) \sqrt{\frac{2\Delta P}{\rho}} \quad (2.15)$$

Valve leakage to ambient is controlled by increasing the length of the lands at the ends of the spools. The length of the lands is penalized by increased viscous power dissipation in the fluid in the clearance between the spool and the sleeve. The viscous friction force is calculated with a parallel plate approximation of the annulus, and the force is calculated from shear stress from Couette flow:

$$F_{vis} = -\pi d_{spool} L \mu \frac{v(\theta)}{c} \quad (2.16)$$

where F_{vis} is the viscous friction force and L is the total length of the spool lands.

This section presented a model for calculating the fully open throttling losses, leakage losses, and viscous friction losses. The subsequent section will present how trade-offs between valve parameters drove the detailed design.

2.2.4. Parameter Study of Design Trade-Offs and Detailed Design

Creating tradeoff maps of the parameters presented in the previous section began with the key valve requirement that a 0.345 MPa on-state pressure drop must be achieved within 5% of the valve switching cycle at the rated flow rate. The valve crank arms are rotated via a 3600 rpm synchronous AC motor, yielding a constant angular crank velocity, $\omega = 120\pi$ rad/s. In order for the 5% transmission ratio to be met, transition to the on-state must occur prior to an angular crank displacement of $\pi * 0.05 = 0.157rad$ with respect to the neutral position. Equation (2.4) yields an axial spool displacement for angular displacement in terms of crank length and coupler length. The l/r ratio of coupler length to crank link length is assumed to be five as a reasonable tradeoff between compactness and transmission angles. Rearranging Eq. (2.4) to solve for the spool position relative to the neutral or center location, at 0.05π angular displacement and an l/r ratio of five yields:

$$x(0.05\pi) = 0.1589r \quad (2.17)$$

Defining the on-state pressure drop as 0.345 MPa enabled calculation of the required effective area as shown in Eq. (2.10). The total effective area is a function of the spool location with respect to the neutral position, the orifice diameter, and the number of orifices in a row. Selecting an orifice diameter and the number of orifices in a row enabled calculation of the required spool displacement with respect to neutral, x , as shown in Eqs. (2.8), (2.11). The required displacement was used to determine the required crank length as shown in Eq. (2.17). Figure 2.8 shows the required crank link length to achieve 5% transition for a range of orifice diameters and number of orifice ports in an individual row.

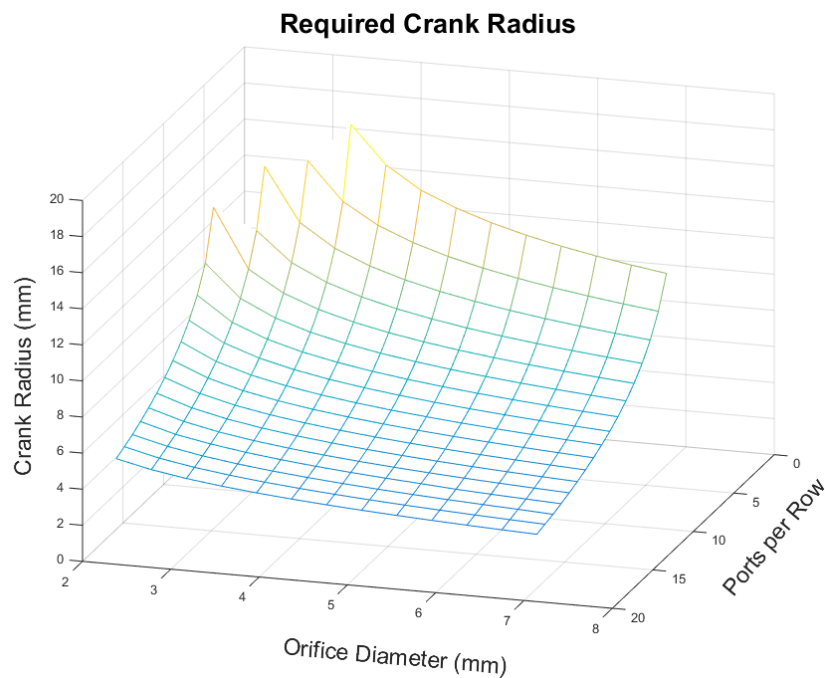


Figure 2.8. Relationship between number of ports in a row and the diameter of the ports vs. the required crank length to achieve a 5% transition ratio

The peak spool velocity over a cycle increases as crank length increases, per Eq. (2.6) resulting in higher viscous friction forces, per Eq. (2.16). The clearance c can be increased to reduce the friction forces, but at the cost of increased leakage, per Eq. (2.14) and (2.15). Summing the viscous and leakage energy losses over a cycle results in the total energy loss, E_{loss} :

$$E_{loss} = \frac{1}{\omega} \int_0^{2\pi} \Delta P Q_{leak}(\theta) d\theta + \frac{1}{\omega} \int_0^{2\pi} |F_{vis}(\theta) v(\theta)| d\theta \quad (2.18)$$

The spool velocity, $v(\theta)$, is evaluated using Eq. (2.6). The energy loss for a given crank length is plotted in Figure 2.9 when spool land lengths are assumed to be $1.5*r$.

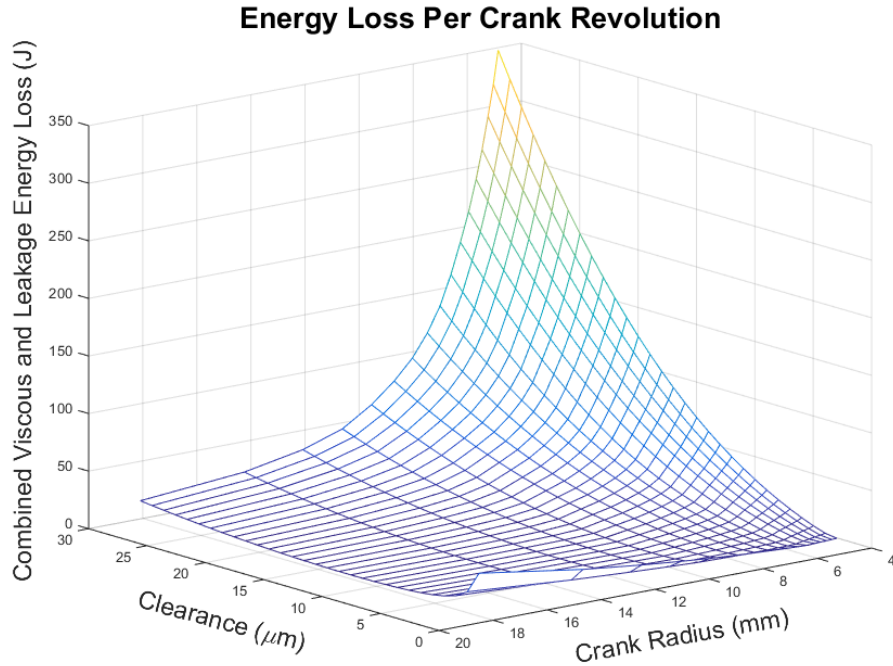


Figure 2.9. The effect of crank length and radial clearance, on energy losses over a cycle

Figure 2.9 indicates that clearances should be minimized until a clearance value of $2 \mu\text{m}$, at which value viscous friction becomes the major loss mechanism. The practical values of the radial clearance between the spool and sleeve are limited by manufacturing tolerance, and $10 \mu\text{m}$ was selected as a minimum achievable value. As the valve lands increase in length, there is an increase in viscous forces per Eq. (2.16), but a reduction in leakage loss. Figure 2.10 illustrates this relationship, with a $10 \mu\text{m}$ radial clearance applied.

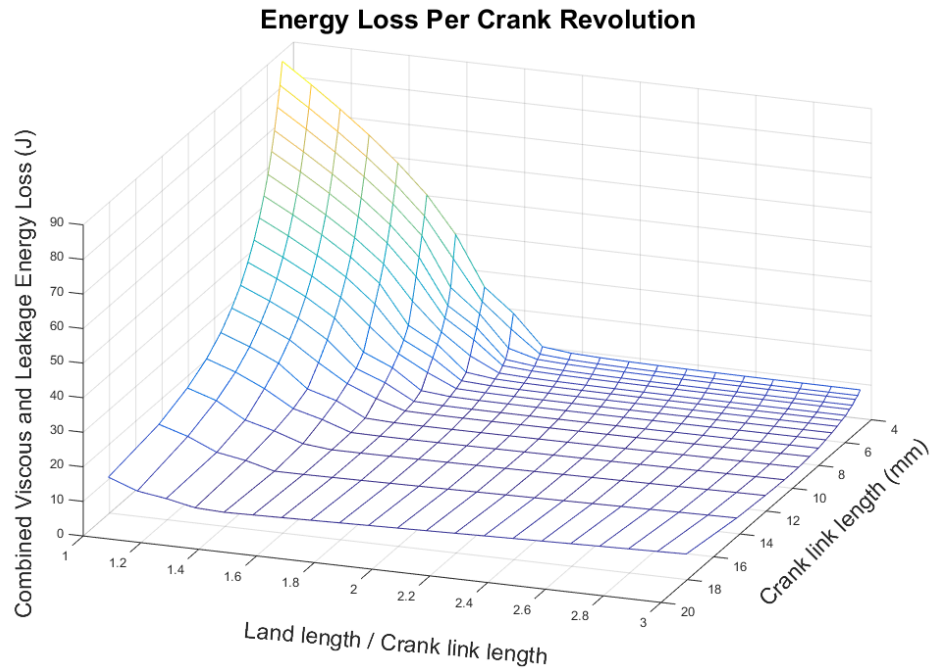


Figure 2.10. Energy loss over a cycle vs. the crank length and non-dimensionalized spool land length

In Figure 2.10, the lowest per cycle losses are achieved for all crank link lengths when the spool land lengths are two times the length of the crank link. Energy loss as a function of crank length was then re-calculated while constraining the land length to twice the crank length and the radial clearance to 10 μm . The resultant energy losses as a function of crank radius are presented in Figure 2.11. The optimal crank length that minimized energy loss over a full crank rotation was 11.43 mm. At short crank lengths, the leakage flow paths are small and leakage is the major loss mechanism. At long crank lengths, the viscous friction forces become the major loss mechanism.

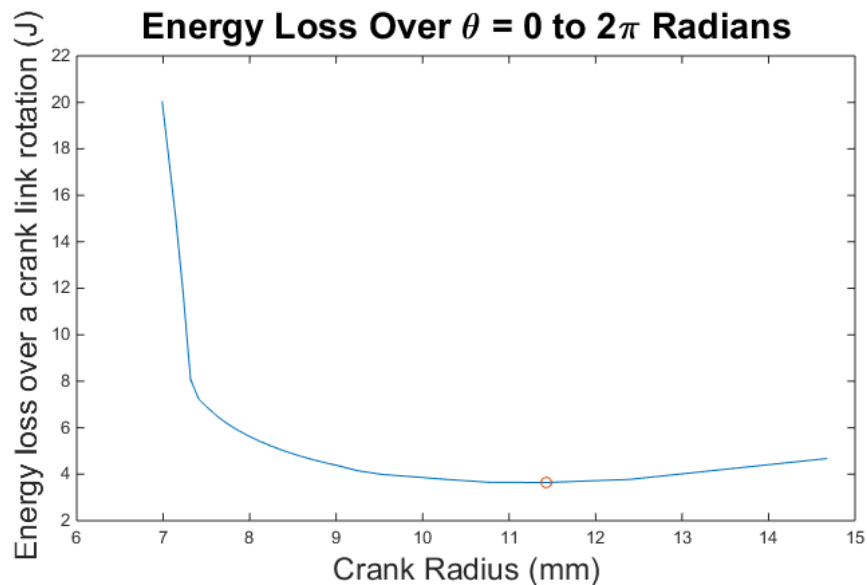


Figure 2.11. Energy loss over a cycle vs. crank link length, with optimized land lengths of two times the crank link length and a radial clearance of 10 μm

The surface generated in Figure 2.8 is referenced to find the number of ports and port diameter required for transition ratio of 5% given the optimized crank length. Eight ports per row was selected to evenly distribute radial flow into the spool grooves, and for ease of manufacturing and spool pressure balancing. With $N = 8$ ports per row, the required orifice diameter is 2.79 mm.

As previously mentioned, the throttling losses through the sleeve orifices are considered the primary losses and the secondary losses are all other losses along the fluid travel path from valve block entry to exit. Increasing the area of the flow path decreases these losses at the expense of increased volume, which leads to higher compressibility losses. Utilizing a typical spool valve block architecture, with a slight variation in circumferential flow galleries, the secondary loss constituents of a single flow path can be seen in Figure 2.12 and their assumed flow types are listed in Table 2.2.

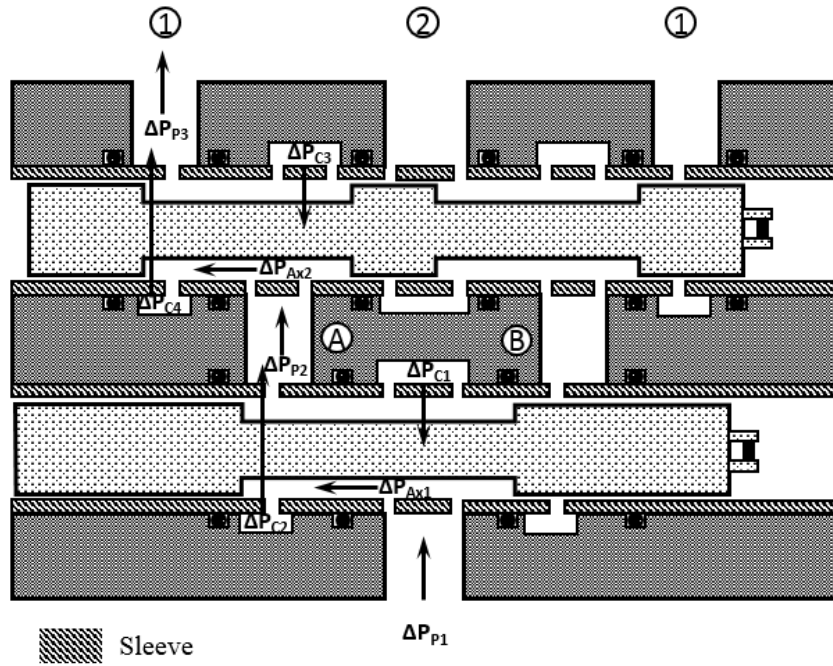


Figure 2.12. Secondary throttling loss components of a single flow path

Table 2.2. Flow types of secondary losses

Secondary Loss	Flow Type
$\Delta P_{p1}, \Delta P_{p2}, \Delta P_{p3}$	Laminar Pipe Flow
$\Delta P_{Ax1}, \Delta P_{Ax2}$	Laminar Annular Flow
$\Delta P_{C1}, \Delta P_{C2}, \Delta P_{C3}, \Delta P_{C4}$	Laminar Flow Through Rectangular Area

To allow for manufacturing symmetry, all corresponding dimensions, such as inlet and outlet port diameters, are equal. The total secondary pressure losses are calculated as:

$$\Delta P_{sec} = 2 * \Delta P_{P1,3} + \Delta P_{P2} + 4 * \Delta P_{C1,2,3,4} + \Delta P_{Ax1} + \Delta P_{Ax2} \quad (2.19)$$

where the subscript P represents the port losses, C the losses flowing circumferentially around the sleeve, and Ax the axial flow losses along the spool. For circumferential flow, it was assumed

Increasing the flow area in all cases decreases the secondary throttling loss but results in an increased switched volume within the valve. To determine this trade off, the volume can be calculated by summing the port, circumferential, axial, and orifice volumes:

$$V_P = \frac{\pi d_p^2}{4} (2l_{P1,3} + l_{P2}) \quad (2.23)$$

$$V_C = 4\pi w_c (h_c^2 + 2r_{SL,o} h_c) \quad (2.24)$$

$$V_{Ax} = \pi (r_{SL,i}^2 - r_{SP,c}^2) (l_{Ax1} + l_{Ax2}) \quad (2.25)$$

$$V_O = 1.5N d_o^2 t_s \quad (2.26)$$

The valve block external dimensions were selected based on centered valve sleeves with allowance for -06 ORB ports on the inlet and outlet. The port diameter selected was slightly larger than the inner diameter of a -06 ORB fitting to allow for smooth flow transition. The circumferential groove width around the sleeves was selected to accommodate the double orifice rows in the sleeve. The center length of spool 1 was extended to allow for straight porting between the two blocks. The remaining dimension was the depth of the circumferential flow groove. Figure 2.14 represents the trade off in pressure drop based on circumferential flow gallery depth, along with the resulting valve dead volume.

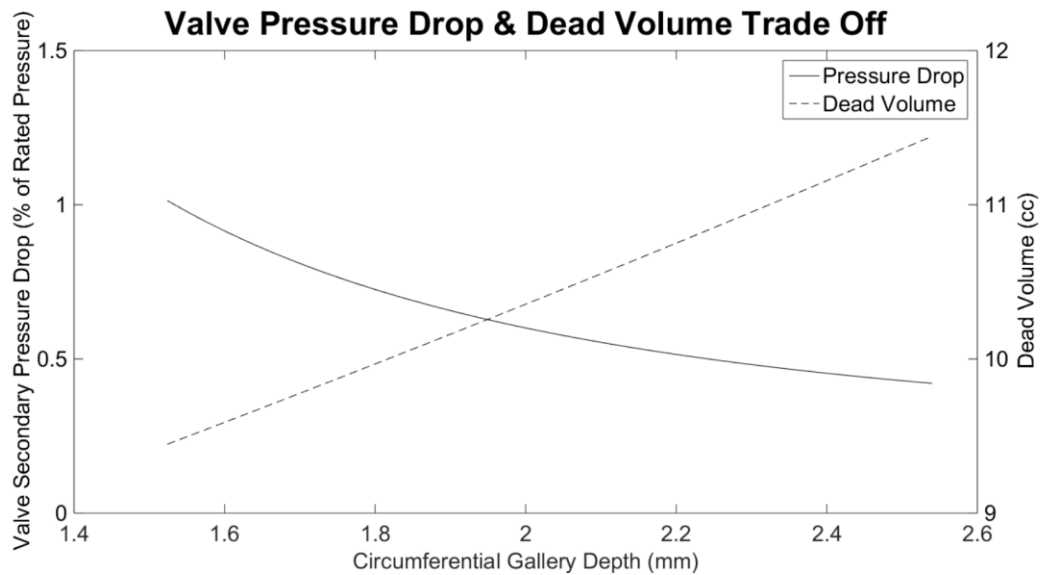


Figure 2.14. Resultant secondary pressure drop while varying circumferential flow gallery depth

Based on preventing the secondary losses from exceeding the primary losses (1% of rated pressure) and results from the boost circuit distributed parameter model constructed by Alexander Yudell that indicated an improvement in efficiency of 4% when the dead volume is reduced from 20 cc to 10 cc, 1.78 mm was selected as the gallery depth. This depth resulted in a 0.74% secondary pressure loss at rated flow and a valve dead volume of 9.93 cc in a single flow path.

In the detailed design, material selection for the valve components was completed. All component drawings can be found in Appendix A.1. The sleeve fits into a valve housing containing the porting and O-ring seals. To allow for easier manufacturing of the O-ring grooves and thru bore, aluminum 6061 was chosen for the valve block material. The high thermal conduction of aluminum also enables dissipation of heat generated in the valve. Buna-N O-rings were selected to seal between the valve block bore and the sleeve. To prevent thermal binding during cold startup the same material was selected for both the spool and sleeve. C11L17 steel was selected and both the spool and sleeve were heat treated to minimize wear.

This section presented the tradeoffs and selection of the valve parameters. Section 2.2.5 provides discussion of the drive mechanism analysis.

2.2.5. Drive Mechanism

A four-bar crank-slider drive mechanism was selected to actuate the spools due to its robust high-speed operation. Optimization of this mechanism is not in the scope of this thesis, but a brief overview of the kinematics and kinetics are presented in this section.

To calculate the forces in the mechanism, a kinematic analysis was completed based on the vector loop shown in Eq. (2.2). Taking the second derivative of the vector loop equation in complex notation and breaking the equation into its respective x and y components provides solutions for the two acceleration unknowns (α_3, \ddot{s}):

$$\alpha_3 = \frac{-r\omega_2^2 \cos(\theta_2) - l\omega_3^2 \cos(\theta_3)}{l \sin(\theta_3)} \quad (2.27)$$

$$\ddot{s} = -r\omega_2^2 \sin(\theta_2) + l\alpha_3 \cos(\theta_3) - l\omega_3^2 \sin(\theta_3) \quad (2.28)$$

The resultant forces in the mechanism links are determined by completing a force balance as shown in Figure 2.15, where F represents the resultant force and M represents the moment created by the friction in the joints. The force subscripts $l2$ represent the force from link l applied on link 2 . The R vectors represent the distance from the link center of gravity to the joint. The joint friction in the crank pin is assumed to be zero based on the low friction coefficient in roller bearings.

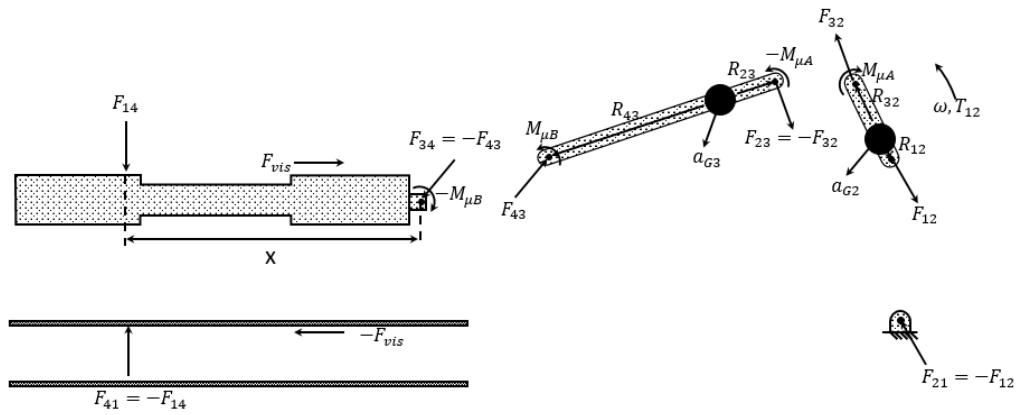


Figure 2.15. Drive mechanism force balance

Summing the x and y force components as well as the moments for each link provides the following system of equations. Where r_A represents the radius of the A joint pin that is acted on by the friction component, μ .

Link 2:

$$F_{12x} + F_{32x} = m_2 a_{G2x} \quad (2.29)$$

$$F_{12y} + F_{32y} = m_2 a_{G2y} \quad (2.30)$$

$$T_{12} + (R_{12x}F_{12x} - R_{12y}F_{12y}) + (R_{32x}F_{32x} - R_{32y}F_{32y}) + M_{\mu A} = I_{G2}\alpha_2 \quad (2.31)$$

$$M_{\mu A} = r_A \mu_A \sqrt{F_{32x}^2 + F_{32y}^2} * \text{sign}(\omega_3 - \omega_2) \quad (2.32)$$

Link 3:

$$-F_{32x} + F_{43x} = m_3 a_{G3x} \quad (2.33)$$

$$-F_{32y} + F_{43y} = m_3 a_{G3y} \quad (2.34)$$

$$(-R_{23x}F_{23x} + R_{23y}F_{23y}) + (R_{43x}F_{43x} - R_{43y}F_{43y}) - M_{\mu A} + M_{\mu B} = I_{G3}\alpha_3 \quad (2.35)$$

$$M_{\mu B} = -r_B\mu_B\sqrt{F_{43x}^2 + F_{43y}^2} * \text{sign}(\omega_3) \quad (2.36)$$

Link 4:

$$F_{14x} - F_{43x} = 0 \quad (2.37)$$

$$F_{vis} - F_{43y} = m_4a_{G4y} \quad (2.38)$$

$$F_{14x} * x - M_{\mu B} = 0 \quad (2.39)$$

There is a two way dependency between the joint friction and link forces. Utilizing an iterative solver on the system of equations provides solutions for the unknown forces that react on the joints as well as the required input torque.

A line drawing of the drive mechanism is shown in Figure 2.16. To complete the stress analysis, the material and component selection for the drive mechanism is listed in Table 2.3. The material selection was based on robust operation with easily accessible materials. A weight optimization was not completed but would likely lead to the selection of different materials. The revolute joint bearings were oil impregnated bronze 932 alloy with a yield stress of 125 MPa. The connecting rod pin for spool 1 was a TiCN-coated 18-8 SS shoulder screw. The length of the sleeve bearings drove the width of the connecting rods.

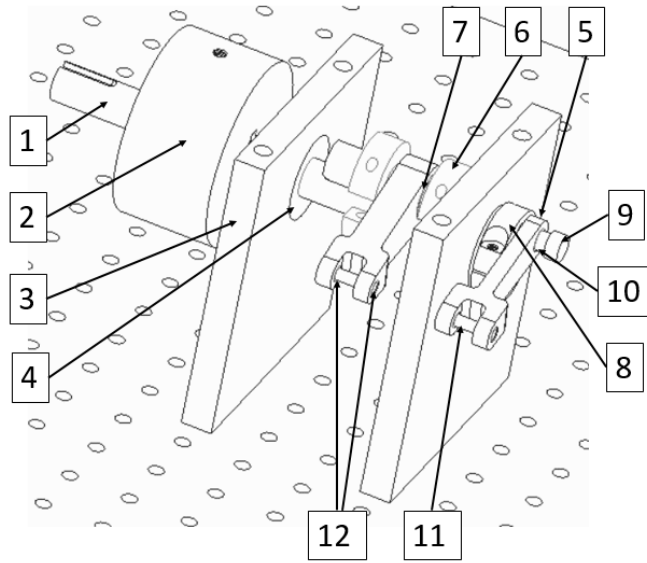


Figure 2.16. Drive mechanism

Table 2.3. Drive mechanism component materials

<u>Figure Reference</u>	<u>Component</u>	<u>Material</u>
1	Drive Shaft	1045 Ground and Polished Steel
2	Flywheel	1045 Ground and Polished Steel
3	Bearing Blocks	6061 Aluminum
4	Shaft Mount Roller Bearings	Double Sealed Steel Ball Bearing
5	Connecting Rods	1018 Steel
6	Conrod 2 Lock Collars	Black Oxide Steel
7	Conrod 2 Bearing	Alloy 932 Bronze
8	Conrod 1 Crank Collar	A-36 Hot Rolled
9	Conrod 1 Connecting Rod Pin	TICN-Coated SS
10	Conrod 1 Bearing	Alloy 932 Bronze

11	Wrist Pin	316 SS Polished
12	Wrist Pin Bearing	Alloy 932 Bronze

This section presented the non-optimized drive mechanism utilized to actuate the valve spools, with achievement of phase shift through manual adjustment of a lock collar. An active phase shift mechanism was not implemented in this iteration, but could be accomplished through the use of a planetary gear set similar to a car differential as shown in Appendix A.2. Section 2.3 presents the overall results of the valve modeling and design.

2.3. Optimized Valve Results

The process outlined in the previous section resulted in an optimal crank length, from which the sleeve port diameter was calculated, assuming eight ports per row. Table 2.4 outlines the key design parameters of the spool valve, which is capable of a 5% transition ratio at a rated flow of 22.8 lpm and rated pressure of 34.5 MPa.

Table 2.4. Valve design optimization results

<u>Attribute</u>	<u>Value</u>
Orifice Diameter	2.79 mm
Num. of Orifice, N	8 (outlet row, A ₂ , A ₄) 8 x 2 rows (inlet row, A ₁ , A ₃)
Crank Length, r	11.43 mm
Spool Diameter, d _{spool}	9.23 mm
Radial Spool Clearance, c	10 μm
Valve Dead Volume	9.93 cc

The effective area of the two outlet flow paths vs. crank link displacement at a spool phase shift, $\phi = \frac{\pi}{4}$, is shown in Figure 2.17. The dashed horizontal line in the figure indicates the effective area that results in a pressure drop of 0.345 MPa through the active flow path. The transition ratio is calculated as the time for an active flow path to achieve this effective area, divided by the valve switching frequency. For this optimized geometry, the transition ratio is 5.0%.

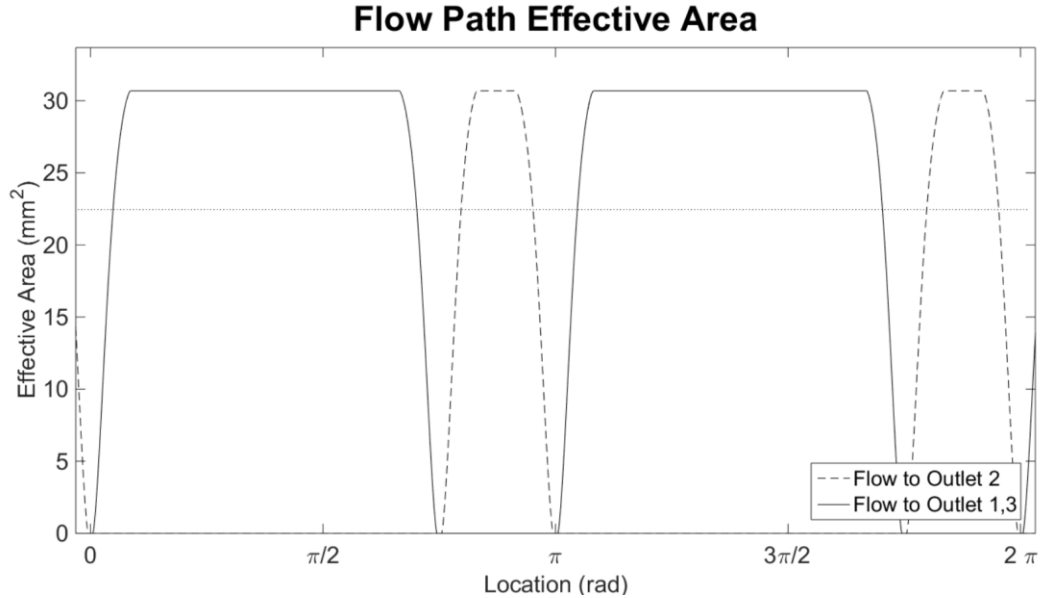


Figure 2.17. Effective area of the valve vs. crank link angular displacement when $\varphi = \frac{\pi}{4}$

The leakage and viscous friction losses are displayed as a fraction of the power at the rated flow and pressure in Figure 2.18. The peak values of leakage loss occur at the neutral points of 0 and π crank angles, which is where the shortest leakage paths occur. The viscous friction losses are proportional to the axial velocity of the spool, but are small compared to the leakage losses. When integrated over 2π radians of crank displacement at an operating frequency of 120 Hz, the energy loss due to leakage and viscous friction is 1.7% of rated flow energy over the same time.

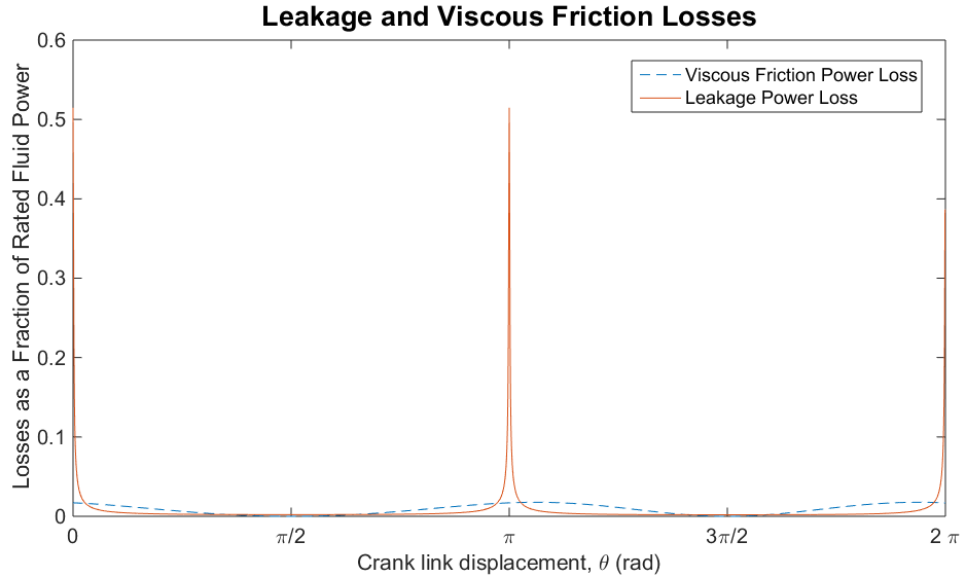


Figure 2.18. Power losses as a fraction of flow power at rated pressure and volumetric flow rate

A solid model of the valve design is presented in Figure 2.19 and all component drawings are contained in Appendix A.1. The valve block is constructed of aluminum 6061 and the sleeve and spool are constructed from C11L17 steel. The spool and sleeve were core hardened to HRC 40 and case hardened to HRC 56-59 in air to prevent the warping that can occur from oil quenching. Case hardening allows ductility retention. It is desirable to have the spool and cylinder expand equally as they come up to operating temperature during startup to avoid binding. As the block has significantly more thermal mass and will not expand as quickly during warmup, a low-mass sleeve is utilized that expands with the spool. Conversely insufficient sleeve thickness can result in expansion of the sleeve due to internal pressure, resulting in leakage. Locational control of the sleeve was accomplished via positive contact from a screw threaded through a cross member located on the back face of the valve block. Adjacent orifices are separated by O-rings installed in the block. The inlet and outlet ports are located in the top of the valve block, directed into the paper as oriented in Figure 2.19. The ports in the valve housing are annular grooves, which allow the flow to enter the circumferentially distributed sleeve ports. Both ends of the spool are exposed to ambient, which pressure balances the valve. In this design iteration, leakage flows to ambient and is collected in a reservoir.

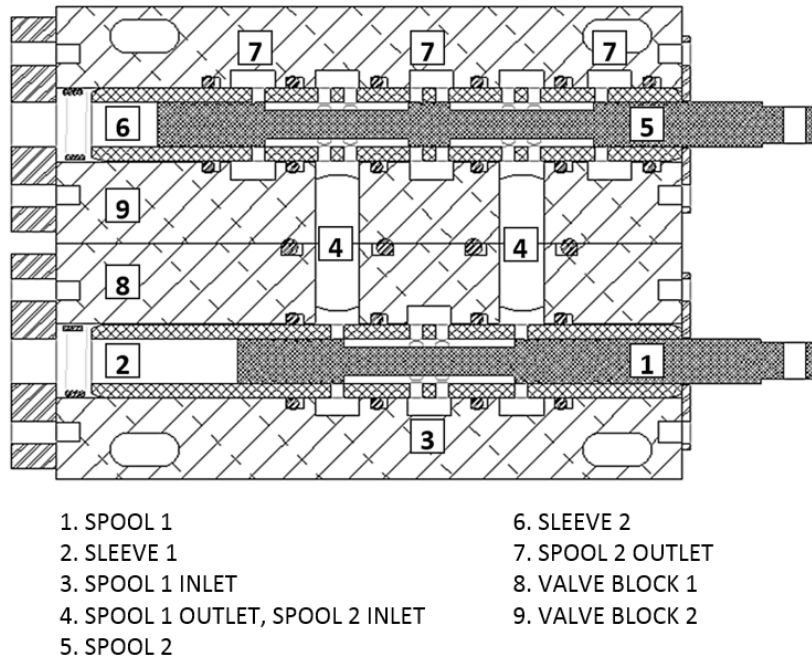


Figure 2.19. Solid model of spools and valve housing

A kinetic analysis of the drive mechanism was presented in section 2.2.5. Figure 2.20 presents the total input torque, at 377 rad/s required with both spools in phase based on linkage dimensions, as shown in Appendix A.1, and masses as listed in Table 2.5.

Table 2.5. Drive mechanism component masses

<u>Component</u>	<u>Value</u>
Coefficient of Friction in Revolute Joints	0.15
Crank-shaft Assembly	1.78 kg
Conrod 1	0.06 kg
Spool 1	0.056 kg
Conrod 2	0.1 kg
Spool 2	0.057 kg

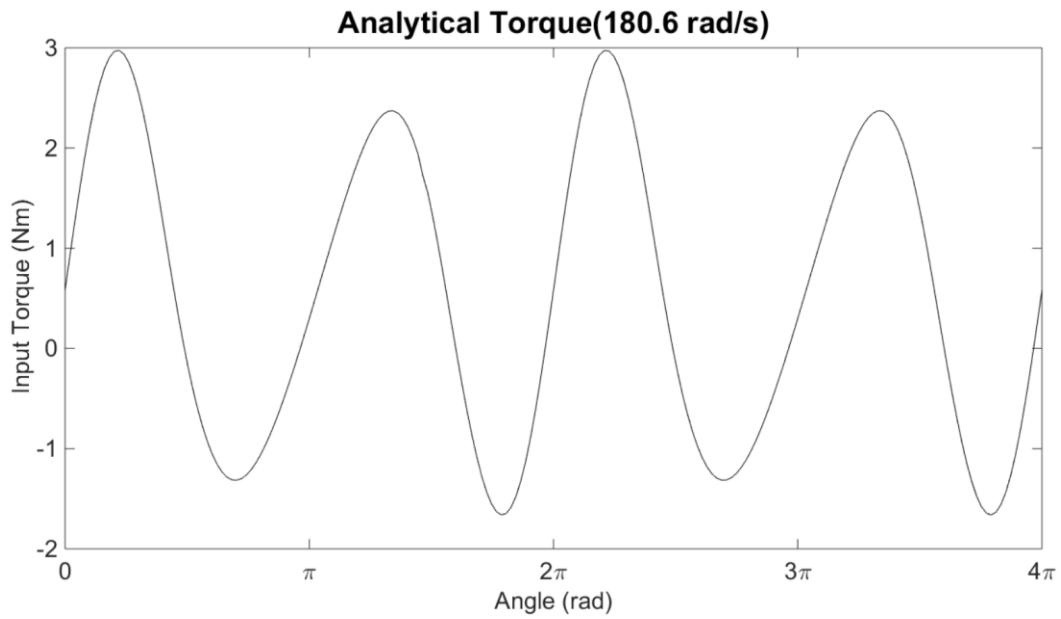


Figure 2.20. Drive mechanism required input torque

Following the kinetic mechanism analysis, a Hertzian contact stress analysis was completed for the pin and bearing in the revolute joint to verify failure would not occur. Figure 2.21 shows the resultant stresses on a revolute joint pin when a force is applied to the link.

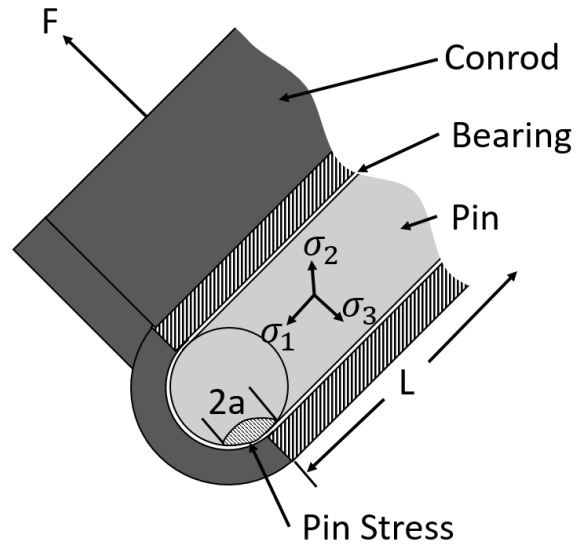


Figure 2.21. Pin and bearing stresses in revolute joint

The contact stress was calculated by first determining the deformed half-width contact surface [28]:

$$a = \sqrt{\frac{4F\left(\frac{1-\nu_1^2}{E_1} + \frac{1-\nu_2^2}{E_2}\right)}{\pi L\left(\frac{1}{R_1} - \frac{1}{R_2}\right)}} \quad (2.40)$$

where a represents the half width of the contact area between the cylindrical pin and the cylindrical bearing. ν and E represent the material Poisson's ratio and Modulus of Elasticity respectively, while the subscripts represent the pin (1) and bearing (2). L is the axial contact length and R represents the joint radius. A radial clearance of 0.127 mm between the pin and bearing was assumed. The maximum contact pressure resulting from the link force is provided by [28]:

$$P_0 = \frac{2F}{\pi a L} \quad (2.41)$$

The three principal stresses and resultant shear stresses are determined by the following equations where 1 represents the joint axial direction, 2 represents a direction perpendicular to the force vector, and 3 represents a direction opposite the force direction. z represents the depth below the pin or bearing contact surface [28].

$$\sigma_1 = -\nu(\sigma_2 + \sigma_3) \quad (2.42)$$

$$\sigma_2 = \frac{-P_0}{a} \left((a^2 + 2z^2)(a^2 + z^2)^{-1/2} - 2z \right) \quad (2.43)$$

$$\sigma_3 = -P_0 \left(\sqrt{\frac{z^2}{a^2} + 1} \right)^{-1} \quad (2.44)$$

$$\tau_1 = \left| \frac{\sigma_2 - \sigma_3}{2} \right|; \tau_2 = \left| \frac{\sigma_1 - \sigma_3}{2} \right|; \tau_3 = \left| \frac{\sigma_1 - \sigma_2}{2} \right| \quad (2.45)$$

The bearing dimensions were deemed acceptable if a yield stress safety factor greater than three was achieved compared with the total equivalent stress as determined using the Von Mises failure criterion:

$$\sigma' = \sqrt{0.5((\sigma_1 - \sigma_2)^2 + (\sigma_2 - \sigma_3)^2 + (\sigma_3 - \sigma_1)^2 + 6(\tau_1 + \tau_2 + \tau_3))} \quad (2.46)$$

The resultant stresses in the wrist pin bearing in spool one, based on a peak calculated force of 110.6 N are shown in Figure 2.22. A 125 MPa yield stress provides a safety factor greater than four.

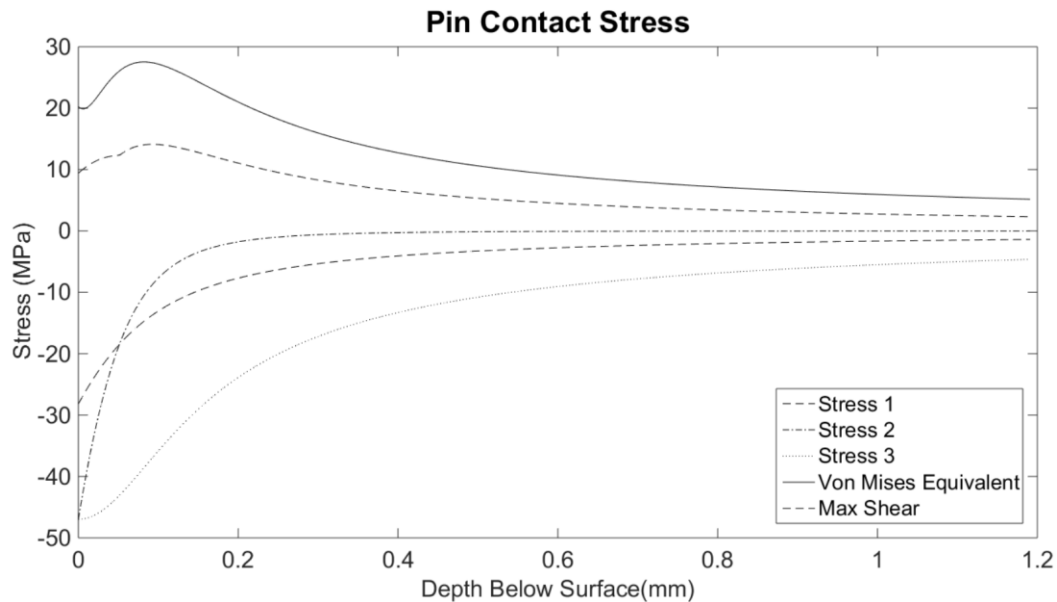


Figure 2.22. Contact stress in wrist pin

This section presented the results for designing and optimizing a high-speed valve suitable for use with switch-mode hydraulics. Section 2.4 provides a conclusion and discussion of this chapter.

2.4. Conclusion

The high-speed valve presented in this chapter enables experimental studies of switch-mode hydraulic circuits at the frequencies required to achieve fast response, good control bandwidth, and reasonable inertance tube lengths for switched inertance converter circuits. The valve design consists of a spool valve architecture equivalent to a 3-way 3-position valve supplying a 5-way 3-position valve. The two spools are actuated by a 4-bar crank-slider mechanism driven by a common crank-shaft. A modulated duty cycle is achieved through phase shifting one crank arm relative to the other. The crank-slider drive mechanism provides the benefit of peak velocity during transition, minimizing throttling losses. Furthermore, the use of a flywheel in conjunction with the crank-shaft allows for storage of the kinetic energy during spool deceleration and the release of the energy during acceleration, improving actuation efficiency. The mechanical coupling to the valve makes the open area of the valve known at all times by measuring the crank angle, allowing easy comparison to numerical simulations.

The valve was optimized for a rated pressure of 34.5 MPa and volumetric flow rate of 22.8 lpm. The resulting valve is capable of transitioning to the on-state in 5% of the switching period, where the on state is defined as a pressure drop of 0.345 MPa or less at the rated flow. The optimization process minimized the combined leakage and viscous friction losses on the sliding spool over a crank rotation, yielding a 1.7% energy loss relative to the flow energy over a cycle in the highest loss operating scenario. This optimization resulted in a crank radius of 11.43 mm, a spool diameter of 9.23 mm, and a radial clearance seal of 10 μm . The orifice ports in the sleeve were optimized towards an orifice diameter of 2.79 mm with each row consisting of eight orifices.

Additional considerations in the design were the secondary losses which consisted of all non-orifice losses. A tradeoff analysis between the compressibility, dependent on the dead volume, and the secondary losses, dependent on the flow path area resulted in a valve volume of 9.93 cc and a secondary pressure drop of 0.74% of the rated pressure.

The two spool design which transitioned at π and 2π radians, allowed two cycles per revolution. There is the potential of increasing the number of cycles per revolution by developing a valve of similar architecture which additionally transitions at $\pi/4$, $3\pi/4$, $5\pi/4$ and $7\pi/4$ radians. This would allow for four valve cycles per crank-shaft revolution at the expense of lower axial transition velocity.

Subsequent chapters will compare the modeled results with experimental results as well as demonstrate the use of this valve design in a switch-mode boost converter circuit.

3. Valve Experimental Validation

3.1. Introduction

Chapter 2 presented a crank-slider high-speed valve model and the resulting detailed design. In this chapter, experimental results for the fabricated valve are presented and model validation is discussed.

Three experimental tests were completed. The first was a low speed quasi-static test to identify the valve effective area as a function of crank-shaft position, valve overlap, transition time, and cycle length. A second quasi-static test was completed in an alternative hydraulic configuration to allow for valve leakage measurements. The final test was a no flow transient test to measure required input torque.

The experimental setup, procedures, and resulting data are provided in section 3.2. The results are presented in section 3.3, followed by discussion and conclusion in section 3.4.

3.2. Methods

3.2.1. Valve Profile Quasi-static Test

The objective of the quasi-static profile test was to determine the fabricated valve area profile as a function of crank-shaft position. The profile consisted of the effective area, valve overlap, transition time, and a comparison of the length of the two switching cycles that occur over one crank-shaft revolution. The valve behavior was approximated as a single orifice by combining the non-dimensional discharge coefficient and effective area into an effective C_dA value. The system information required to determine these parameters is provided by the following dependencies. The experimental C_dA can be determined through rearrangement of the orifice equation along with the experimental measurements of: valve inlet pressure p_{inlet} , valve outlet pressure p_{outlet} , and outlet flow rate Q_{outlet} :

$$C_d A = Q_{outlet} * \left(\frac{2(p_{inlet} - p_{outlet})}{\rho} \right)^{-0.5} \quad (3.1)$$

The hydraulic fluid utilized for the experiments was Mobile DTE 25 with a manufacturer provided density of 874 kg/m³.

The experimental hydraulic schematic is presented in Figure 3.1. A photograph of the experimental setup with labels corresponding to the hydraulic schematic is presented in Figure 3.2. The equipment utilized as labeled in Figure 3.1 is listed in Table 3.1.

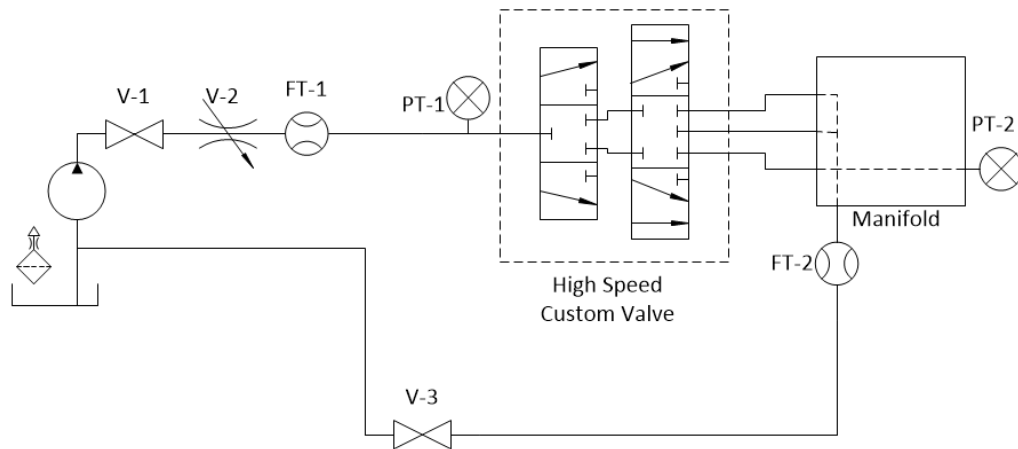


Figure 3.1. Valve validation hydraulic experimental setup

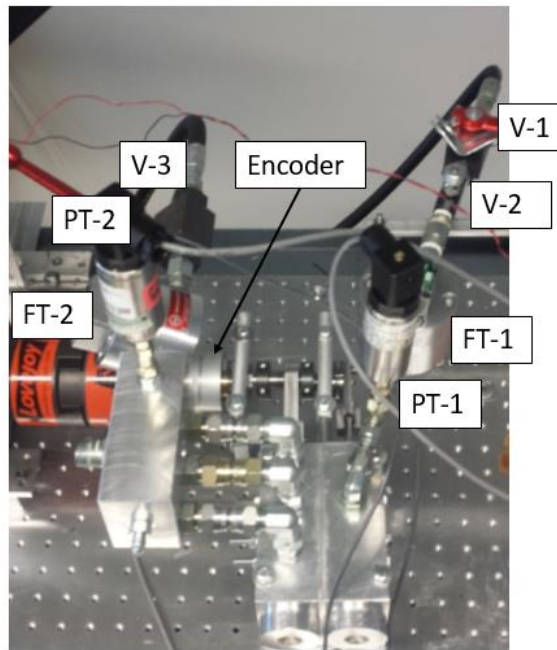


Figure 3.2. Experimental setup

Table 3.1. Quasi-static experimental equipment list

Drawing Reference	Description	Manufacturer	Model	Parameters
	Hydraulic Power Unit	Newton Manufacturing CO	99-498, Ser. NH-05928 0403	10HP/5GPM/3000PSI
V-1	Source Shutoff Valve	Hydae	KHB-16SAE-1114	
V-2	Throttle Valve	Parker	N400S	
FT-1	Source Flow Meter	AW Lake (Gear)	JVA-30KG-50-NPT	0.03-7.0 GPM. DH-B Sensor, 1689.2 Pulses/Liter
PT-1	Inlet Pressure Transmitter	Honeywell	440 060-F441-01, Ser. 1151652	500PSI, 9-32VDC, 4-20mA Output

High-speed Custom Valve	Crank-slider Spool Valve	Custom		
PT-2	Outlet Pressure Transmitter	Honeywell	440 060-F440-05, Ser. 1223574	200PSI, 9-32VDC, 4-20mA Output
FT-2	Source Flow Meter	AW Lake (Gear)	JVA-30KG-50-NPT	0.03-7.0 GPM. DH-B Sensor, 1687.8Pulses/Liter
V-3	Source Shutoff Valve	Hydae	KHB-16SAE-1114	
Not Shown	DC Gearmotor	Barber-Colman	EYQC-33900-2	24VDC, Geared to 2RPM
Not Shown	Gear Reducer	Boston	721-10-6	10:1
Not Shown	Rotary Optical Encoder	US Digital	HB6M	2 x 1024 Pulses/Revolution
Not Shown	Circuit Power Supply	Dr. Meter	HY300 3D-3	
Not Shown	Data Acquisition	National Instruments	NI PCIe-6343	32 AI Channels (500kS/s Total) 4 Counter Channels

The data acquisition card received inputs from 2 analog pressure transmitters, 2 digital flow meters, and a digital rotary encoder. A diagram of the electrical circuit is shown in Figure 3.3.

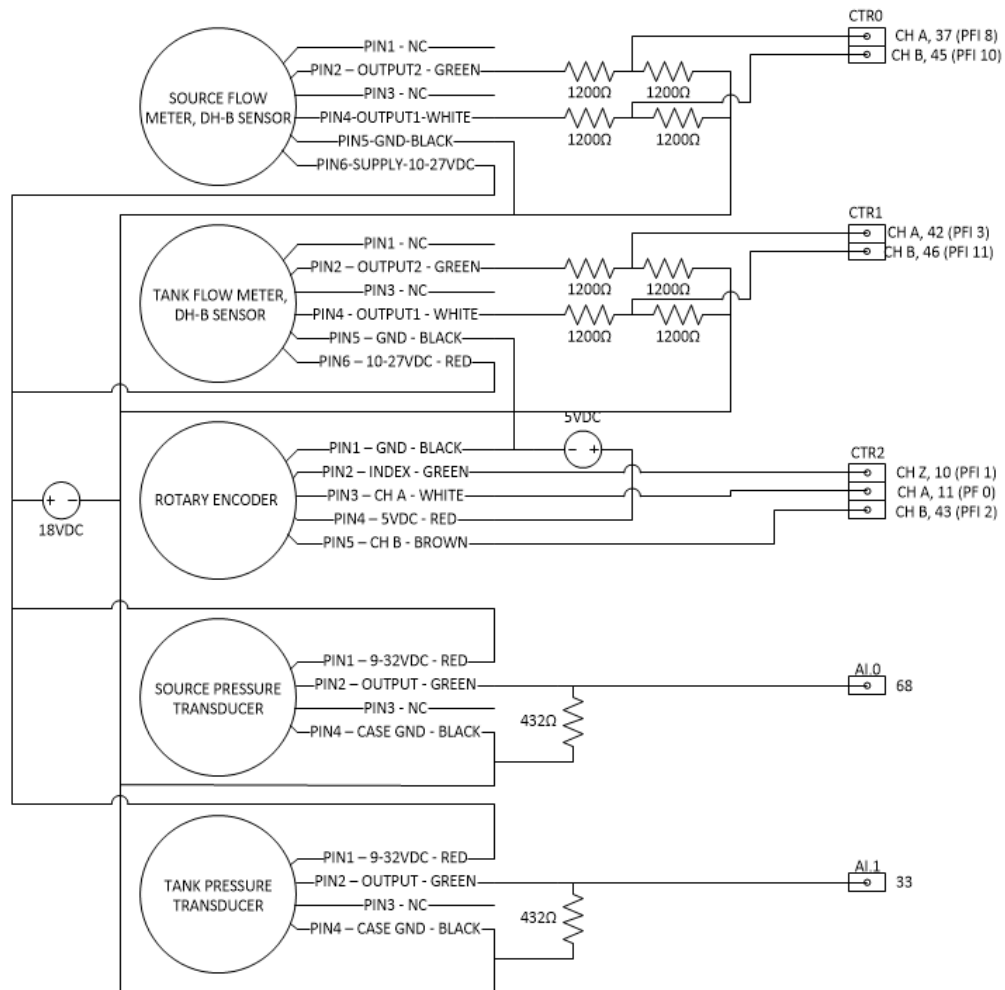


Figure 3.3. Quasi-static electrical circuit diagram

The AW Lake gear flow meters provided 1690 digital pulses for every liter of fluid volume that passed through the system. To provide a minimum of 50 pulses at each position of the rotary encoder on the valve crank-shaft (the encoder was sampled in quadrature 4×1024) at the rated flow (22.7 lpm), the maximum rotational velocity was 0.0196 rad/s. Using a gearmotor and a 10:1 gear reducer, the experimental crank-shaft rotational velocity was 0.0157 rad/s.

To determine the experimental C_dA , the primary and secondary losses are lumped into one parameter that contains linear and non-linear loss components, creating a flow dependency. The tests were completed at nine flow rates, accomplished through adjustment of the upstream throttling valve. To obtain data for all valve flow paths in one crank-shaft revolution, the duty cycle was set to 0.5. A summary of the experimental set points is shown in Table 3.2.

Table 3.2. Quasi-static C_dA Test Operating Points

<u>Parameter</u>	<u>Operating Point</u>
Crank-shaft Angular Velocity	0.0157 (rad/s)
Supply Pressure (Runs 1-8)	2.5 (MPa)
Supply Pressure (Run 9)	3.5 (MPa)

The procedure to complete the quasi-static valve profile test was as follows:

1. Configure the spools to a duty cycle of 0.5 with spool one located at the zero position
2. Close shutoff valves V-1, V-3
3. Turn on HPU unit and adjust pressure set point to 2.5 MPa (3.5 MPa for final test)
4. Open shutoff valves V-3 then V-1
5. Position the throttling valve to achieve evenly distributed flow from 1-18 lpm and allow 30 seconds to reach steady state
6. Energize the DC motor and begin sampling P-1, P-2, FT-1, FT-2, and the rotary encoder at a rate of 100 kHz
7. When the crank-shaft has made a full revolution (approximately 6 minutes) stop the DC motor and complete data sampling
8. Close shutoff valve V-1 and follow HPU shutdown procedures
9. Repeat steps 2-8 for all nine throttling valve positions

Setting the duty cycle consisted of using the model to determine the required phase shift, calculating the corresponding connecting rod angle, and using a digital angle indicator to identify the correct position. Selection of a 0.5 duty cycle provided the fully open flow paths in the order A1-A2-B3-B2, as designated in Figure 3.4.

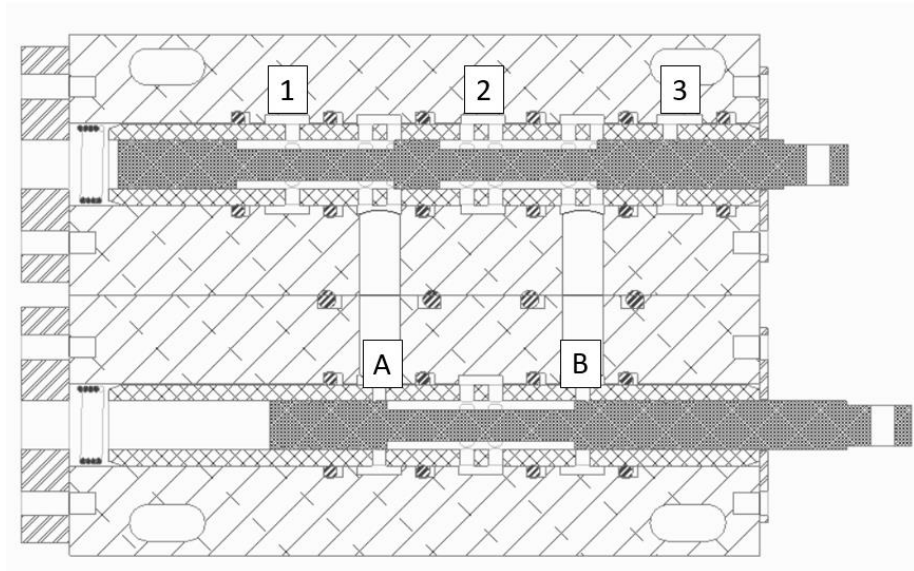


Figure 3.4. Flow path identification for quasi-static experimental test

A comparison of the analytical and experimental results required analytical pressure drop calculations of both primary and secondary losses discussed in section 2.2, as well as the losses between the valve block and the pressure transmitters (fitting losses). The additional fitting losses external to the valve are displayed in Figure 3.5.

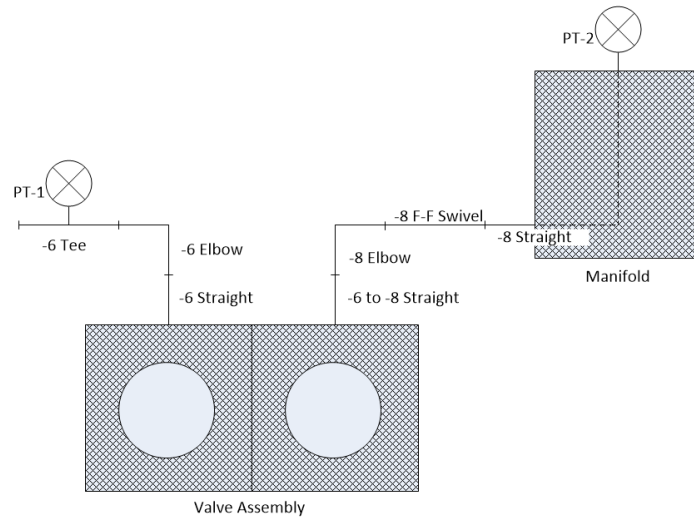


Figure 3.5. Experimental external fitting losses

The flow through the fittings was assumed to be fully developed laminar flow and the pressure drop is determined from empirical loss coefficients:

$$\Delta P_{fit} = K_L \frac{v^2 \rho}{2} \quad (3.2)$$

The straight -08 fittings were treated as laminar pipe flow. To account for the sudden expansion/contraction, the valve inlet, outlet, and manifold inlet fittings were treated as an orifice. A summary of the fitting losses along with assumptions is listed in Table 3.3.

Table 3.3. External pressure losses from experimental setup

<u>Type</u>	<u>Quantity</u>	<u>Size</u>	<u>K_L</u>
Tee Line	0.5	-6	0.9
Elbow	1	-6	1.5
Straight	50.8 (mm)	-6	Laminar Pipe Flow
Valve Entry	1	-6	Orifice Flow (C _d =0.6)
Valve Exit	1	-6	Orifice Flow (C _d =0.6)
Elbow	1	-8	1.5

Straight	127 (mm)	-8	Laminar Pipe Flow
Manifold Entry	1	-8	Orifice Flow ($C_d=0.6$)

Calculating all pressure losses at the experimental flow rates and correlating the values to a single orifice, provided an analytical comparison, which is discussed in section 3.3.

The test presented in this section allowed experimental determination of valve profile as a function of crank-shaft angular position. From this information a quantitative comparison of experimental and analytical values for valve transition, overlap, and cycle length was completed and is presented in section 3.3. A quasi-static leakage test and a transient test were additionally completed and the procedures are presented in the subsequent methods sections.

3.2.2. Quasi-static Leakage & Torque Transient Test

To further validate the valve model presented in section 2.2, a quasi-static test was completed to determine the experimental valve leakage and a transient test was completed to determine the required input torque. This section provides a brief overview of the hydraulic setup, the test set points, and the experimental procedures.

Leakage consists of flow from the high pressure points, supply and load, to the low pressure points, ambient and tank. As shown in Figure 2.18 leakage is typically negligible until the valve is in transition at which point leakage paths to tank are at minimum length. To experimentally measure these values with a gear flow meter, it is important to configure the valve for maximum leakage. This occurs at a duty of 1 where the load pressure is held at the supply pressure to allow backflow into the valve. The hydraulic schematic for this test is presented in Figure 3.6.

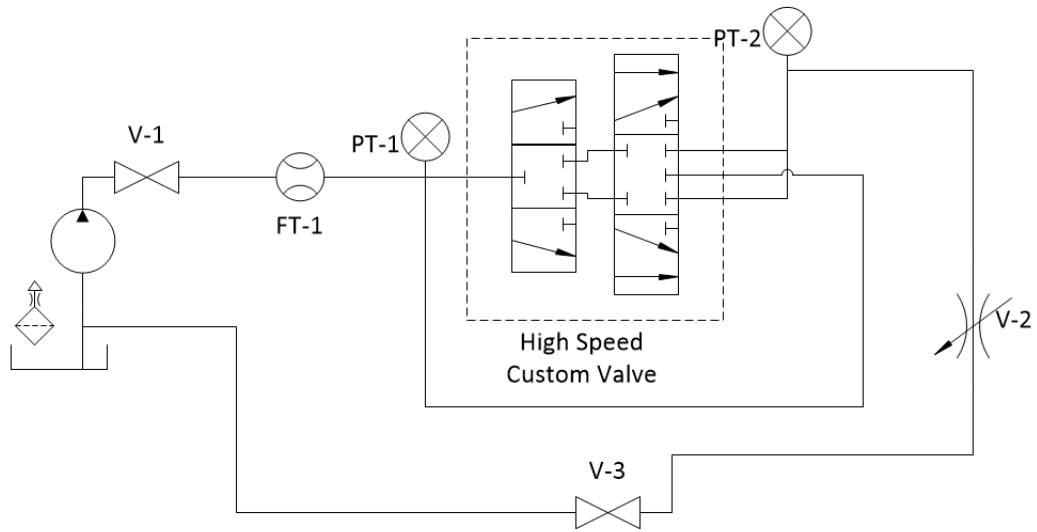


Figure 3.6. Leakage hydraulic experimental setup

The equipment utilized in this experiment is the same as presented in Table 3.1, with the addition of the pressure transmitters and torque transducer listed in Table 3.4. The optical rotary encoder was replaced with a torque transducer with a built in encoder.

Table 3.4. Leakage test pressure transmitters

Drawing Reference	Description	Manufacturer	Model	Parameters
PT-1	Supply Pressure Transmitter	Honeywell	440	Range: 5000psi Output: 4-20mA
PT-2	Tank Pressure Transmitter	Sensotec	440/F442-03	Range: 5000psi Output: 4-20mA
	Torque Transducer	Futek	TRS605, S/N 456903	5Nm, Encoder 2x360 PPR

The sensor circuits were equivalent to the sensor circuits used in test 1, shown in Figure 3.3, with the exception of the torque transducer as shown in Figure 3.7.

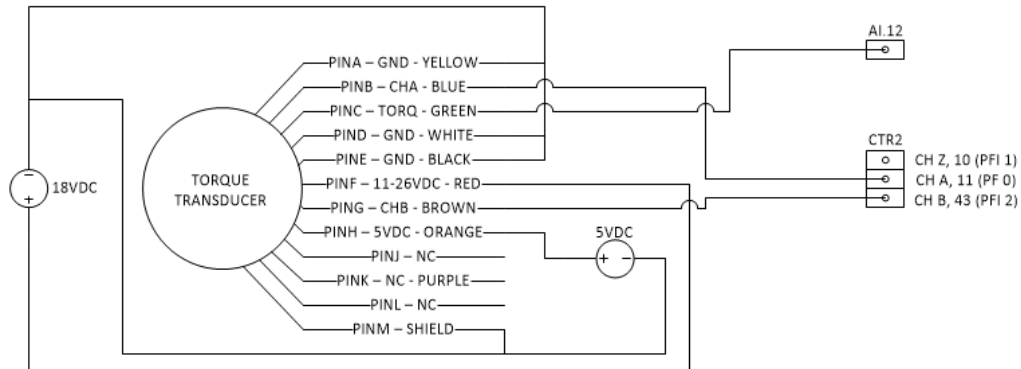


Figure 3.7. Torque transducer electrical circuit

For this test the 10:1 input speed reducer was rotated by hand. The procedures to complete the leakage test were as follows:

1. Configure the spools to a duty cycle of 1 with spool one located near the zero position
2. Close shutoff valves V-1, V-3
3. Turn on HPU unit and adjust pressure set point to 20.7 MPa
4. Open shutoff valves V-3 then V-1
5. Begin sampling P-1, P-2, FT-1, and the rotary encoder (Quadrature) at a rate of 10 kHz while slowly (<0.32 rad/s) turning the input of the 10:1 speed reducer
6. When the crank-shaft has made a full revolution complete data sampling
7. Close shutoff valve V-1 and follow HPU shutdown procedures

The pressure set point was selected based on the hose pressure ratings used in the hydraulic set up and resulted in a mean supply pressure of 19.4 MPa. The experimental values that were sampled at the same encoder position were averaged. The leakage is calculated analytically as described in section 2.2.3 and the results are presented in section 3.3.

Following the leakage experimental test, with the system in a zero-pressure oil-filled state, a torque transient test was completed. The hydraulic system remained in the same configuration but the 10:1 speed reducer was replaced by an electrical motor powered by a variable frequency drive as listed in Table 3.5.

Table 3.5. Electrical drive motor

Description	Manufacturer	Model	Parameters
Electrical Drive Motor	Electrim	38CF-3-1-36	3450RPM, 1.0HP
Variable Drive	WEG	CFW 08	3-300Hz

The procedures utilized to complete the torque transient test were as follows:

1. Start the HPU and set pressure to 3.5 MPa
2. Verify valves V-1, V-2, and V-3 are in the open state
3. Allow flow into the system for 10 s and shutdown the HPU, this is to ensure a fully lubricated system
4. Set the variable frequency drive to 5 Hz and initiate the drive. This corresponds to a rotational frequency of approximately 30.1 rad/s
5. Sample the torque transducer (and built in rotary encoder) at 10 kHz for 5 s
6. Stop the electrical drive motor
7. Repeat steps 1-6 at a variable drive setting of 30 Hz (approximately 180.6 rad/s)

The rotational velocity of the torque transient test did not exceed 180.6 rad/s due to concerns over damaging the torque transducers as the crank-shaft due to high vibrational resonant frequencies. The data acquired along with an analytical comparison is presented in section 3.3.

This section presented a brief overview of the experimental setup and procedures completed in a quasi-static leakage and torque transient test. All results along with analytical comparison is provided and discussed in section 3.3.

3.3. Results

Experimental results were acquired for the three experiments presented in the previous sections. The data acquired along with analysis and an analytical comparison are presented in this section.

The quasi-static valve profile test provided a lumped C_dA parameter as a function of crank-shaft position at nine flow rate settings. The valve profile results for the maximum flow test, are shown in Figure 3.8. Data points that were sampled at the same rotary encoder position were averaged. The labeling at the plateaus indicates the fully open flow path. The labels at the

transition events indicate the port that is transitioning. TA indicates spool one is transitioning across port A. Port 2 consists of a double row of orifices which is demonstrated in the data as the additional increase in value during flow paths A2 and B2.

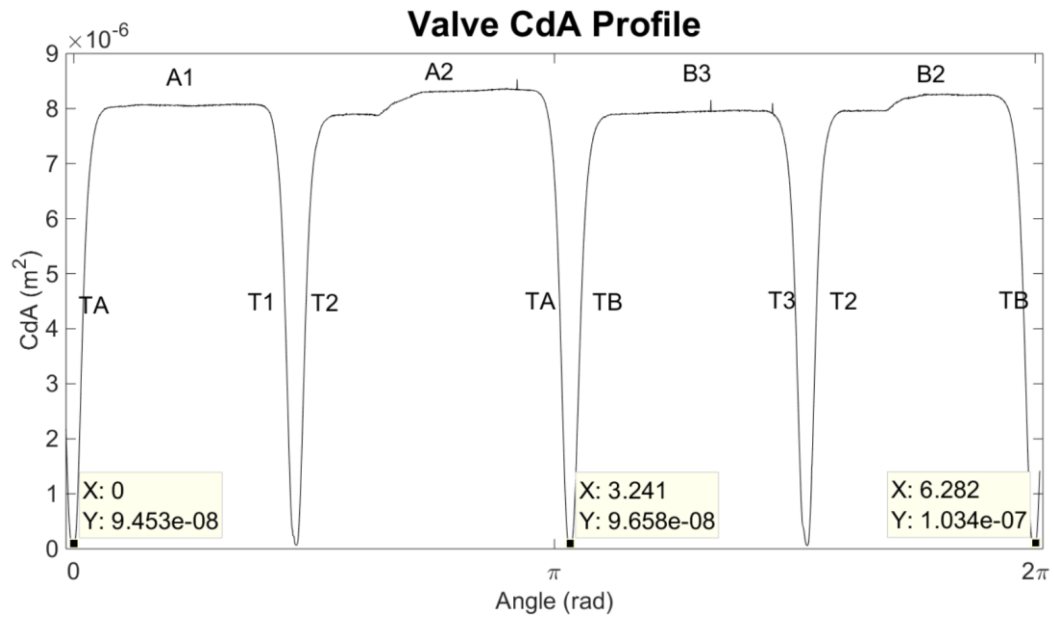


Figure 3.8. Run nine CdA profile

Each full crank-shaft revolution was designed to complete two symmetrical valve switching cycles. The experimental test demonstrated the two switching cycles (A1-A2 & B3-B2) but an asymmetry existed. Comparison of the cycle lengths, as shown in Figure 3.8, resulted in a first cycle length 6.6% greater than the second cycle length. During assembly, binding at the pin joints forced the valve block to be positioned at a slight angle to the crank-shaft, shown in an exaggerated view in Figure 3.9.

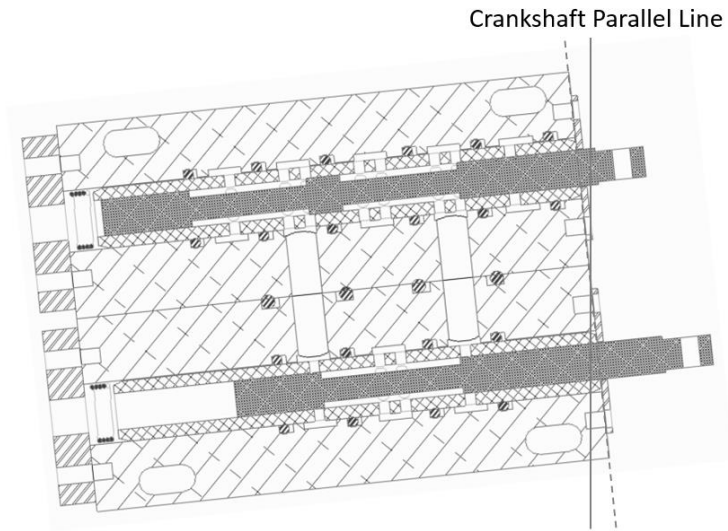


Figure 3.9. Valve block angular offset

This adjusted valve setup can be simulated in the model as a positive shift for spool 1 and a negative shift for spool 2 in the x-direction. Selection of a shift distance of 0.58 mm yielded an A2-B3 transition location that closely matches the experimental results, as displayed in Figure 3.10.

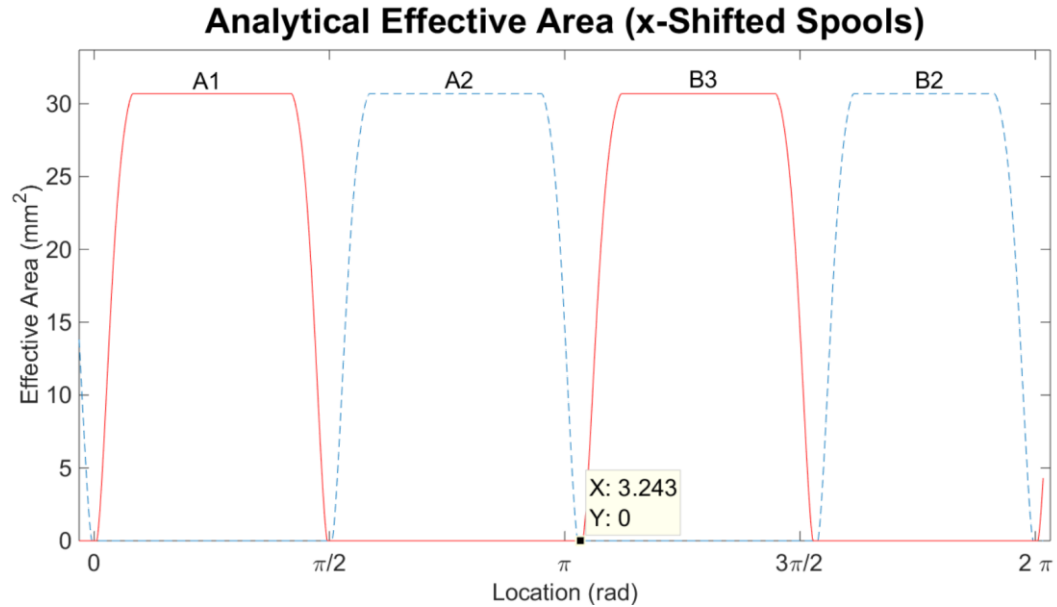


Figure 3.10. Analytical effective area with a positive shift for spool one and a negative shift of spool two of 0.58 mm

A closer view of the transitional period between flow paths A1 and A2 provides information on the transition time as well as the valve overlap. A comparison of the analytical and experimental fully open transition locations is shown in Figure 3.11. The analytical data was calculated based on transition across only the valve orifices and the experimental data includes the additional system losses (secondary, fitting). This caused the disparity in transition gradients and results in a higher analytical C_dA value, but does not affect the time to a fully open position. To present the analytical C_dA values, calculated only considering the orifice rows, and the experimental C_dA values, which included all system losses, on the same graph, the analytical data y-values were linearly contracted. Based on the values displayed there was a -2.7% percent difference in transition time between the experimental and analytical data.

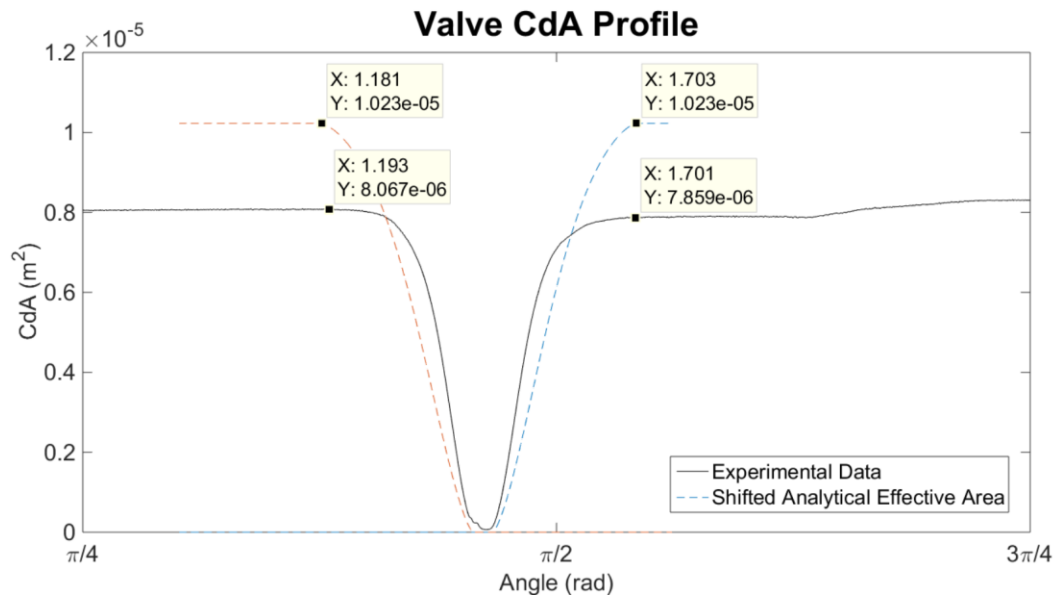


Figure 3.11. Analytical and experimental transition time comparison

To compare the design and experimental valve overlap, the data between flow paths A2 and B3 are presented in Figure 3.12. Based on the values displayed, there was a -13.3% percent difference between the experimental and analytical overlap. The effective area from the analytical model provided a clear transition from open to fully closed. The experimental data, however, was dependent on the flow through the valve, which, as a result of leakage, did not reach zero. The leakage also created challenges in identifying the transition point from partially open to fully closed.

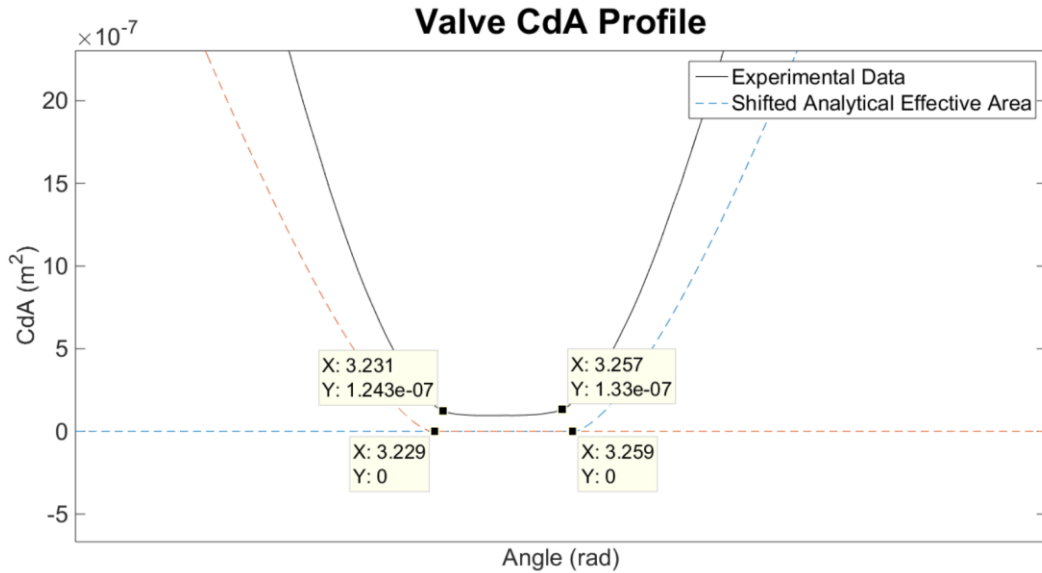


Figure 3.12. Valve analytical and experimental overlap comparison between flow paths A2 and B3

The valve profile results acquired for all nine of the flow rate settings are displayed in Figure 3.13. The general trend shows an increase in flow rate results in an increase in C_dA . For each individual test the fully open experimental flow rate and C_dA values, for the first flow path (A1), were averaged and resulted in the values presented in Table 3.6. The resultant analytical and experimental values as a function of flow rate are shown in Figure 3.14. The analytical values were determined as discussed in section 3.2.1.

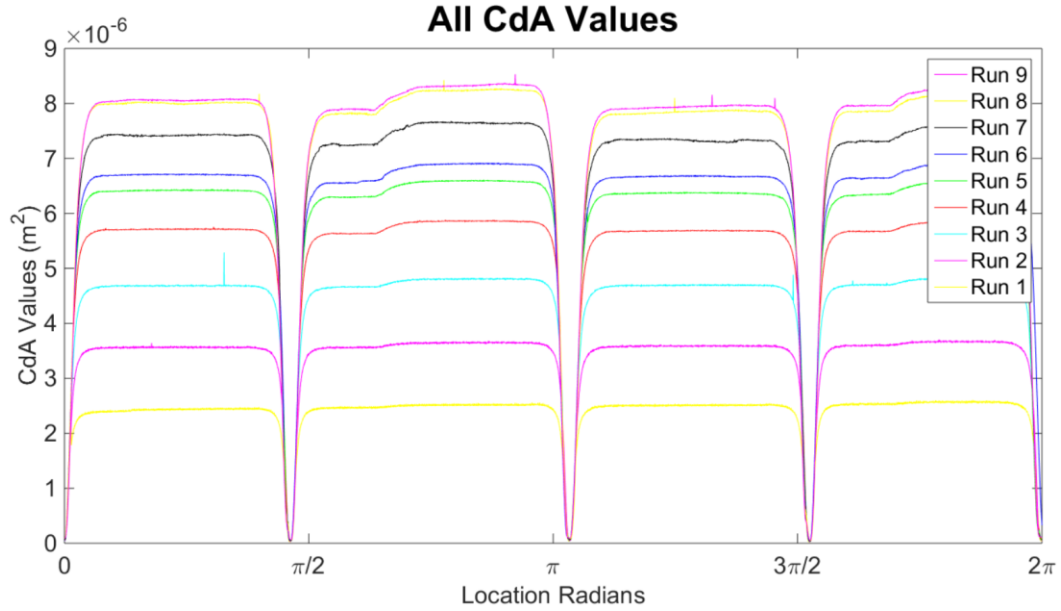


Figure 3.13. Experimental CdA values for nine flow rate trials

Table 3.6. Experimental average flow rate and C_dA through fully open flow path A1

<u>Run</u>	<u>Average Fully Open, A1,</u> <u>Flow rate (lpm)</u>	<u>Average Fully Open, A1,</u> <u>CdA (m²*10⁻⁶)</u>
1	1.17	2.43
2	2.01	3.56
3	3.32	4.69
4	4.93	5.71
5	6.37	6.42
6	7.56	6.70
7	11.74	7.42
8	15.24	8.01
9	17.49	8.06

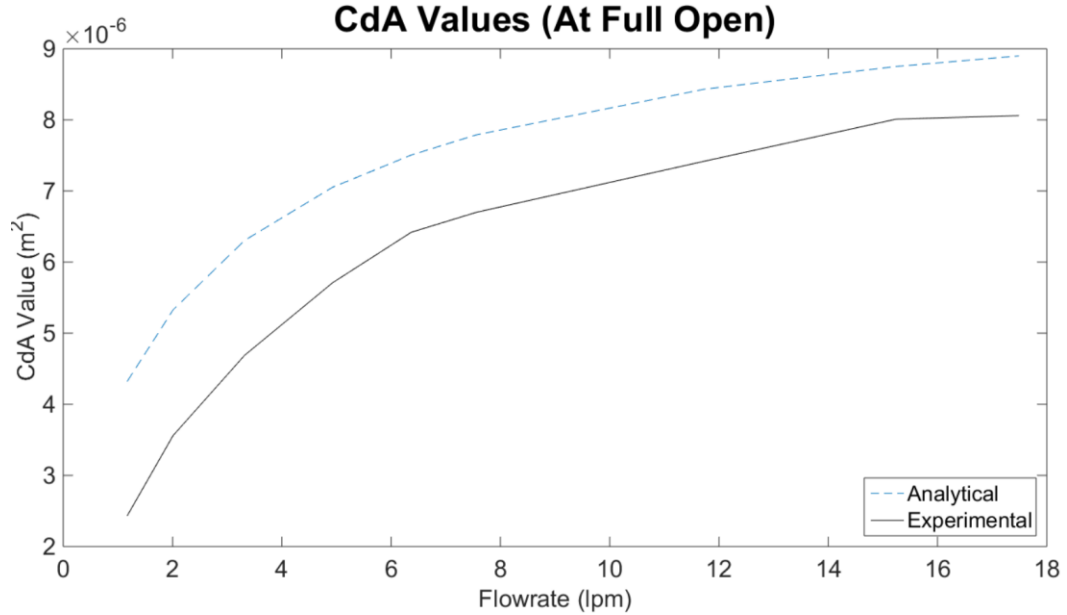


Figure 3.14. Comparison of analytical and experimental CdA at various flow rates

The analytical and experimental data demonstrated a similar trend with a consistently lower value for the experimental. This lower value indicates that the pressure loss through the valve was higher than calculated. A higher experimental pressure drop could be caused by a lower discharge coefficient, smaller circumferential flow gallery dimensions, or incorrect fitting loss assumptions. This data is sufficient to indicate that the primary and secondary valve losses are near expected values.

The objective of the second experiment was to determine the leakage flow rate as a function of the crank-shaft position. The experimental data along with the analytical comparison are presented in Figure 3.15. The data show a variation in the analytical and experimental peak leakage rates during transition, mainly at the π , transition. Additionally there is a clear non-symmetrical gradient for both experimental peaks. As mentioned previously, due to binding, the valve block had to be placed at an angle to the crank-shaft, which caused non-simultaneous transition between the two spools, resulting in shifted leakage occurrences. The variation in peak leakage rates is attributed to non-uniform clearances, based both on eccentricity of the spool

in the sleeve well as variation in sleeve cylindricity. In addition, instantaneous peak flow rates are difficult to capture utilizing gear flow meters due to the high inertia of the meter.

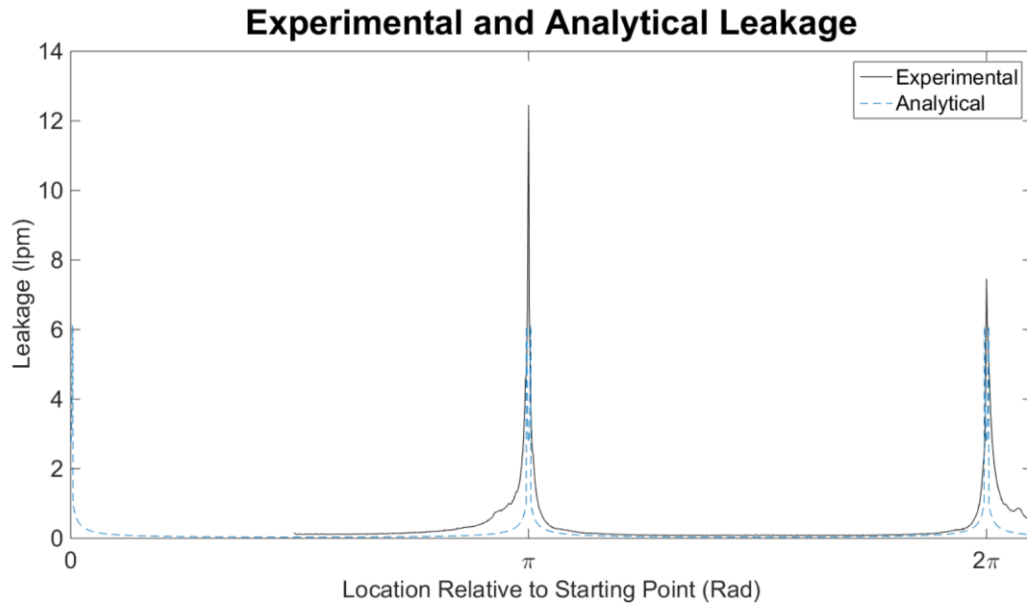


Figure 3.15. Experimental and analytical leakage comparison

The final experimental test, a torque transient test was completed at crank-shaft rotational speeds of 30.1 rad/s and 180.6 rad/s. The experimental data and analytical data, based on the model described in section 2.2.5, are presented in Figure 3.16. The first subplot displays the torque at 30.1 rad/s and the second subplot displays spool 1 and spool 2 location, as measured crank center to wrist pin. At low speed, the viscous and inertial forces rapidly decrease, resulting in a low input torque predicted by the analytical model. When the crank-shaft was rotated by hand, binding could be felt when the spools were approaching the maximum and minimum x locations, which corresponds to the linkage toggle positions. This is shown in the first subplot where the experimental torques are much higher than analytical. Tracking the unexpected torque peaks to the spool location, as shown by the dashed lines, correlates with these binding occurrences. Figure 3.17 presents the torque at 180.6 rad/s. At higher crank-shaft velocity the inertial and viscous forces become larger and the model better predicts the torques as shown in Figure 3.17. The effects of the binding forces are still demonstrated as a positive shift in the analytical torque

valleys. It is hypothesized that the model would better match at higher velocities where the magnitude of the viscous and inertial forces is much larger than the binding forces.

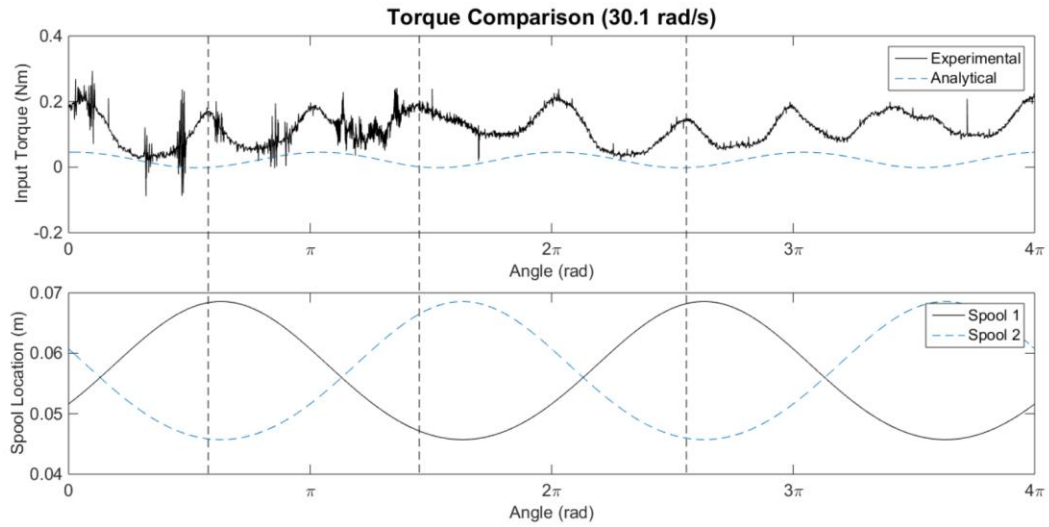


Figure 3.16. Analytical and experimental input torque comparison at 30.1 rad/s

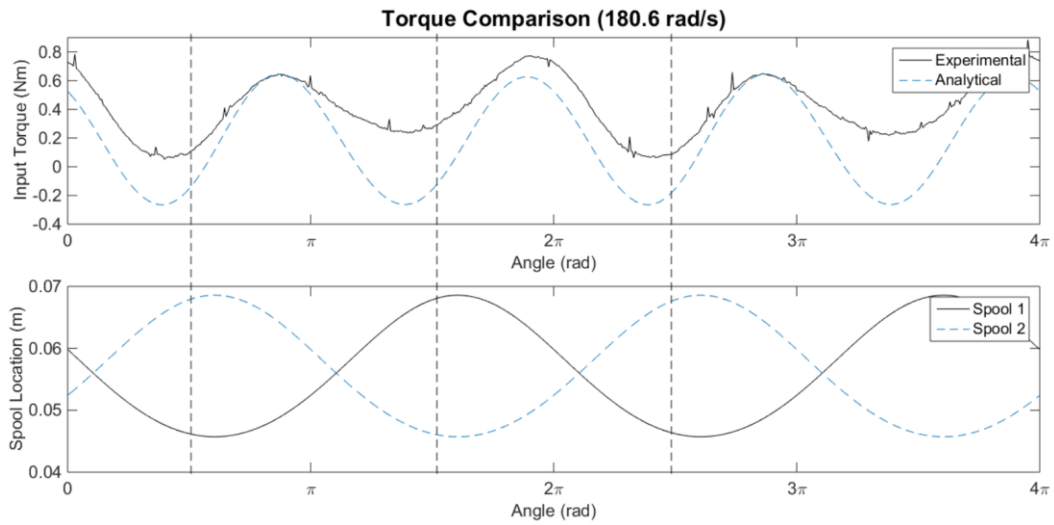


Figure 3.17. Analytical and experimental input torque comparison at 180.6 rad/s

The experimental results along with an analytical comparison for valve profile, leakage, and torque input were presented in this section. A discussion and overview are presented in the subsequent section.

3.4. Discussion & Conclusion

Three experimental tests and their respective results were presented in this section. The first consisted of a quasi-static valve profile test where the valve crank-shaft was slowly rotated, allowing flow to pass through the valve. All outlets were connected to a tank at atmospheric pressure and the measurement of the inlet pressure, outlet pressure, and tank flow rate allowed an effective lumped C_dA to be determined as a function of crank-shaft location. The objective of the second test was to compare the analytical and experimental leakage rates. The valve was configured for a duty of 1 and the supply and load were pressurized. As the crank-shaft was rotated the only flow path was leakage to ambient or leakage to tank. The final experimental test consisted of rotating the crank-shaft at two speeds, high and low, to determine the required input torque which is a function of viscous and inertial forces.

The quasi-static profile test demonstrated proper operation of two switching cycles over a single crank revolution. The cycles, however, were asymmetric, where the first cycle was 6.6% longer than the second cycle. This was explained by rotating the valve block during setup to prevent binding. The model demonstrated that a 0.58 mm shift in the x-direction matched the 6.6% variation. The predicted transition time was within 3% of the experimental results. The experimental valve overlap was 13.3% less than the analytical which only constituted a 0.13% difference when compared to cycle length. This was attributed to challenges in identifying the exact transition location due to non-zero leakage as well as spool tolerance variations. The lumped C_dA as a function of crank-shaft position was acquired at nine flow rates ranging from 1.17-17.49 lpm. The experimental results demonstrated agreement in the shape of the C_dA values predicted by the analytical model, but were consistently lower indicating a larger than expected pressure drop.

The leakage results demonstrated the occurrence of leakage peaks during transition and relatively low leakage during non-transition. The leakage peaks predicted by the analytical model were of

similar magnitude of the experimental results. The experimental leakage results had an asymmetrical gradient, which was demonstrated by the model when the x-location of spool 1 was shifted. The use of gear flow meters with incremental pulses provided challenges in acquiring instantaneous data that properly characterized the sharp gradients. A Coriolis meter was priced, but was cost prohibitive.

The low speed (30.1 rad/s) experimentally measured torque did not agree well with analytical predictions. Torque peaks occurred at the ends of the spool travel, which was attributed to binding that was observed during rotation of the crank-shaft by hand. At the higher speed (180.6 rad/s) test, the increased viscous and inertial forces provided results that better matched the model. The binding could be seen as a positive shift in the experimental data.

The fabricated valve profile matched the required constraints discussed in section 2.2.1, including the transition time, overlap, and overall shape required for use in a hydraulic switch-mode boost converter circuit. The subsequent section will provide the experimental procedures and results of the use of this valve in such a circuit.

4. Boost Circuit Experimental Validation

4.1. Introduction

Chapter 2 and 3 presented a high-speed hydraulic valve model and experimental validation of the resulting valve prototype. In this chapter, the use of the high-speed valve in a switch-mode boost converter circuit is discussed.

A boost converter is a hydraulic circuit that utilizes fluid inductance to develop an elevated pressure, compared to source. Figure 4.1 presents a simplified boost circuit hydraulic schematic. When the directional valve is open to tank, fluid is accelerated through the inductance tube converting energy in the pressure domain to the kinetic domain. When the valve is switched to the load branch, the fluid in the inductance tube decelerates, decreasing the kinetic energy while delivering flow to the boosted load pressure.

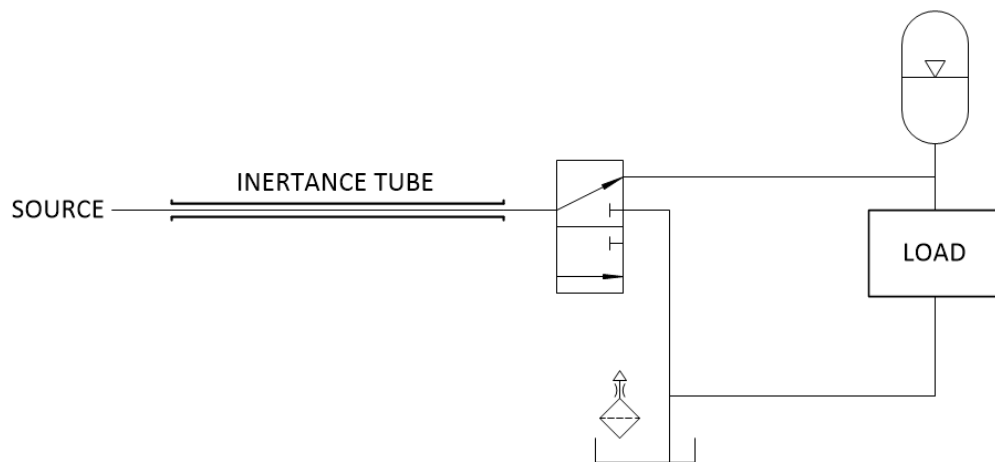


Figure 4.1. Simplified pressure boost converter

Boost converters offer the opportunity for varying pressures at point of use in multi-actuator systems supplied by a common pressure rail. This is useful in systems such as mobile hydraulics, where individual actuator pressure demand is variant and independent.

The boost converter experiment consisted of a single hydraulic test setup, tested at six different valve duty cycle settings. The valve was operated at optimal switching frequencies based on the duty cycle. The resultant data allowed calculation of the pressure boost ratio, system power (rail and load), and circuit efficiency. Additionally, the pressure wave propagation through the circuit were used to determine the fluid sonic velocity.

The experimental setup and procedures are provided in section 4.1. The results are presented in section 4.2, followed by discussion and conclusion in section 4.3.

4.1. Methods

The objective of the boost converter experimental test was to determine the hydraulic circuit behavior at various duty cycles. This was accomplished with the experimental system shown in Figure 4.2, which uses the high-speed crank-slider valve presented in chapters 2 and 3. Five locations were selected for pressure sampling, the rail, mid inertance tube, valve entry, load outlet, and tank outlet. The flow rate through all of the flow paths: rail, tank, and load, were measured with gear flow meters. In addition, the valve crank-shaft angular position was measured with a rotary encoder. Two photographs of the experimental setup are presented in Figure 4.3 and Figure 4.4. The equipment utilized as labeled in Figure 4.2 is listed in Table 4.1.

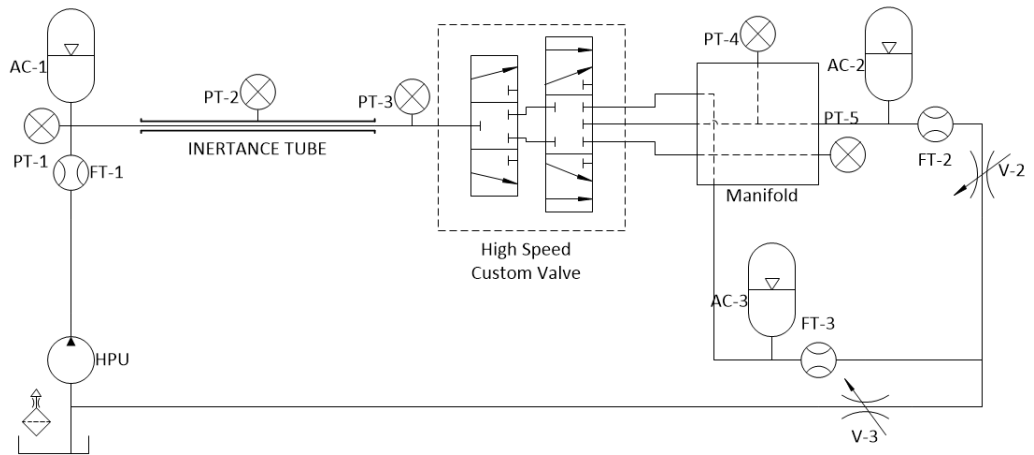


Figure 4.2. Experimental boost circuit hydraulic schematic

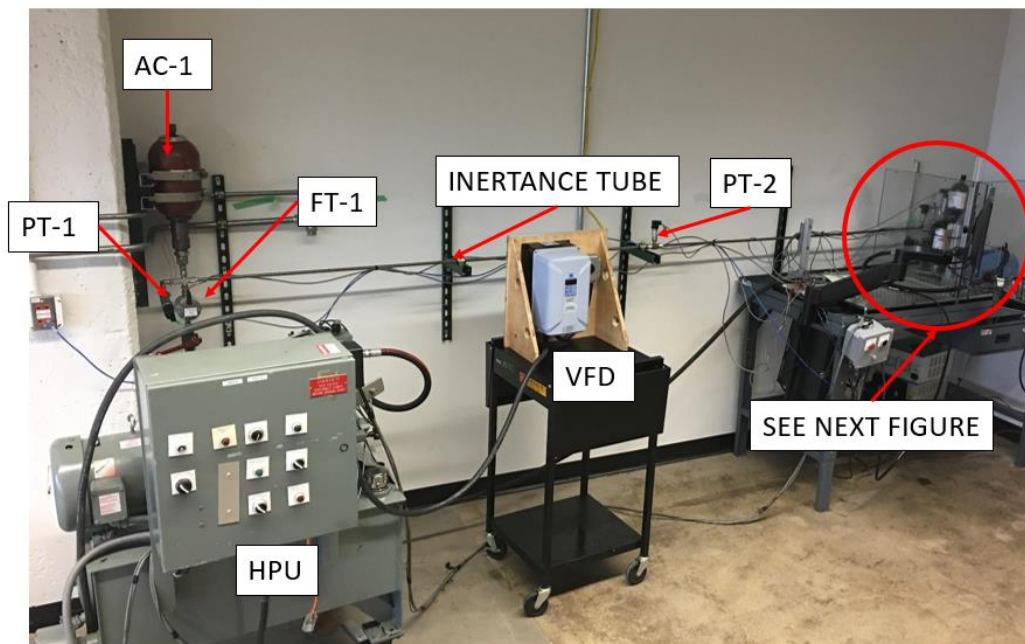


Figure 4.3. Experimental boost circuit setup (1)

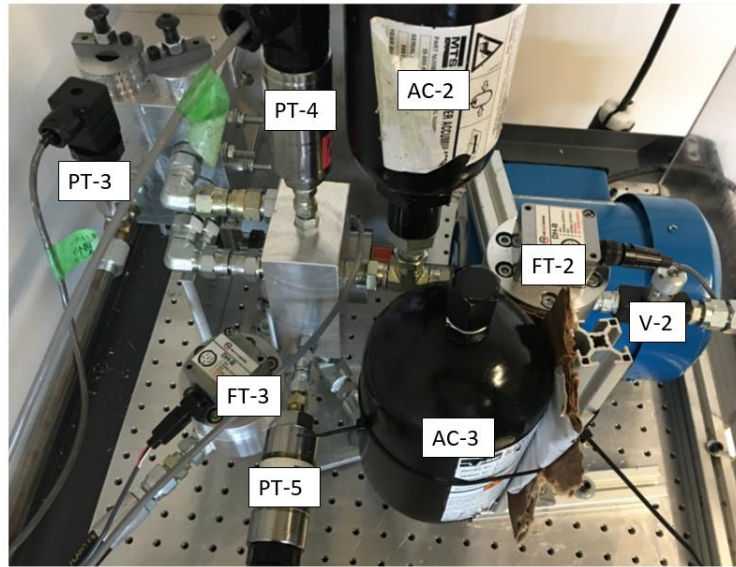


Figure 4.4. Experimental boost circuit setup (2)

Table 4.1. Boost circuit experimental equipment list

Drawing Reference	Description	Manufacturer	Model	Parameters
	Source Shutoff Valve	Hydae	KHB-16SAE-1114	
FT-1	Rail Flow Meter	AW Lake	JVA-30KG-50-NPT	0.03-7.0 GPM. DH-B Sensor
PT-1	Rail Pressure Transmitter	Sensotec	440/F442-03, Ser. 998861	5000PSI, 9-32VDC Output: 4-20mA
AC-1	Source Bladder Accumulator	Bosch	Bladder	Capacity: 4L Precharge: 8MPa
	Inertance Tube		Steel	1/2"OD, 1/4"ID, 3.68m
PT-2	Mid-Tube Pressure Transducer	Omega	PX4201-3KGX, #1	Range: 0-3000psi Output: 0-100mV
PT-3	Valve Entry Pressure Transducer	Omega	PX4201-3KGX, #2	Range: 0-3000psi Output: 0-100mV
High-speed Custom Valve	Crank-slider Spool Valve	Custom	N/A	Driven via 3450RPM AC motor

PT-4	Load Pressure Transmitter	Honeywell	060-F442-03, Ser. 1226395	5000PSI, 9-32VDC Output: 4-20mA
AC-2	Load Accumulator	MTS	BA001B3T01A1-MTSP	Capacity: 0.47L Precharge: 8MPa
FT-2	Load Flow Meter	AW Lake	JVA-20KG-25-NPT	0.01-2.0 GPM. DH-B Sensor
V-2	Load Valve	Parker	N400S	
PT-5	Tank Pressure Transmitter	Sensotec	440/F442-03, Ser. 837083	5000PSI, 9-32VDC Output: 4-20mA
AC-3	Tank Accumulator	Parker	BA002B3T01A1	Capacity: 1Qt Precharge: 3.5MPa
FT-3	Tank Flow Meter	AW Lake	JVA-30KG-50-NPT	0.03-7.0 GPM. DH-B Sensor
V-3	Tank Boost Valve	Parker	N400S	
	Return Shutoff Valve	Hydae	KHB-16SAE-1114	
HPU	Hydraulic Power Unit	Newton Manufacturing CO.	99-498 Ser. NH-05928 0403	10HP/5GPM/3000PSI
	Electrical Drive Motor	Electrim	38CF-3-1-36	3450RPM, 1.0HP
VFD	Variable Drive	WEG	CFW 08	3-300Hz
	Rotary Optical Encoder	US Digital	HB6M	2 x 1024 Pulses/Revolution
	Circuit Power Supply	Dr. Meter	HY300 3D-3	
	Data Acquisition	National Instruments	NI PCIe-6343	32 AI Channels (500kS/s Total) 4 Counter Channels

The inertance tube selected had an inner diameter of 6.35 mm (0.25”), wall thickness of 3.18 mm (0.125”), and length of 3.68 m. The length was selected as a reasonable experimental setup length that resulted in an optimal switching frequency <100 Hz, as discussed later in this section. The diameter was selected as a readily available tube size that provided reasonable pressure drop at the HPU maximum flow rate.

The data acquisition system, Figure 4.5, received inputs from five analog pressure transducers, three digital flow meters, and a digital rotary encoder. The rail, load, and tank pressure transducers outputted a 4-20 mA signal. A 432 Ω resistor was placed in series with these transducers to provide the DAQ with a voltage of 8.64 V at maximum output current. The DAQ range for these analog inputs was ± 10 V. The mid-tube and valve entry pressure transducers had a response time of 0.2 ms and a 100 mV ratiometric differential output. The DAQ range for these inputs was set to ± 1 V which applied a built in gain to the signal. Additionally, a three-point median filter was applied in software to remove single spikes caused by noise from the variable frequency drive (VFD). The flowmeters outputted digital counter pulses near the sensor supply voltage. A voltage divider was constructed to drop the flow meter digital output to the 5 V recommended for the DAQ counter channel input. The rotary encoder was powered by 5 V, which allowed the outputs to be directly sampled from a DAQ counter channel. Additionally the circuit supply voltage was acquired for reference. The pressure transducers were calibrated using a deadweight tester and measured supply voltage, as presented in Appendix A.3.

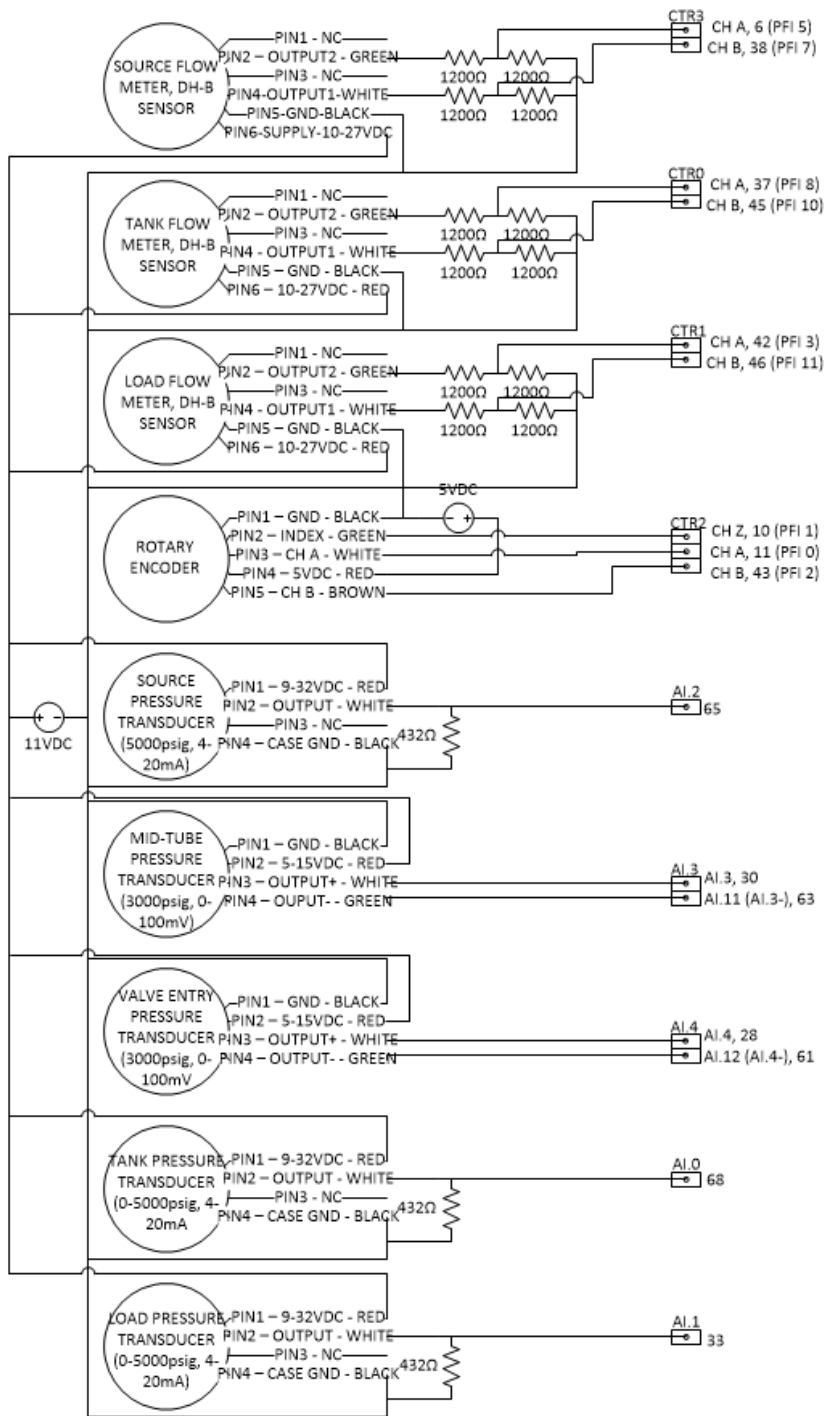


Figure 4.5. Boost circuit electrical circuit schematic

As discussed in chapter 1, from lumped parameter models developed by Johnston et al., the optimal switching frequency is dependent on the duty cycle, D , fluid sonic velocity, c , and inertance tube length, L [21]:

$$f = \frac{Dc}{2L} \quad 0 \leq D \leq 0.5; \quad f = \frac{(1-D)c}{2L} \quad D > 0.5 \quad (4.1)$$

The fluid used was Mobil DTE 25 with a manufacturer provided density of 874 kg/m^3 . A test previously conducted by a lab colleague, Hao Tian [29], measured the displacement of a piston into a cylinder with a known volume, resulting in a calculated bulk modulus of 1.40 GPa . The sonic velocity is expressed as:

$$c = \sqrt{\frac{\beta}{\rho}} \quad (4.2)$$

Six target duty cycle set points were selected for experimental testing and their respective optimal frequencies are listed in Table 4.2. A VFD was utilized to adjust the speed of the motor driving the valve crank-shaft. At a VFD setting of 60 Hz the motor achieves its rated RPM of 3450 . Based on two switching cycles per crank-shaft revolution, the switching frequency can be used to determine the VFD frequency set point based on Eq. (4.3), where f_s represents the switching frequency and f_{VFD} represents the VFD frequency set point. These values are also presented in Table 4.2.

$$f_{VFD} = \frac{3600}{3450} * \frac{f_s}{2} \quad (4.3)$$

Table 4.2. Experimental duty set points and resultant switching frequencies

<u>Duty Cycle</u>	<u>Switching Frequency (Hz)</u>	<u>VFD Frequency (Hz)</u>
0.2	33.2	17.33
0.3	49.8	26.00

0.4	66.4	34.66
0.5	83.0	43.33
0.7	49.8	26.00
0.9	16.6	8.67

Additional experimental set points selected were the load orifice area, tank pressure, and source pressure. As shown in the simplified boost converter schematic in Figure 4.1, the high-speed control valve switches the inertance tube between load and tank. In a real application this load could consist of a hydraulic actuator or motor, which in an experimental setting would add another level of complexity. For the experimental system, a simple needle valve was placed on the load side to apply flow resistance to simulate a load. To apply sufficient load resistance compared to the switching valve, the load valve C_dA set point was an order of magnitude smaller than the switching valve fully open C_dA . The selected value is presented in Table 4.3. Based on the high switching frequency and expected wave oscillations in the inertance tube, cavitation was a concern. To prevent cavitation in this set of tests, the tank side was boosted above atmospheric pressure through the use of a downstream needle valve. The source pressure was selected such that a pressure transient peak twice the source pressure did not exceed the rated pressure of the high-speed pressure transducers, 20.7 MPa (3000 psi). The pressure set points are listed in Table 4.3.

Table 4.3. Boost circuit experimental set points

<u>System Parameter</u>	<u>Target Set Point</u>
Load Orifice (C_dA)	$5 \cdot 10^{-7} \text{ (m}^2\text{)}$
Source Pressure	11 (MPa)
Boosted Tank Pressure	5 (MPa)

To set the load valve to the value listed in Table 4.3, a steady state test was completed with the switching valve in a static position. With the switching valve manually positioned open to load, the pressure measurements PT-4 and PT-5, along with the flow measurement from FT-2, were used in the orifice equation to determine the load valve C_dA . The procedure for setting the load valve was as follows:

Load Valve Setting – Adjusting the load valve to the desired orifice area

Valves V-1 and V-4 are ball valves used to isolate the system.

1. Turn the HPU on and set the pressure set point to 11 MPa
2. Turn the following valves to the fully open position: V-1, V-3, V-4
3. Manually rotate the High-speed Valve to flow path source to load
4. Turn valve V-2 until the flow as measured from FT-2 and the differential pressure as defined by the difference between PT-4 – PT-5 indicate an orifice area, based on the orifice equation of $5E-7 \text{ m}^2$ within 10%
5. Once the load valve has been set, tighten the set screw and shut down the system

The next requirement in completing the experimental tests was to set the high-speed valve duty cycle to the desired value. The required phase shift between crank arms to accomplish the duty cycle was determined using the model presented in section 2.2. Figure 4.6 presents a photograph of the adjustment method. With connecting rod two held in a known vertical position, a simple geometric relationship was used to determine the angle for connecting rod one to accomplish the phase shift. The crank arm for spool one was rotated independently of the spool two crank arm until the connecting rods were at the correct angular position as measured by the digital angle indicator.

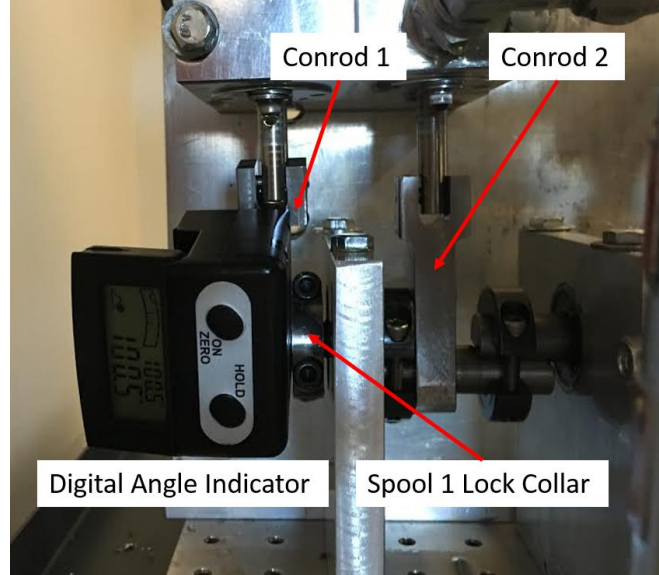


Figure 4.6. Duty cycle adjustment method

This method was rather rudimentary and required iterative adjustments based on an experimentally determined duty profile. Additionally, as discussed in section 3.3 there was a slight difference in the duty cycle between the two switching cycles per valve revolution. To experimentally determine the actual duty cycles, a slow speed 18.1 rad/s profile test was completed. The experimental duty cycle was determined as the angular duration that the valve was closed to tank, $\theta_{tankclosed}$, over the designed cycle duration as shown in Eq. (4.4). A higher duty cycle indicates more open time to load.

$$D_{exp} = \frac{\theta_{tankclosed}}{\pi} \quad (4.4)$$

The experimental procedures followed to acquire the duty cycle profile, were completed for each duty cycle adjustment and are as follows:

Duty Profile – Verifying the duty cycle set point

1. Manually adjust the high-speed valve in a non-operational state to 0.2D
2. Turn the following valves to the fully open position: V-1, V-4

3. Position needle valve V-3 to a 1 turn position and manually position the valve for flow to tank
4. Turn on the HPU and set the pressure set point to 7 ± 0.2 MPa as measured by PT-1
5. Activate the motor for the High-speed Valve with the VFD set at 3 Hz
6. Adjust needle valve V-3 until peak to peak oscillations in the source pressure are near 1 MPa
7. Acquire data from all sensors for 5s at a sampling frequency of 50 kHz
8. Shutdown HPU and follow proper system bleeding procedures
9. Repeat steps 1-8 for the duty set points presented in Table 4.2 prior to running the full experimental test

Once the load valve was set and the duty cycle was adjusted to the desired value based on the previous procedures, the transient switch-mode experimental tests were conducted at the switching frequencies listed in Table 4.2. The procedures completed for each of the six tests were as follows:

Boost Circuit Testing – Transient switch-mode tests

1. Turn the following valves to the fully open position: V-1, V-4
2. Position needle valve V-3 to a 1 turn position and manually position the valve for flow to tank
3. Turn on the HPU and set the pressure set point to 11 ± 0.2 MPa as measured by PT-1.
4. Activate the motor for the High-speed Valve with the VFD set at 5 Hz. Slowly accelerate the motor via VFD to a valve switching frequency of 33.2 Hz (Approximately 17.33 Hz on VFD)
5. In an iterative approach adjust needle valve V-3 and the HPU set point until an equilibrium source pressure and tank pressure of 11 ± 0.5 MPa and 5 ± 0.2 MPa respectively is achieved (as measured by PT-1 and PT-5)
6. Acquire data from all sensors for 1s at a sampling frequency of 50 kHz
7. Shutdown HPU and follow proper system bleeding procedures.
8. Repeat steps 1-8 for the duty set points and valve switching frequencies presented in Table 4.2

The measurements acquired from experimental tests provided information to calculate the system boost ratio, the rail power, the load power, overall system efficiency, and sonic velocity. To determine single-cycle behavior, a numerical integration of the instantaneous values was completed and averaged over each cycle. The cycle results were averaged over 16 cycles to determine the cyclic steady-state behavior. The boost ratio, *BR*, was defined as the ratio of the

load and rail pressures compared to tank. These pressures were measured as shown in Eq. (4.5), where the numbered subscript represents the pressure sensor as shown in Figure 4.2. To calculate the average boost ratio over a single cycle, Eq. (4.6) was used, where t_{cs} represents the cycle start time, and T_{ss} is the cycle period.

$$p_{raildiff} = p_1 - p_5 \quad p_{loaddiff} = p_4 - p_5 \quad (4.5)$$

$$BR_{1cycle} = \frac{\int_{t_{cs}}^{T_{ss}+t_{cs}} (p_{loaddiff}) dt}{\int_{t_{cs}}^{T_{ss}+t_{cs}} (p_{raildiff}) dt} \quad (4.6)$$

The average rail power over a single cycle, $\bar{P}_{rail,1cycle}$, is determined based on the rail flow rate, Q_{rail} , and rail differential pressure.

$$\bar{P}_{rail,1cycle} = \frac{\int_{t_{cs}}^{T_{ss}+t_{cs}} (p_{raildiff}) Q_{rail} dt}{T_{ss}} \quad (4.7)$$

The average load power over a single cycle, $\bar{P}_{load,1cycle}$, is determined based on the load flow rate, Q_{load} , and load differential pressure.

$$\bar{P}_{load,1cycle} = \frac{\int_{t_{cs}}^{T_{ss}+t_{cs}} (p_{loaddiff}) Q_{load} dt}{T_{ss}} \quad (4.8)$$

The steady state system efficiency over a single cycle, η_{1cycle} , is the ratio of steady state load power and rail power.

$$\eta_{1cycle} = \frac{\bar{P}_{load,1cycle}}{\bar{P}_{rail,1cycle}} \quad (4.9)$$

The sonic velocity was determined by plotting the inertance tube pressure transients, as measured by P-2 P-3, vs time. The pressure wave time of flight of specific events was measured at the two

sensors. From the time of flight and the distance between the transducers, 1.74m, the sonic velocity was calculated.

The experimental setup, equipment, and procedures for a boost converter circuit were presented in this section. All results acquired in the completion of the boost converter testing including boost ratio, rail power, load power, system efficiency, and sonic velocity for the six duty cycle set points are presented in the following section.

4.2. Results

The experimental setup and procedures to obtain data from a hydraulic boost converter circuit were presented in the previous section. This section presents the data acquired during the experimentation along with a brief analysis.

As discussed in the previous section the first test was a static test to properly set the load orifice. The load orifice area and discharge coefficient were determined from the measured pressure differential and flow rate through the orifice equation. The load orifice C_dA was initially set to a value of $5.27 \times 10^{-7} \text{ m}^2$ which was within 10% of the target set point of $5 \times 10^{-7} \text{ m}^2$. After the experimental runs were completed, the load orifice valve effective area had decreased due to backlash in the needle valve screw and vibration in the system. The resultant C_dA after all tests were completed was $3.64 \times 10^{-7} \text{ m}^2$. This variation is not of concern since the needle valve was being used to simulate a flow load and all load flow rates were acquired.

The second test was used to calculate the actual duty cycle. This was required for validation of a boost converter model developed by another member of the lab, as well as verifying that the duty cycle was set near the target value. With the valve crank-shaft rotating at a slow speed, the pressure measured by the valve entry pressure transducer, plotted in Figure 4.7, allowed identification of key events. The rotary encoder index was utilized as the zero position and does not represent the crank-shaft zero position. The figure displays multiple cycles overlaid based on rotary encoder position.

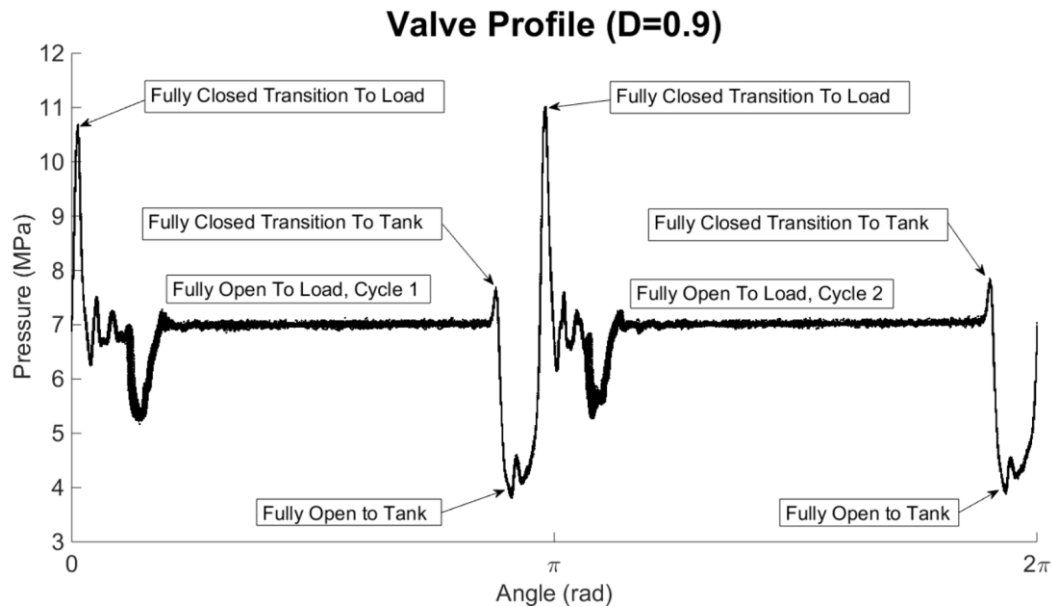


Figure 4.7. Experimental valve profile, D=0.9

The fully closed transition peaks represent when the valve is at the center of the closed position. The elevated pressure plateaus indicate when the valve is open to load with the first plateau representing the first cycle and the second plateau representing the second cycle. The experimental duty cycle was defined as the angle duration that the valve is closed to tank divided by π , as shown in Eq. (4.4). Measuring the distance between the fully closed transition peaks, as shown in Figure 4.8, allowed determination of the duty cycle. The transition peaks represent the center of the fully closed position so an additional closed time of 0.005π , 0.5% of cycle time, was added to the peak to peak distances. This was based on the fully closed designed period of 1% of the switching cycle. As discussed in the previous chapter, during assembly, the valve block had to be located at an angle to the crank-shaft to prevent binding, which resulted in a duty cycle asymmetry between the two cycles. All experimentally determined duty cycles are provided in Table 4.4.

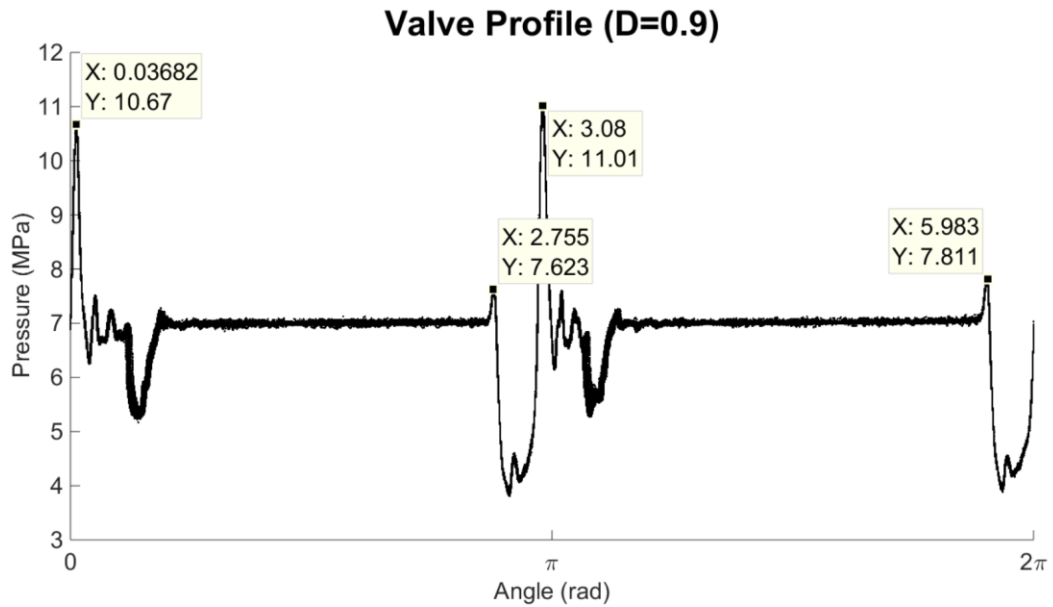


Figure 4.8. Experimental valve profile peak locations, D=0.9

Table 4.4. Experimental actual duty cycle results

<u>Duty Set Point</u>	<u>Cycle 1 Actual Duty</u>	<u>Cycle 2 Actual Duty</u>	<u>Average Actual Duty (+0.005π)</u>
0.2	0.150	0.205	0.183
0.3	0.236	0.289	0.268
0.4	0.365	0.420	0.397
0.5	0.463	0.515	0.494
0.7	0.666	0.719	0.697
0.9	0.865	0.922	0.899

Following the valve profile acquisition, the transient switch-mode tests were completed. The transient system pressures at a duty cycle of 0.5 are presented in Figure 4.9. Due to noise from operating the VFD, a three-point median filter was applied to the raw data. The plot represents

data acquired for 42 crank-shaft revolutions overlaid at the same rotary encoder position. The boost converter effect can be seen by the elevated load pressure compared to rail pressure. A plot of the inertance tube pressures is presented Figure 4.10. Several interesting events are labeled on the pressure plots and a brief discussion of each is completed following the figures.

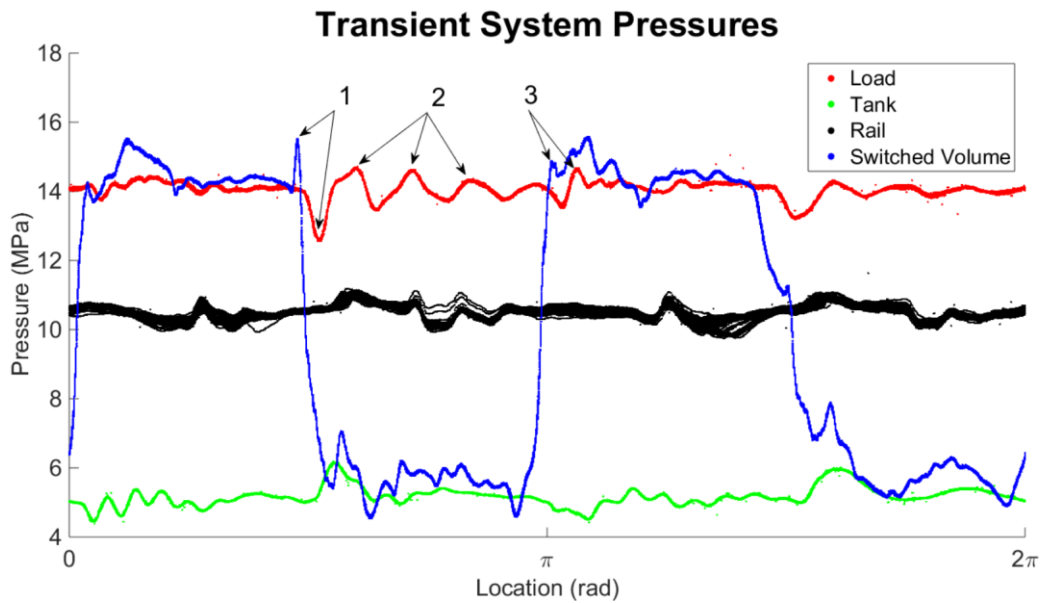


Figure 4.9. System experimental pressures, D=0.5

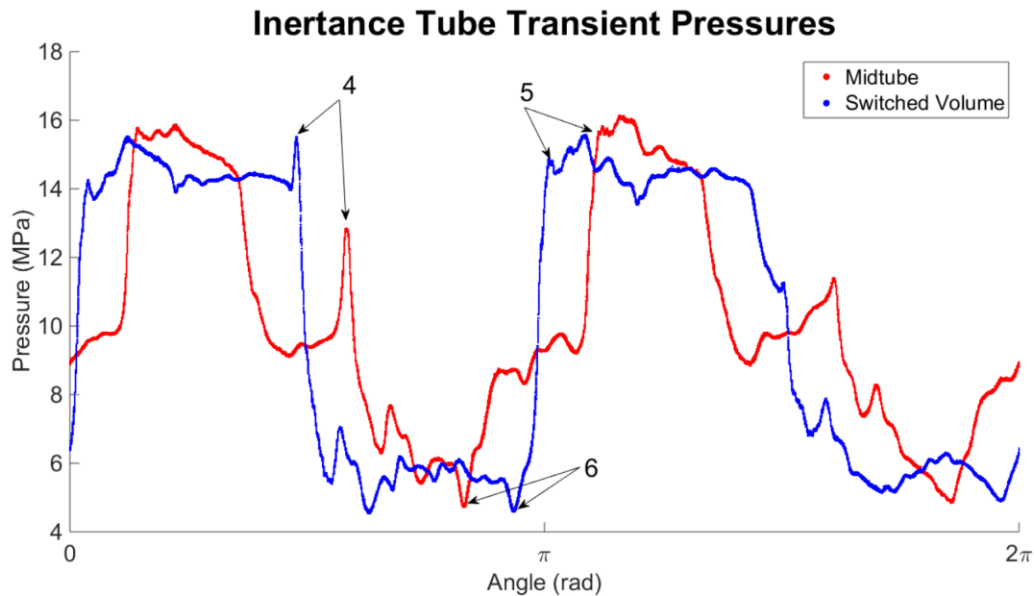


Figure 4.10. Inertance tube experimental pressures, $D=0.5$

Discussion of events labeled in Figure 4.9, Figure 4.10:

- In event 1, the valve has closed after being open to load, blocking the load flow, creating a spike in the switched volume pressure. The fluid on the load side has momentum away from the valve. When flow to load is blocked, the momentum creates a low pressure dip measured at the load pressure transducer. The switched volume pressure spike is reflected up the inertance tube, as observed by the delayed pressure spike seen at the mid-tube pressure transducer labeled 4.
- Event 2 indicates a decaying pressure wave resonance observed in the load line. This occurs when the valve is blocked to load.
- In event 3, the valve has closed after being open to tank, blocking the tank flow, creating a spike in the switched volume pressure. Once the valve completes the transition, the switched volume is exposed to the load side, as seen by the spike in load pressure. The elevated load pressure propagates up the inertance tube, as observed by the delayed pressure increase seen at the mid-tube transducer labeled 5.
- Event 6 is labeled to demonstrate pressure oscillations that dip below the tank pressure of 5 MPa, indicating that without a boosted tank pressure, cavitation would occur.

Similar pressure transients occurred at all six of the experiments. The boost ratio, as shown in Eq. (4.6), was calculated for each test based on the ratios of load differential pressure and rail differential pressure, as calculated in Eq. (4.5). Table 4.5 lists the boost ratio at each duty cycle, which is plotted in Figure 4.11.

Table 4.5. Experimental boost ratio results

<u>Duty</u>	<u>Avg. Rail Pressure (MPa)</u>	<u>Avg. Tank Pressure (MPa)</u>	<u>Avg. Load Pressure (MPa)</u>	<u>Boost Ratio</u>
0.2	8.09	5.08	10.29	1.73
0.3	10.58	5.30	16.18	2.06
0.4	10.76	5.00	15.01	1.74
0.5	10.49	5.17	14.05	1.67
0.7	10.83	5.11	12.85	1.35
0.9	10.86	5.19	11.29	1.08

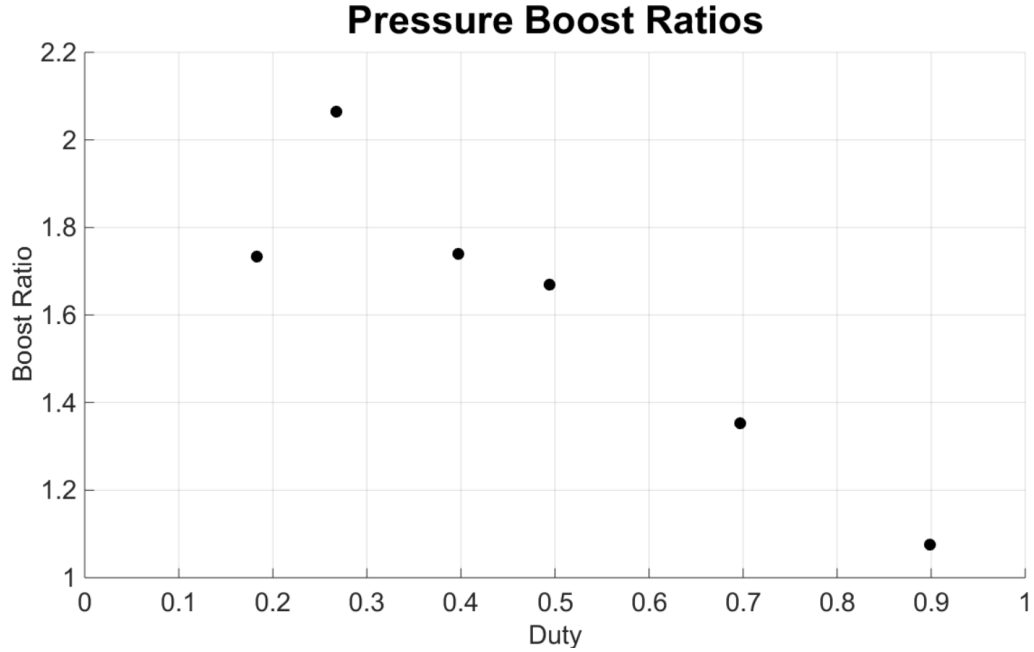


Figure 4.11. Boost ratio as a function of duty

The general trend is a decrease in duty cycle leads to an increase in boost ratio up to a maximum boost ratio of over 2 at a duty cycle of 0.3. Below a duty cycle of 0.3 the boost ratio begins to decrease. At low duty cycles, the overall source flow rate increases to a level where the frictional system losses decrease the boost potential. As shown in Table 4.5, the HPU was not able to meet desired rail pressure due to the high flow rate into the inertance tube at the lowest duty cycle.

The steady state power calculations for the load and rail are based on the flow rates and differential pressures as shown in Eq. (4.7), (4.8). The experimental load and rail power at each duty cycle are presented in Figure 4.12. The steep drop in load power at a duty cycle of 0.2, represents a decrease in efficiency caused by excessive friction losses as well as the system demand exceeding the flow rate capability of the HPU.

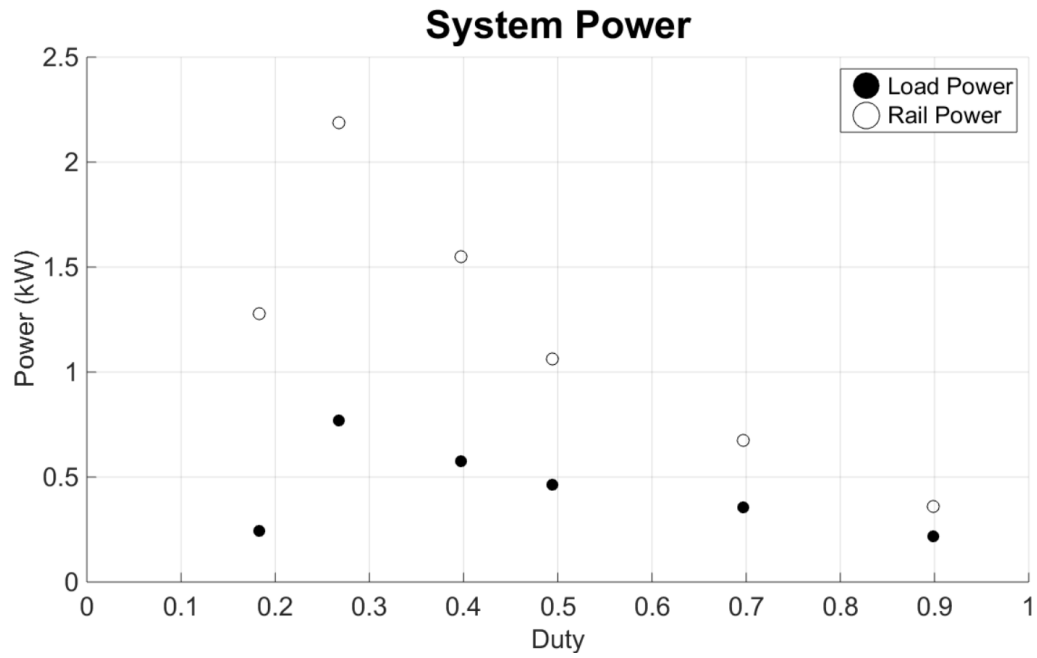


Figure 4.12. System power as a function of duty

The system efficiency is determined based on the ratio of load power and rail power as shown in Eq. (4.9). The experimental efficiency as a function of duty cycle are presented in Figure 4.11. A summary of the system powers and efficiencies are presented in Table 4.6.

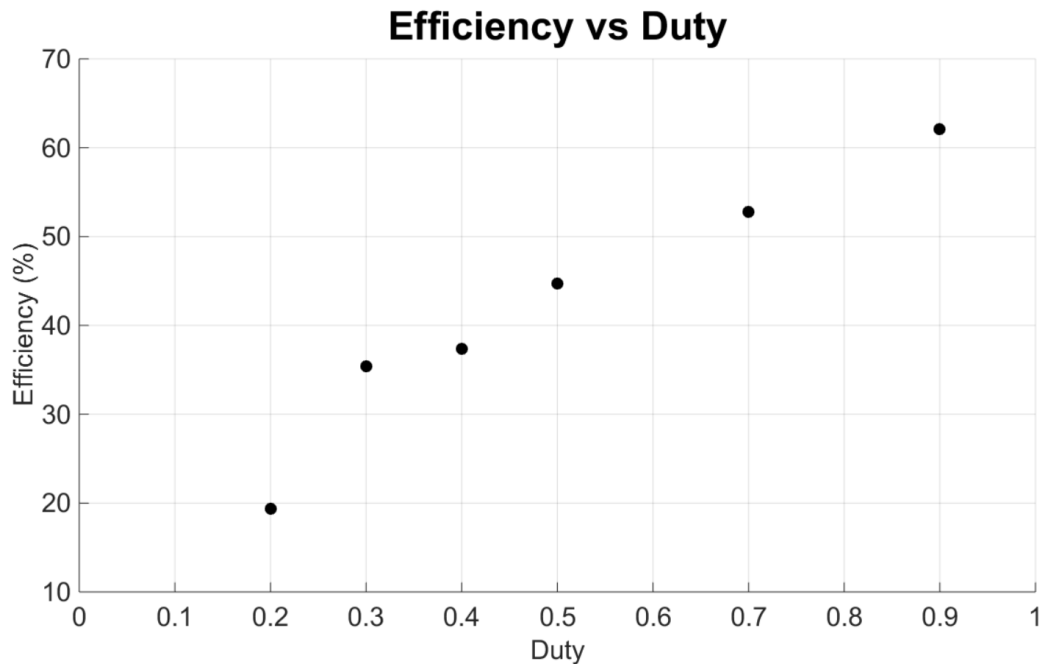


Figure 4.13. System efficiency as a function of duty

Table 4.6. Experimental power results

<u>Duty</u>	<u>Rail Power (kW)</u>	<u>Load Power (kW)</u>	<u>Efficiency</u>
0.2	1.28	0.24	19.4
0.3	2.19	0.77	35.4
0.4	1.55	0.58	37.4
0.5	1.06	0.46	44.7
0.7	0.67	0.35	52.7
0.9	0.36	0.22	62.1

The general trend is an increase in efficiency with an increase in duty cycle. At higher duty cycles, the valve is open to load for a higher percentage of time and thus the flow rate through the inertance tube decreases, which reduces the system friction losses.

The sonic velocity in the fluid, based on the bulk modulus of 1.40 GPa and density of 874 kg/m³, was calculated from Eq. (4.2) as 1266 m/s. The determination of the bulk modulus was discussed in the previous section and was completed at a temperature of 24 °C after a 24 hour period of resting in a vented tank. The effects of temperature and entrained air content in the actual experimental set up could have had large effects on these fluid properties and ideally real time inline determination would have been completed. An alternative method for determining the sonic velocity is the wave propagation, as measured by the time of flight between the mid-tube and switched volume at the valve entry. Figure 4.14 presents these transient pressures at a duty of 0.5 along with the labeling of three wave propagation occurrences. The time between propagation events and the distance between pressure sensors (1.74 m) resulted in a calculated sonic velocity of 1403 m/s for all three events. The sonic velocity based on wave propagation is 10.8% greater than that based on density and bulk modulus. This discrepancy can be attributed to variations in the entrained air content and fluid temperature, which are different from those used in the bulk modulus determination. In future tests, the sonic velocity measurement via the time of flight of a pressure wave should be taken into account as it results in a 10.8% greater optimal switching frequency and includes additional system effects such as tube compliance.

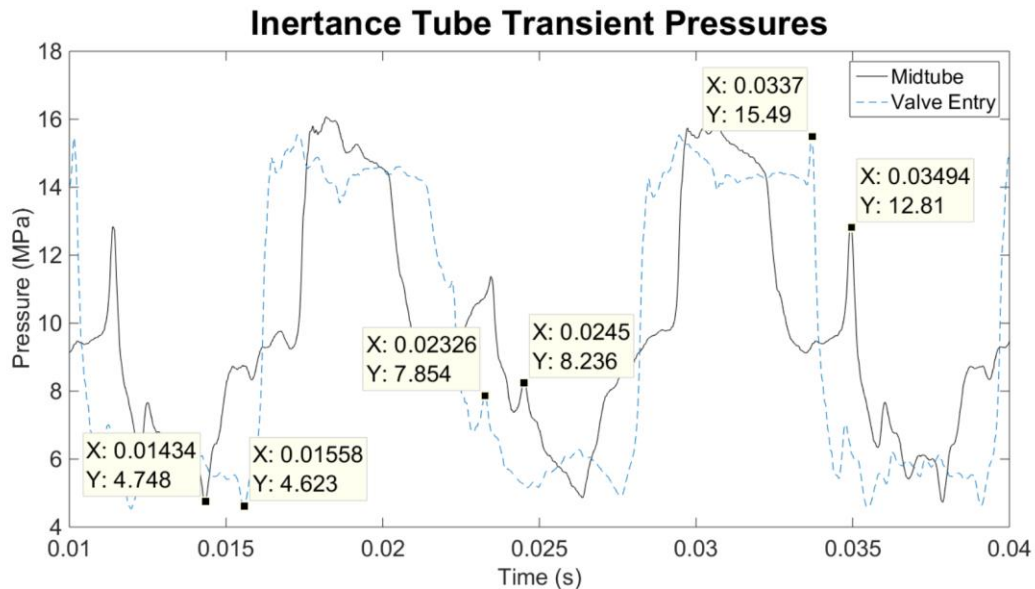


Figure 4.14. Inertance tube pressure transients at D=0.5

The results from the experimental switch-mode tests including boost ratio, load power, rail power, efficiency, and sonic velocity were presented in this section. The subsequent section will provide a brief discussion and overview of this chapter.

4.3. Discussion and Conclusion

In this chapter, an experimental test setup, operating procedures, and experimental results were presented for a pressure boost converter circuit. The experimental system used the high-speed switching valve presented in chapter 3, a source pressure set point of 11 MPa, and a tank pressure of 5 MPa. Tests were completed at six duty cycle set points consisting of 0.2, 0.3, 0.4, 0.5, 0.7, and 0.9 with respective switching frequencies of 33.2, 49.8, 66.4, 83.0, 49.8, and 16.6 Hz.

The resultant circuit was able to accomplish a pressure boost ranging from 1.08 at a duty cycle of 0.9 to a maximum boost of 2.06 at a duty cycle of 0.3. The general trend was a decrease in duty cycle led to an increase in boost ratio down to a duty cycle of around 0.3. At duty cycles below this, the flow through the inertance tube increases significantly, causing the friction losses to decrease the boost ratio. The conversion of fluid inertance into an elevated load side pressure demonstrated the successful use of the high-speed valve in a switched mode system.

Due to the non-linear nature of the orifice load, at lower duty cycles, where higher load pressures were achieved, higher power was delivered to the load. A maximum load power of 0.77 kW was achieved at a duty cycle of 0.3. The system also reached a maximum source power of 2.8 kW at a duty cycle of 0.3. The peak source power of 2.8 kW is significantly lower than the valve designed power of 13 kW resulting in non-optimized valve operation. Increasing the system power delivery through a source pressure increase, inertance tube length reduction or diameter increase, or a simulated load resistance reduction could improve the valve efficiency in the system.

The system efficiency ranged from 19% at $D=0.2$ to 62% at $D=0.9$. The overall trend resulted in an increased efficiency at a higher duty cycle. Lower duty cycles result in higher source flow rates. These high flow rates contribute to larger friction losses in the inertance tube, lowering the

system efficiency. These initial efficiencies are promising for the first sets of tests of this system, but need improvement for commercial viability. Many tuning parameters exist, such as switching frequency, load orifice, rail/tank pressure, valve overlap, and inertance tube dimensions, which could potentially offer efficiency improvements. The dynamic switch-mode system model being constructed by lab colleague Alexander Yudell should allow tradeoff mapping of these parameters to maximize efficiency. In addition soft switching could also provide efficiency gains by reducing throttling losses during transition.

The wave propagation in the tube provided an alternative method of calculating the fluid sonic velocity. Based on the density and bulk modulus, the sonic velocity was calculated as 1266 m/s, and was used to determine the optimal switching frequency. The sonic velocity based on the time of flight between wave propagation was 10.8% greater at 1403 m/s. Further studies should investigate if selecting the switching frequency based on time of flight sonic velocity provides a more efficient system.

In summary, the high-speed hydraulic valve is an integral part of the demonstrated switch-mode circuit, which demonstrated a boost ratio over two. The results showed a high repeatability of the pressure waveforms generated from abrupt valve switching. Future system testing, including adjusting the load orifice area, system pressures, and switching frequencies should be completed to work towards improved system efficiencies. It is also worthwhile to investigate operation with a non-boosted tank pressure. In addition, the use of soft switching and high-speed check valves could additionally improve system efficiencies. Longer term goals should include the use of this valve in a pressure buck converter circuit and improving system design into a realistic industry package. Overall, the experimental test provided proof of hydraulic boost capabilities validating the valve operation.

5. Conclusion

5.1. Review

The content of this thesis consisted of an overview of the field of digital hydraulics and the motivation to pursue more efficient hydraulic systems, presented in chapter 1. This also included an overview of current high-speed hydraulic valve and switch-mode circuit research. Chapter 2 presented a model and design of a dual spool crank-slider valve capable of the demanding requirements needed for efficient switch-mode hydraulic circuit operation. Chapter 3 presented experimental data of the resulting valve prototype which demonstrated agreement between the experimental and analytical model results. Chapter 4 demonstrated the successful use of this high-speed valve in a pressure boost converter hydraulic circuit. The remaining sections of this chapter present an overview of the critical contributions in section 5.2 and recommendations for future work in section 5.3.

5.2. Conclusions

The contributions of this thesis work consisted of the modeling and design of a high-speed dual crank-slider valve, the experimental comparison of the resulting prototype with the analytical model, and the demonstration of this high-speed valve in a pressure boost converter.

The first contribution was the design and modeling of a high-speed hydraulic valve. The valve architecture consisted of two spools driven by a 4-bar crank-slider mechanism. The spools were arranged to create the flow paths of a 3/3 valve supplying a 5/3 valve. The spools were driven via a common crank-shaft enabling a variable duty cycle by phase shifting one of the crank arms relative to the other. A model was developed to evaluate the tradeoffs in dimensioning the valve. The valve rated flow and pressure were 22.8 lpm and 34.5 MPa. The transition time was defined as the time to travel from a fully closed state to an open state and was selected as 5% of the total cycle time at a switching frequency of 120 Hz. The valve was defined as open when the effective area of the sleeve orifices was sufficient to reduce the pressure drop to less than 1% of rated pressure at rated flow. Using these constraints a dimensional optimization that determined crank radius, spool diameter, sleeve orifice diameter, and number of sleeve orifices was completed to minimize leakage and viscous friction energy loss. The resultant leakage and viscous friction loss

was 1.7% of rated power. Modifying the valve block dimensions to decrease dead volume resulted in a dead volume of 9.93 cc at a secondary pressure loss of 0.74% of rated pressure.

The second contribution was the fabrication of a valve prototype and experimental comparison with the model. The first experimental test consisted of a low speed rotation to obtain a valve profile based on crank-shaft position. Based on the orifice equation a lumped C_dA was determined by measuring the pressure in/out and the flow rate through the valve. This was completed at nine different flow rates, from 1.17-17.49 lpm, to obtain a flow dependent fully open C_dA relationship. This had good agreement in shape with analytical values. From these data, the transition time to fully open was compared with analytical with an agreement within 3%. The experimentally measured valve overlap was 13.3% less than predicted by the analytical model. This difference was 0.13% of the total cycle length. The experimental data also revealed a cycle asymmetry between the two cycles caused by mis-alignment of the valve setup to prevent binding of the linkage. The second experiment compared the experimental and analytical leakage rates. Leakage peaks occurred as predicted during transition. The overall magnitude of the peaks were in the expected range, but there was discrepancy in the experimental and analytical values. This was attributed to the behavior of the gear flow meters and manufacturing tolerances of the spools. The third test consisted of a transient torque test to compare analytical drive torque, which is dependent on viscous friction, to experimental. At low speeds, binding at the toggle positions caused higher experimental values. At higher speeds the analytical and experimental results were in better agreement. Overall the fabricated valve profile matched the analytical well especially in the critical areas of transition and shape.

The third contribution was the successful experimental demonstration of the high-speed valve in a pressure boost converter. The experimental setup consisted of an inertance tube upstream of the switching valve and a throttling valve to simulate a flow load. Six experimental tests were completed at duty cycles from 0.2-0.9 at a peak switching frequency of 83 Hz at a duty cycle of 0.5. Prior to each test, a slow speed valve profile was acquired to compare the actual duty cycle to the target set point. With a target source pressure of 11 MPa and a boosted tank pressure of 5 MPa a boost ratio up to 2.06 was accomplished at a duty cycle of 0.3. The efficiency of the circuit ranged from 19% to 62% with a general trend of higher efficiency at high duty cycles. A

comparison of time of flight sonic velocity and fluid properties yielded a 10.8% greater velocity based on time of flight. The valve in the pressure boost converter overall demonstrated great boost potential, but further efficiency work is required.

This section presented the contributions of the work completed. Section 5.3 provides an overview of future work to allow further improvements.

5.3. Recommendations for Future Work

The major recommendations can be broken into two sections, further work with switch-mode testing utilizing the valve prototype and further improvements for valve design.

The pressure boost converter experimental tests were completed with a boosted tank pressure to prevent cavitation. Non-boosted experimental tests should be completed and effects of cavitation on the system should be determined. The data acquired during these tests should be validated against a comprehensive dynamic system model. With a validated hydraulic model, efficiency mapping would allow the optimization of the operating parameters such as switching frequency, inertance tube dimensions, and pressure set points. With an optimized circuit, the load effects should be investigated through studies with a linear actuator and hydraulic motor. Additionally, system improvements such as soft switching and use of high-speed check valves should be investigated. If the switch-mode setups show feasible high efficiency results, further work with valve optimization should be completed.

The optimization of a drive mechanism was not in the scope of this work. A potential phase shift mechanism was presented in Appendix A.2, but its use was not implemented. This requires additional design to implement operational phase shifting. A drive system operating from fluid scavenged power would also greatly improve the design. Very few considerations were given to the overall size of the setup and vast improvements would be needed to make it commercially viable. Further requirements for automated valve and system performance would require a control algorithm to properly adjust valve duty cycle and frequency based on load demand.

The power density in fluid systems inherently provides an advantage over equivalent electromechanical systems. Fluid power systems, however, have not made major leaps in efficiency improvement and still typically rely on decades old technologies. The work in this thesis provides an insight into switch-mode hydraulics, offering the possibility of improved adjustable power delivery through the use of switched inertance hydraulic systems. Demonstration of a boost ratio greater than two without a conventional pump/motor based hydraulic transformers is an exciting demonstration of this technology. Further work in high-speed valve design and efficient switch-mode system demonstration is required for continued research in this field.

6. References

- [1] L. J. Love, E. Lanke and P. Alles, "Estimating the Impact (Energy, Emissions and Economics) of the U.S. Fluid Power Industry," Oak Ridge National Laboratory, Oak Ridge, 2012.
- [2] M. Linjama, "Digital Fluid Power - State of the Art," in *The Twelfth Scandinavian International Conference on Fluid Power*, Tampere, 2011.
- [3] N. Mohan, T. M. Undeland and W. P. Robbins, *Power Electronics: Converters, Applications, and Design*, New York: Wiley and Sons, 1995.
- [4] H. Kogler and R. Scheidl, "Two Basic Concepts of Hydraulic Switching Converters," in *The First Workshop on Digital Fluid Power*, Tampere, 2008.
- [5] M. Pan, J. Robertson, N. Johnston, A. Plummer and A. Hillis, "Experimental Investigation of a Switched Inertance Hydraulic System," in *ASME/BATH 2014 Symposium on Fluid Power and Motion Control*, Bath, 2014.
- [6] H. Yang and M. Pan, "Engineering Research in Fluid Power: A Review," *Journal of Zhejiang University-Science A*, vol. 16, no. 6, pp. 427-442, 2015.
- [7] J. Lumkes Jr., M. A. Batdorff and J. R. Mahrenholz, "Model Development and Experimental Analysis of a Virtual Displacement Pump System," *International Journal of Fluid Power*, vol. 10, no. 3, pp. 17-27, 2009.
- [8] J. M. Pan, K. S. Plummer and A. Hillis, "Theoretical and experimental studies of a switched inertance hydraulic system," *Journal of Systems and Control*, pp. 12-25, 2014.
- [9] R. E. Clark, G. W. Jewell, J. S. Forrest, J. Rens and C. Maerky, "Design Features for Enhancing the Performance of Electromagnetic Valve Actuation Systems," *IEEE Transactions on Magnetics*, vol. 41, no. 3, pp. 1163-1168, 2005.

- [10] T. Kajima, S. Satoh and R. Sagawa, "Development of a high speed solenoid valve," in *Transactions of the Japan Society of Mechanical Engineering: Part C*, 1994.
- [11] S. Yang and J. C. Ordonez, "Concurrent Solenoid Design Optimization From Thermal and Electromagnetic Standpoint," *IEEE Transactions on Applied Superconductivity*, vol. 26, no. 4, 2016.
- [12] T. Muto, H. Yamada and Y. Suematsu, "PWM Digital Control of a Hydraulic Acuator Utilizing Two-Way Solenoid Valves," *Journal of Fluid Control*, pp. 24-41, 1990.
- [13] T. Kajima and Y. Kawamura, "Development of a High-Speed Solenoid Valve: Investigation of Solenoids," *IEEE Transactions on Industrial Electronics*, vol. 42, no. 1, 1995.
- [14] C. Noergaard, D. B. Roemer, M. M. Bech and T. O. Andersen, "Experimental Validation of Mathematical Framework for Fast Switching Valves Used in Digital Hydraulic Machines," in *ASME/BATH 2015 Symposium on Fluid Power and Motion Control*, Chicago, 2015.
- [15] T. Royston and R. Singh, "Development of a Pulse-Width Modulated Pneumatic Rotary Valve for Actuator Position Control," *Journal of Dynamic Systems, Measurement, and Control*, pp. 495-505, 1993.
- [16] J. D. Van de Ven and A. Katz, "Phase-Shift High-Speed Valve for Switch-Mode Control," *Journal of Dynamic Systems, Measurement, and Control*, 2011.
- [17] H. C. Tu, M. Rannow, J. Van de Ven, M. Wang, P. Li and T. Chase, "High Speed Rotary Pulse Width Modulated On/Off Valve," in *ASME International Mechanical Engineering Congress*, Seattle, WA, 2007.
- [18] S. Yokota and K. Akutu, "A Fast-Acting Electro-Hydraulic Digital Transducer," *JSME International Journal*, pp. 489-495, 1991.
- [19] T. Lantela, J. Kajaste, J. Kostamo and M. Pietola, "Pilot Operated Miniature Valve with Fast Response and High Flow Capacity," *International Journal of Fluid Power*, vol. 15, no. 1, pp. 11-18, 2014.

- [20] N. P. Sell, N. Johnston, A. R. Plummer and S. Kudzma, "Development of a Position Controlled Digital Hydraulic Valve," in *ASME/Bath 2015 Symposium on Fluid Power and Motion Control*, Chicago, 2015.
- [21] M. Pan, N. Johnston, A. Plummer, S. Kudzma and A. Hillis, "Theoretical and Experimental Studies of Switched Inertance Hydraulic System," *Systems and Control Engineering*, pp. 12-25, 2014.
- [22] V. J. De Negri, P. Wang, A. Plummer and N. Johnston, "Behavioural Prediction of Hydraulic Step-Up Switching Converters," *International Journal of Fluid Power*, vol. 15, no. 1, pp. 1-9, 2014.
- [23] F. Wang, L. Gu and Y. Chen, "A Hydraulic Pressure-Boost System Based on High-Speed On-Off Valves," *IEEE/ASME Transactions on Mechatronics*, vol. 18, no. 2, pp. 733-743, 2013.
- [24] B. Beckstrand and J. D. Van de Ven, "Experimental Validation of a Soft Switch for a Virtually Variable Displacement Pump," in *ASME/BATH Symposium on Fluid Power & Motion Control*, 2014.
- [25] M. B. Rannow and P. Y. Li, "Soft Switching Approach to Reducing Transition Losses in On/Off Hydraulic Valve," *Dynamic Systems, Measurements, and Control*, 2012.
- [26] A. Katz and J. D. Van de Ven, "Design of a High-Speed On-Off Valve," in *International Mechanical Engineering Congress and Exposition*, Lake Buena Vista, FL, 2009.
- [27] J. Wu and J. D. Van de Ven, "Development of a High-Speed On-Off Valve for Switch-Mode Control of Hydraulic Circuits with Four-Quadrant Control," in *ASME International Mechanical Engineering Congress & Exposition*, Vancouver, British Columbia, 2010.
- [28] K. L. Johnson, in *Contact Mechanics*, Cambridge, Cambridge University Press, 1985, pp. 84-106.
- [29] H. Tian. Personal Communication. 19 February 2016.

- [30] M. B. Rannow, H. C. Tu, P. Y. Li and T. R. Chase, "Software Enabled Variable Displacement Pumps-Experimental Studies," in *ASME International Mechanical Engineering Congress and Exposition*.
- [31] P. Cui, R. T. Burton and R. R. Ukrainetz, "Development of a High Speed On/Off Valve," *SAE Technical Paper Series*, pp. 21-25.

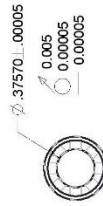
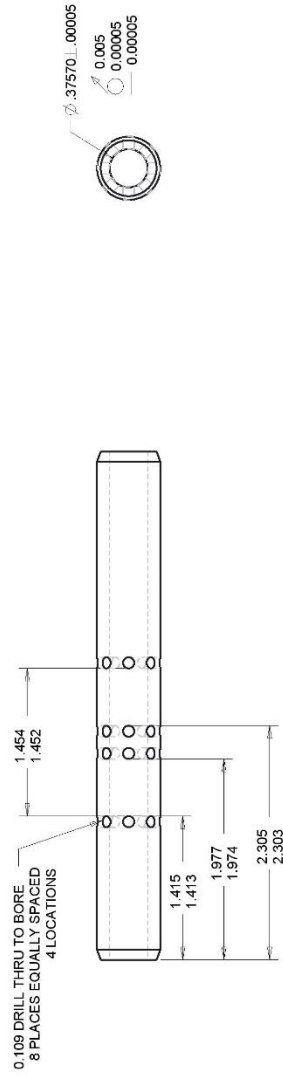
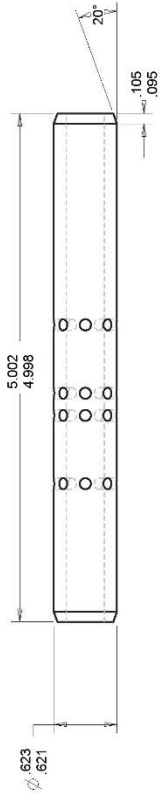
Appendix A.

Appendix A.1. Valve Part Drawings

The valve part drawings are contained in this appendix. They are in the following order:

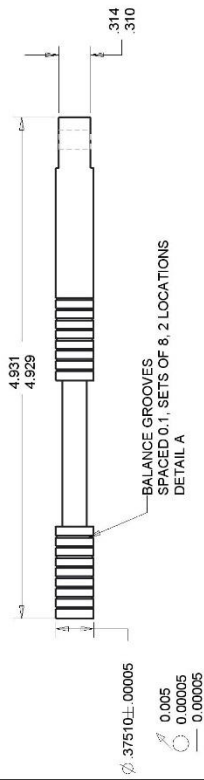
1. 3-Way Sleeve
2. 3-Way Spool
3. 3-Way Valve Block
4. 5-Way Sleeve
5. 5-Way Spool
6. 5-Way Valve Block
7. Connecting Rod 1
8. Connecting Rod Drive Collar
9. Connecting Rod 2
10. Connecting Rod 1 Drive Shaft
11. Connecting Rod 2 Drive Shaft
12. Main Drive Shaft
13. Flywheel
14. Bearing Block
15. Valve Block Spacer
16. Hold Washer
17. Back Stop
18. Vertical Plate
19. Vertical Mount Bottom Plate
20. Outlet Manifold

NOTES:
 1. ALL OUTSIDE DIAS $\sqrt{0.002}$
 2. SLEEVE TO BE AIR QUENCHED TO MINIMIZE DISTORTION
 3. O.D. $\sqrt{0.0025}$ AFTER HEAT TREAT



UNIVERSITY OF MINNESOTA			
TITLE	SUBASSEMBLY	3-WAY VALVE	
DRAWN	REV# & DATE	MATERIAL	HEAT TREAT
SEK	02, 5/27/15	C11L17	S-50

- NOTES:
 1. ALL OUTSIDE DIA'S ± 0.002
 2. SPOOL TO BE AIR QUENCHED TO MINIMIZE DISTORTION
 3. O.D. ± 0.0025 AFTER HEAT TREAT



DETAIL A

Features
 S-57, Balance Grooves

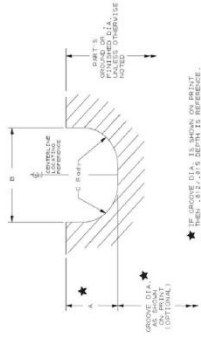
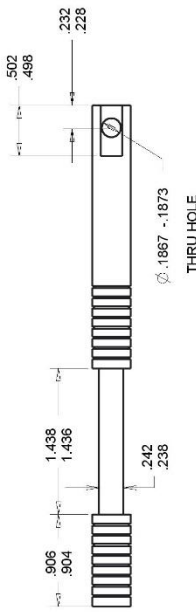
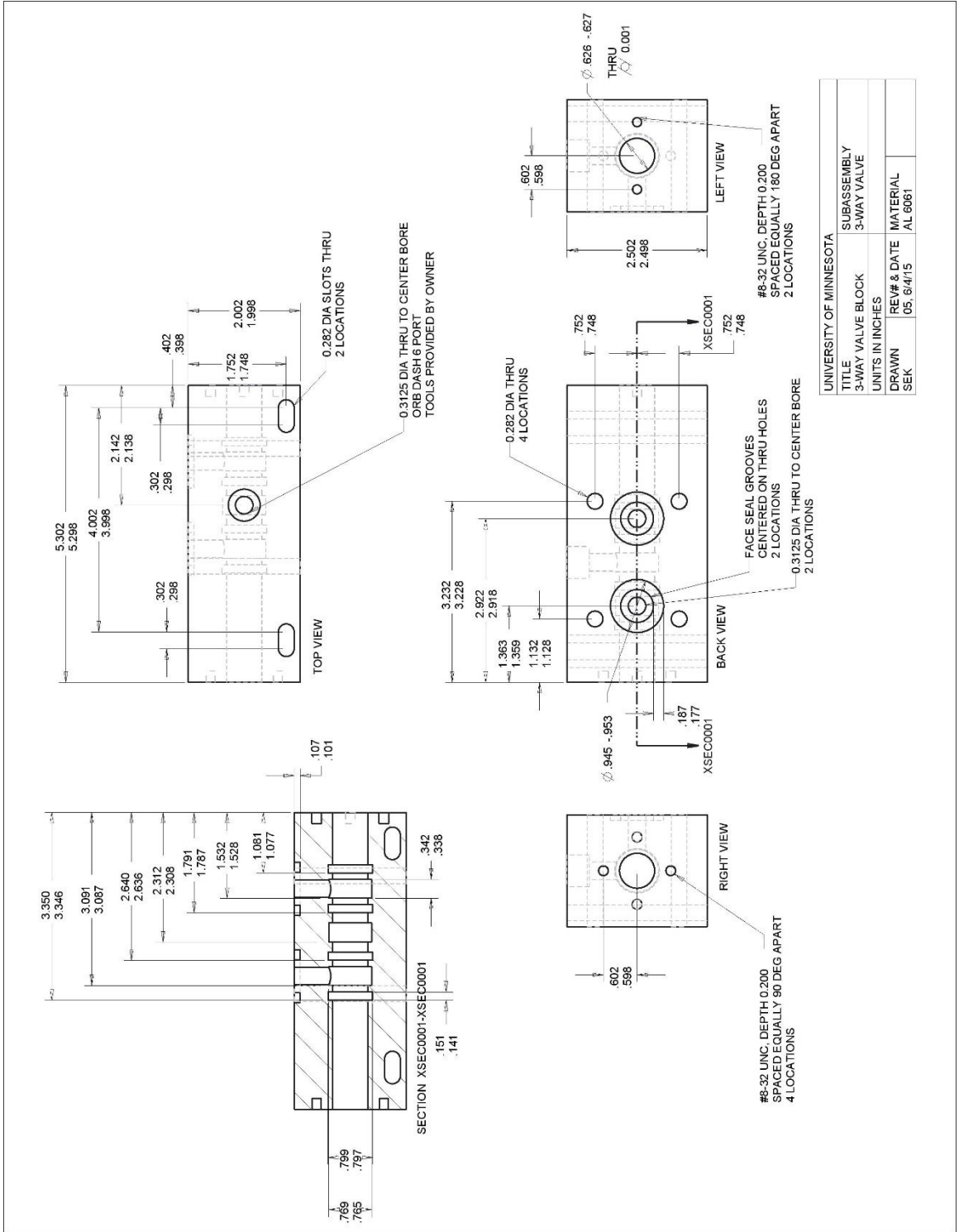


Figure 1

Legend:
 A- $0.12/0.15$ in
 B- $0.02/0.05$ in
 C- $0.008/0.010$ in

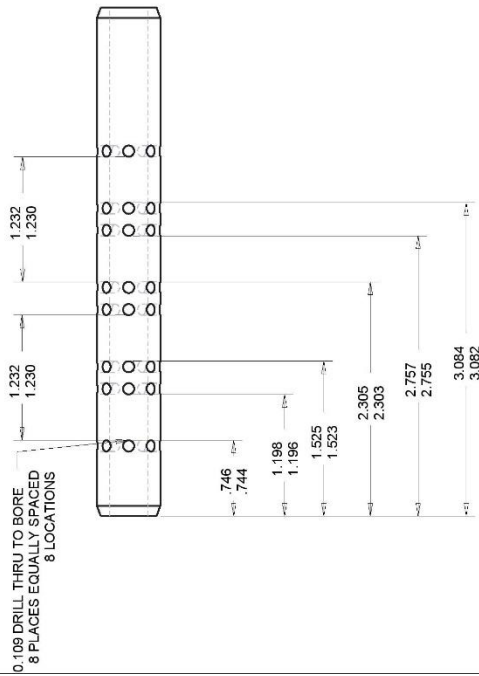
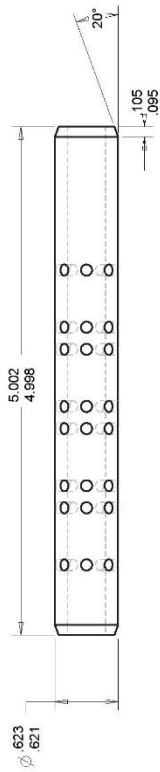


UNIVERSITY OF MINNESOTA	
TITLE	SUBASSEMBLY
3-WAY SPOOL	3-WAY VALVE
DRAWN	REV# & DATE
SEK	02. 5/27/15
MATERIAL	HEAT TREAT
C11L17	S-50



UNIVERSITY OF MINNESOTA	
TITLE	SUBASSEMBLY
UNITS IN INCHES	3-WAY VALVE
DRAWN	REV# & DATE
SEK	05.6/4/15
	MATERIAL
	AL 6061

- NOTES:
 1. ALL OUTSIDE DIA'S \pm 0.002
 2. SLEEVE TO BE AIR QUENCHED TO MINIMIZE DISTORTION
 3. O.D. \pm 0.0025 AFTER HEAT TREAT



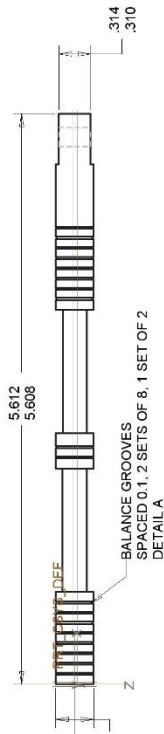
0.109 DRILL THRU TO BORE
 8 PLACES EQUALLY SPACED
 8 LOCATIONS



UNIVERSITY OF MINNESOTA	
TITLE	SUBASSEMBLY
DRAWN	S-WAY VALVE
REV# & DATE	MATERIAL
02.5/27/15	C11L17
HEAT TREAT	S-50

- NOTES:
 1. ALL OUTSIDE DIA'S ± 0.002
 2. SPOOL TO BE AIR QUENCHED TO MINIMIZE DISTORTION
 3. O.D. ± 0.0025 AFTER HEAT TREAT

$\phi .37510 \pm .00005$
 0.005
 0.00005
 0.00005



DETAIL A

Features
 S-67 Balance Grooves

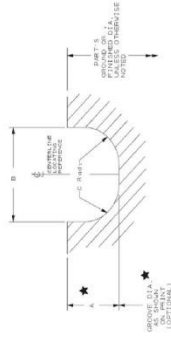
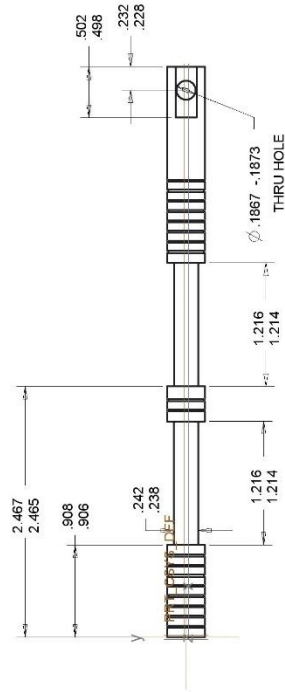
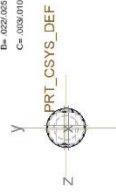
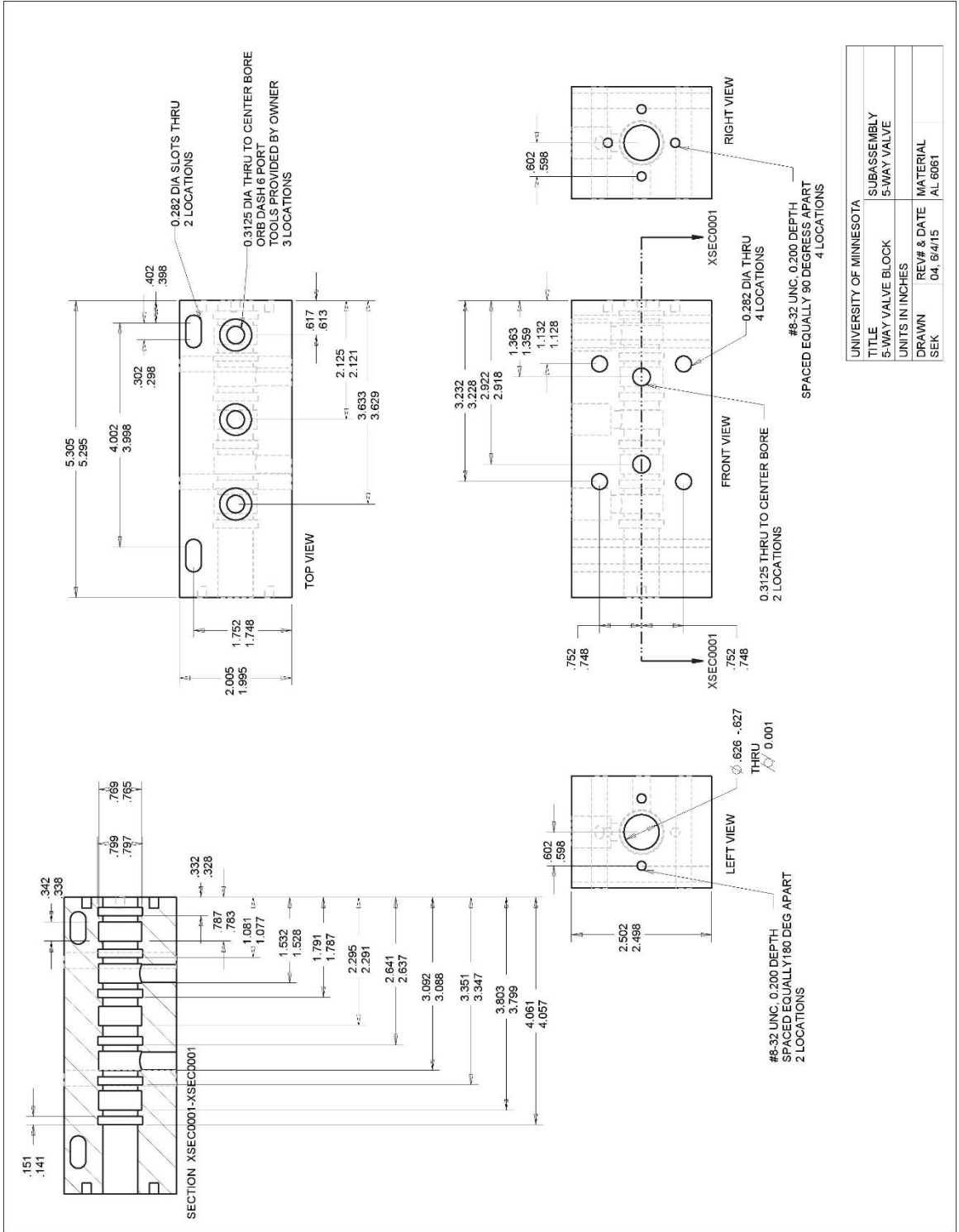


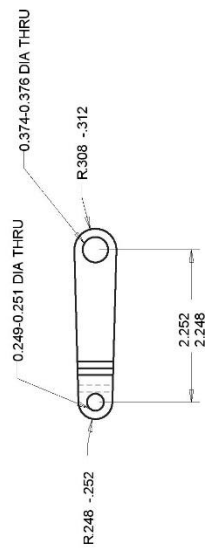
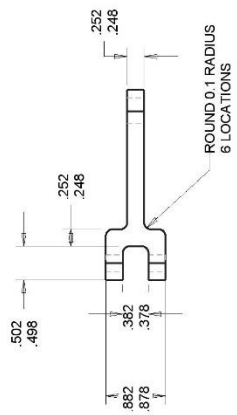
Figure 1
 Legend:
 A= .012/0.015 in
 B= .020/0.025 in
 C= .003/0.010 in



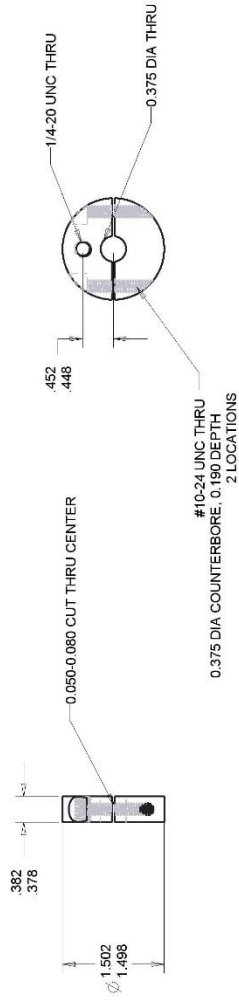
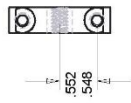
UNIVERSITY OF MINNESOTA	
TITLE	SUBASSEMBLY
5-WAY SPOOL	3-WAY VALVE
DRAWN	REV# & DATE
SEK	02.5/27/15
	MATERIAL
	C11L17
	HEAT TREAT
	S-50



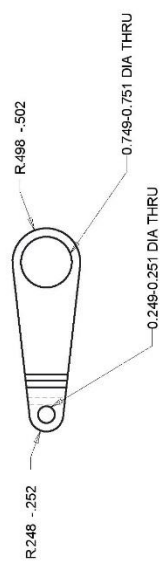
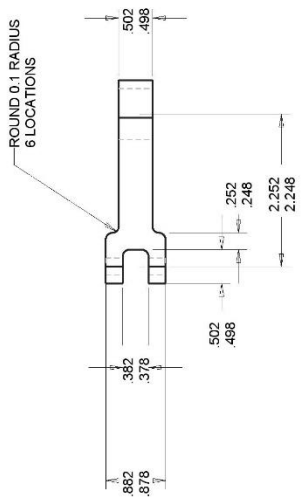
UNIVERSITY OF MINNESOTA	
TITLE	SUBASSEMBLY
UNITS IN INCHES	5-WAY VALVE
DRAWN	REV# & DATE
SEK	04, 8/4/15
	MATERIAL
	AL 6061



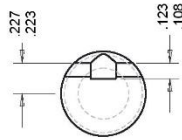
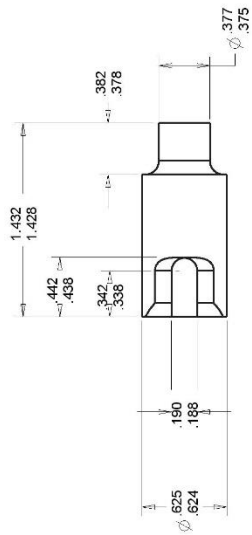
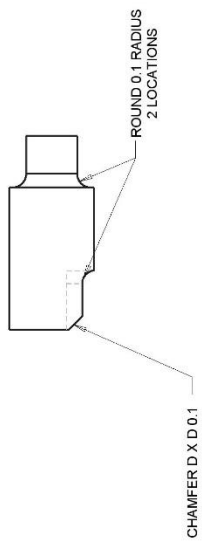
UNIVERSITY OF MINNESOTA	
TITLE	SUBASSEMBLY
3-WAY SPOOL CONROD	DRIVE MECHANISM
DRAWN	REV# & DATE
SEK	02, 6/2/15
	MATERIAL
	STEEL



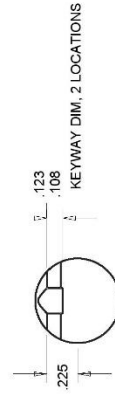
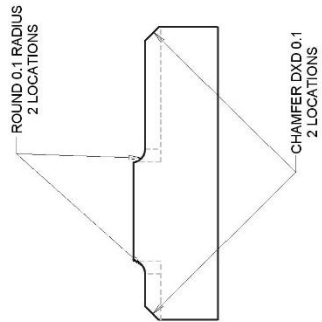
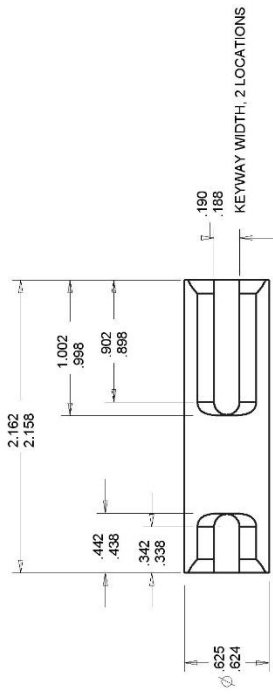
UNIVERSITY OF MINNESOTA	
TITLE	SUBASSEMBLY
CONROD1 DRIVE COLLAR	DRIVE MECHANISM
DRAWN	REV# & DATE
SEK	02. 02/15
	MATERIAL
	STEEL



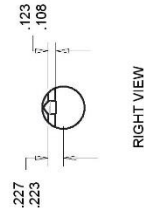
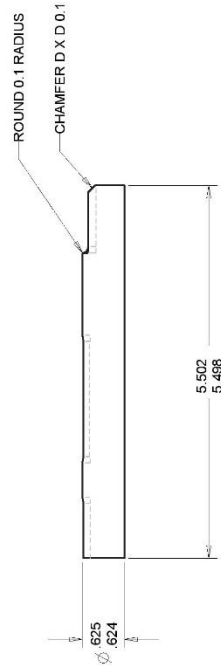
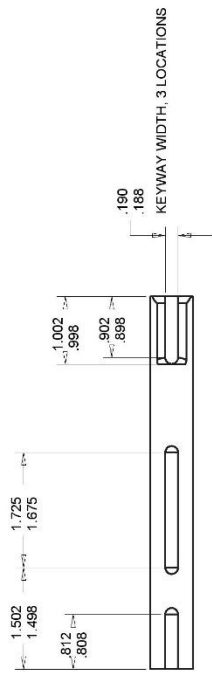
UNIVERSITY OF MINNESOTA			
TITLE	SUBASSEMBLY		
5-WAY SPOOL CONROD	DRIVE MECHANISM		
DRAWN	REV# & DATE	MATERIAL	
SEK	02.62/15	STEEL	



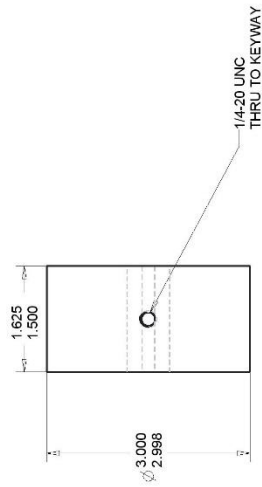
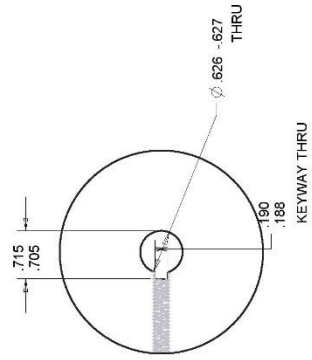
UNIVERSITY OF MINNESOTA	
TITLE	SUBASSEMBLY
CONROD1 DRIVE SHAFT	DRIVE MECHANISM
DRAWN	REV# & DATE
SEK	02.62/15
	MATERIAL
	STEEL 1045



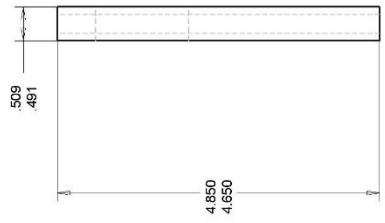
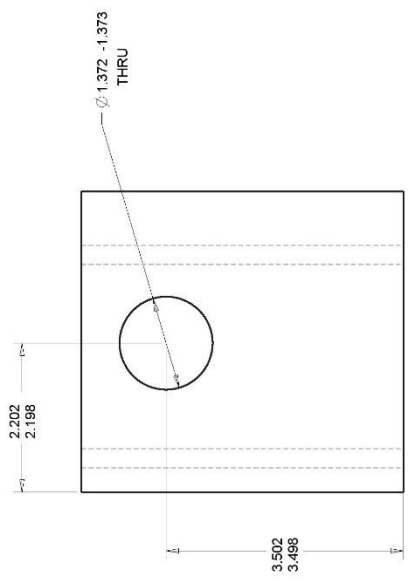
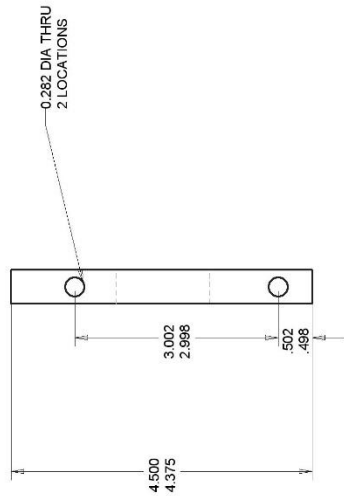
UNIVERSITY OF MINNESOTA			
TITLE	SUBASSEMBLY	DRIVE MECHANISM	
CONROD2 DRIVE SHAFT	REV# & DATE	MATERIAL	
DRAWN	02.62/15	STEEL 1045	
SEK			



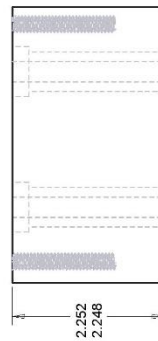
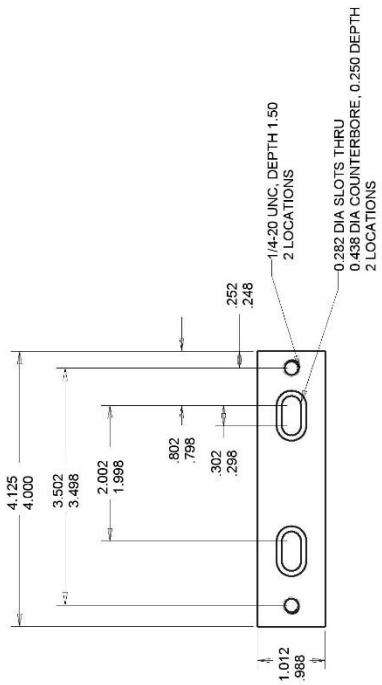
UNIVERSITY OF MINNESOTA			
TITLE	SUBASSEMBLY	MAIN DRIVE SHAFT	
DRAWN	REV# & DATE	DRIVE MECHANISM	MATERIAL
SEK	03. 03/15	STEEL 1045	



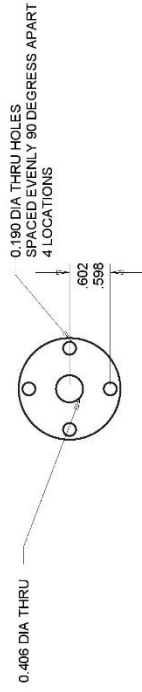
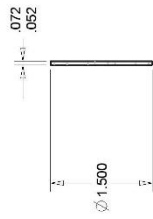
UNIVERSITY OF MINNESOTA	
TITLE	SUBASSEMBLY
FLYWHEEL	DRIVE MECHANISM
DRAWN	REV# & DATE
SEK	03, 6/3/15
	MATERIAL
	STEEL



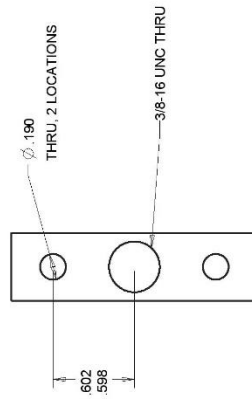
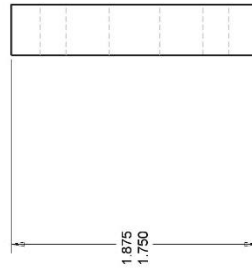
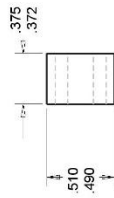
UNIVERSITY OF MINNESOTA			
TITLE	SUBASSEMBLY		
BEARING BLOCK	DRIVE MECHANISM		
DRAWN	REV# & DATE	MATERIAL	
SEK	03, 6/3/15	AL 6061	



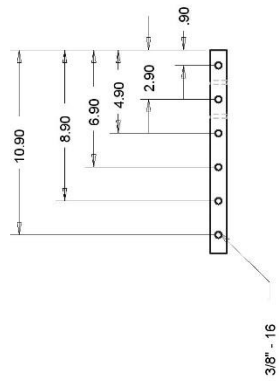
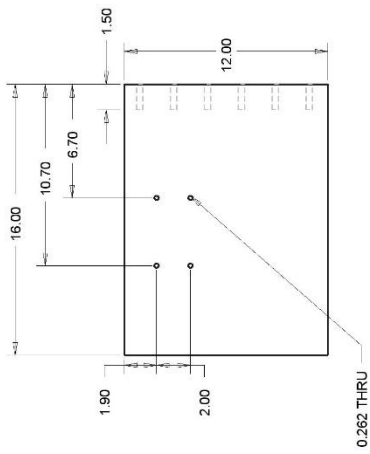
UNIVERSITY OF MINNESOTA			
TITLE	SUBASSEMBLY		
VALVE BLOCK SPACER	MISC		
DRAWN	REV# & DATE	MATERIAL	
SEK	03. 6/3/15	AL 6061	



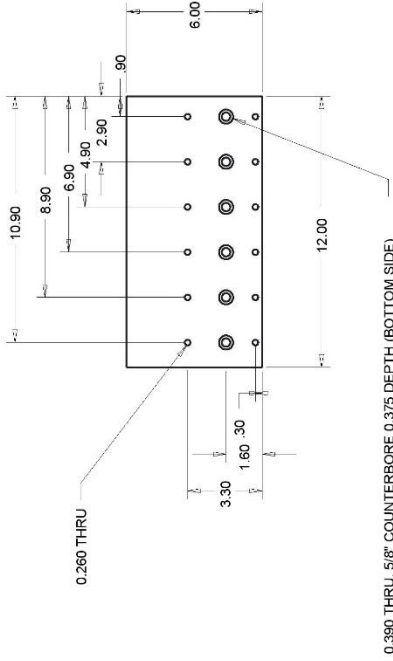
UNIVERSITY OF MINNESOTA	
TITLE	SUBASSEMBLY
HOLD WASHER	MISC
DRAWN	REV# & DATE
SEK	02.6/2/15 MATERIAL
	STEEL



UNIVERSITY OF MINNESOTA	
TITLE	SUBASSEMBLY
BACK STOP	MISC
DRAWN	REV# & DATE
SEK	03, 6/3/15
	MATERIAL
	STEEL

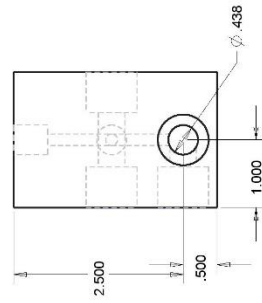
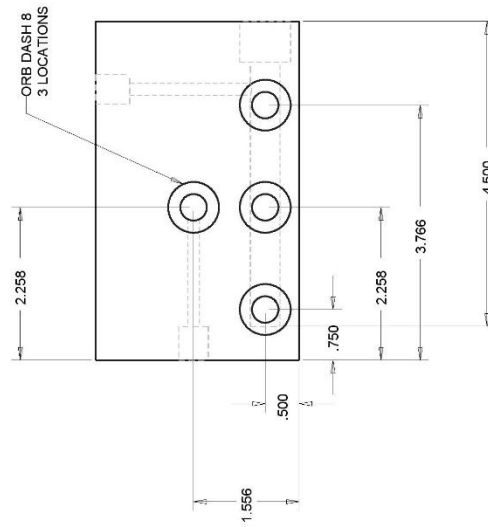
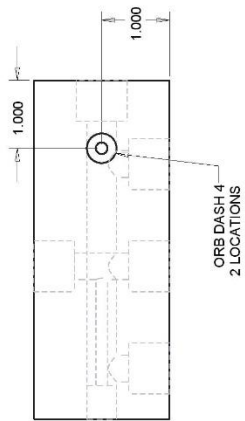


UNIVERSITY OF MINNESOTA	
TITLE	SUBASSEMBLY
VERTICAL MOUNT	MOUNT
UNITS IN INCHES	
DRAWN	REV# & DATE
SEK	01, 4/20/16
	MATERIAL
	AL 6061



0.390 THRU, 5/16" COUNTERBORE 0.375 DEPTH (BOTTOM SIDE)

UNIVERSITY OF MINNESOTA	
TITLE	SUBASSEMBLY
VERTICAL MOUNT BOTTOM	MOUNT
UNITS IN INCHES	
DRAWN	REV# & DATE
SEK	01, 4/20/16
	MATERIAL
	AL 6061



UNIVERSITY OF MINNESOTA	
TITLE	SUBASSEMBLY
OUTLET MANIFOLD	
UNITS IN INCHES	
DRAWN	REV.# & DATE
SEK	01.4/20/16
	MATERIAL
	AL 6061

Appendix A.2. Potential Active Phase Shift Mechanism

The valve presented achieved phase shift manually while in a static state. One concept for achieving phase shift in a dynamic state would be the use of a planetary gear set, such as that in a vehicle differential as shown in Figure 6.1.

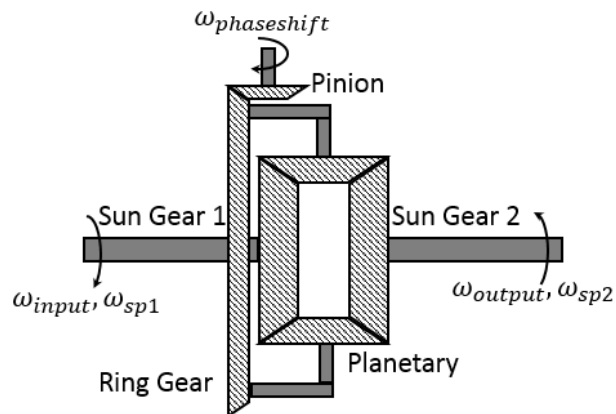


Figure 6.1. Dynamic phase shift concept utilizing differential gear set

A sun gear would be utilized as both the input and the driver of spool 1. Under normal, non-phase shifting operation, the ring gear would be held stationary resulting in an output of equal rotational velocity in the opposite direction. To achieve phase shift the pinion gear would be utilized to rotate the ring gear causing a variation in input and output velocities thus phase shifting the output and input shafts.

Appendix A.3. Pressure Sensor Calibrations

The following pressure transducer calibrations were completed for the pressure boost converter experimental setup. The testing was completed with the use of a hydraulic dead weight tester in the exact electrical configuration shown. The testing consisted of 7 points from 0-20.9MPa. The results from the 4-20mA transmitters were trended better by a third order polynomial than a linear fit.

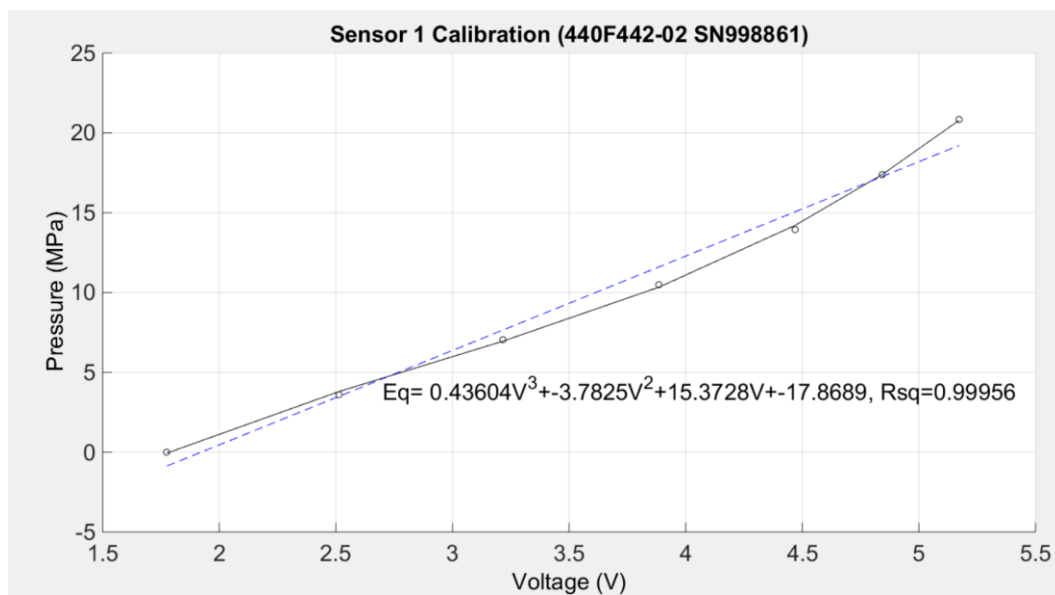


Figure 6.2. Pressure boost converter, source pressure transmitter calibration

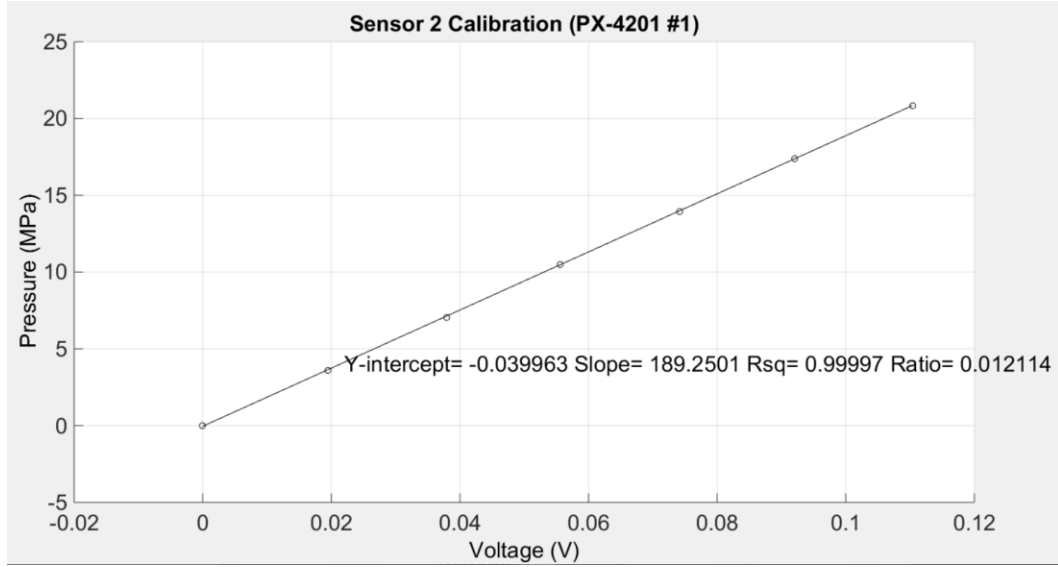


Figure 6.3. Pressure boost converter, mid-tube pressure transducer calibration

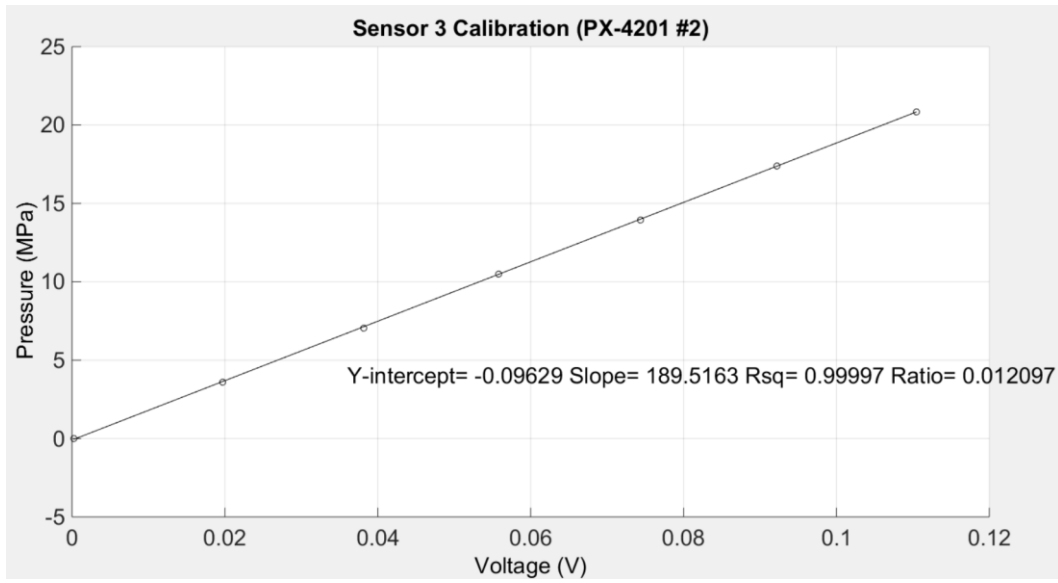


Figure 6.4. Pressure boost converter, valve entry pressure transducer calibration

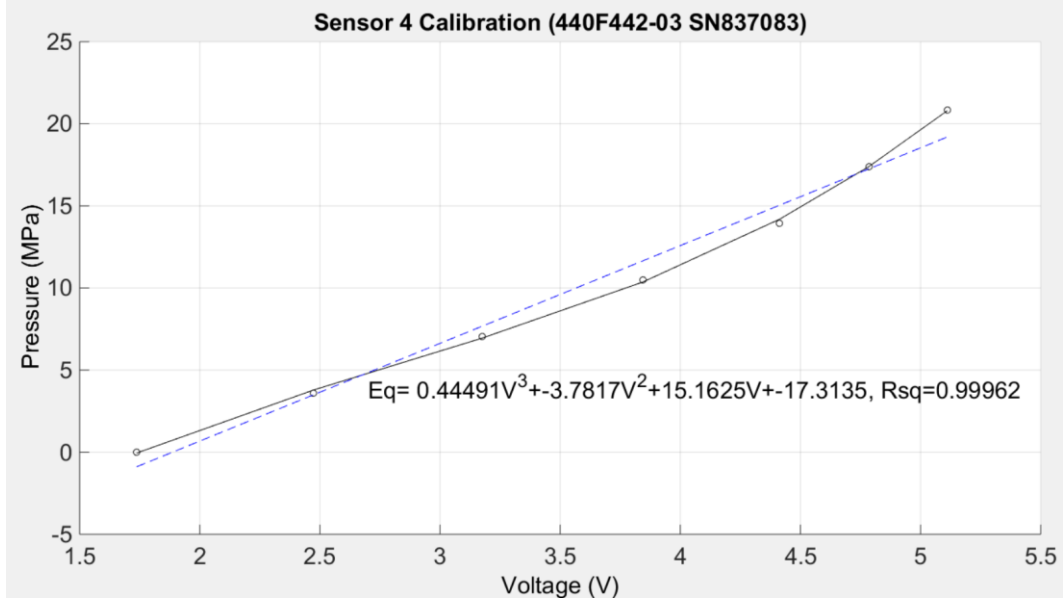


Figure 6.5. Pressure boost converter, load pressure transmitter calibration

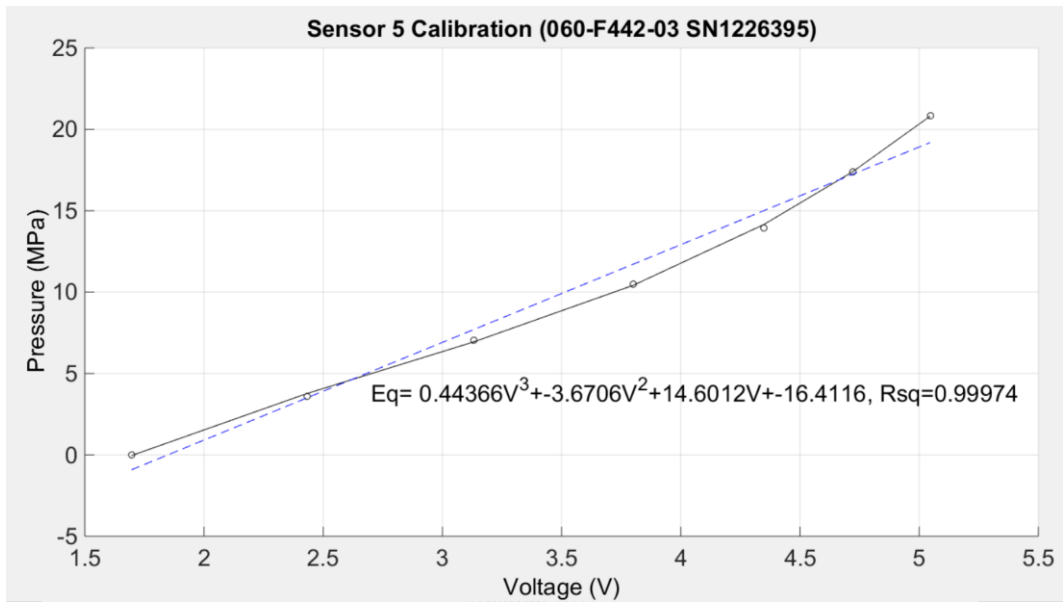


Figure 6.6. Pressure boost converter, tank pressure transmitter calibration